TÉCNICO LISBOA

Multi-Harmonic Identification with Swept-Sine Excitation in Nonlinear Dynamics

Carlos Eduardo Machado de Sousa

Thesis to obtain the Master of Science Degree in

Aerospace Engineering

Supervisor(s): Eng. Giancarlo Kosova
Prof. Nuno Miguel Rosa Pereira Silvestre

Examination Committee

Chairperson: Prof. Fernando José Parracho Lau
Supervisor: Prof. Nuno Miguel Rosa Pereira Silvestre
Member of the Committee: Prof. Nuno Manuel Mendes Maia

November 2022

Dedicado à minha família

Acknowledgments

First and foremost, I would like to thank Instituto Superior Técnico and Professor Nuno Silvestre for granting me the opportunity of taking this endeavour. I am also very grateful of Eng. Giancarlo Kosova, who closely guided me these last months. Without his expertise and dedication this work would not be possible.

I also have to thank Siemens Digital Industries Software for the internship opportunity. I could not have asked for a better environment to develop from and I can only wish for more colleagues of mine to experience the same I did.

This work also reflects the last 5 years of my life. All the friends and memories, Lisbon, Helsinki and Leuven will never be forgotten as they truly are the best of these years.

At last, I could not thank enough the endless support of my family.

Resumo

O Digital Tracking Filter (DTF) é uma técnica que obtém boas estimações de amplitude e fase de medições de resposta de um sistema e da força aplicada, e consequentemente das Funções de Resposta de Frequência (FRFs) da estrutura, sobre excitação swept-sine. É mais precisa que o harmonic estimator na presença de distúrbios tonais. O objectivo desta dissertação é estender o procedimento do DTF para estruturas não-lineares. De facto, enquanto que a resposta de uma estrutura linear apenas se manifesta à frequência fundamental de excitação ω, uma estrutura não-linear também vibra nos múltiplos de ω, $n \times \omega$, chamados harmónicos. A técnica proposta, nomeada Multi-Harmonic Digital Tracking Filter (MHDTF), estima a amplitude e fase dos harmónicos de ordem superior. O procedimento é aplicado a dados de simulação e experimentais e a influência de certos parâmetros do MHDTF é estudada. Os resultados também são comparados com outras técnicas do estado da arte.

As capacidades multi-harmónicas do MHDTF abrem a possibilidade do seu uso na área de identificação de sistemas não-lineares. Neste contexto, a metodologia de construção de um modelo multi-harmónico de State-Space é descrita e aplicada para simulações em tempo. O procedimento é aplicado a um modelo simulado de parâmetros discretos e a um setup experimental de uma aeronave demo. A vantagem desta abordagem é o seu uso simples e a possibilidade de obter uma melhor aproximação da resposta com as contribuições multi-harmónicas. A desvantagem encontra-se na linearização e, consequentemente, a precisão apenas se encontra ao nível de excitação usado na identificação.

Palavras-chave: Identificação de Sistemas Não-Lineares, Harmónicos de Ordem Superior, Curva de Resposta de Frequência Não-linear, Ensaios Dinâmicos, Filtro Digital, Modelo State-space Multi-harmónico.

Abstract

The Digital Tracking Filter (DTF) is a technique to obtain good estimations of the amplitude and phase of the measured system's response and applied force, and hence of the structural Frequency Response Functions FRFs, under swept-sine excitation. It is normally more accurate than the harmonic estimator in presence of tonal disturbances. The goal of this dissertation is to extend the DTF procedure to nonlinear structures. Indeed, while the response of a linear structure manifests only at the fundamental excitation frequency ω, a nonlinear structure vibrates also at integer multiples of ω, $n \times \omega$, called harmonics. The proposed technique, labelled Multi-Harmonic Digital Tracking Filter (MHDTF), estimates the amplitude and phase of these higher-orders harmonics as well. The procedure is first applied to simulated data and after experimental data and the influence of certain MHDTF parameters is studied. The results are also compared with the ones of other state of the art techniques.

The multi-harmonic capabilities of the MHDTF open the way to its potential use in the nonlinear system identification area. In this context, the methodology of obtaining a multi-harmonic State-Space model is described and used for time simulations. The procedure is applied to a simulated lumped parameter model and after a demo airplane experimental setup. The advantage of this approach is its simple use and the possibility to better approximate a response with multi-harmonic contributions. The clear drawback lies in the linearisation, hence, its accuracy only at the level of excitation used during the identification.

Keywords: Nonlinear System Identification, Higher-order harmonics, Nonlinear Frequency Response Curve, Dynamic Testing, Digital Filter, Multi-harmonic State-space Model.

Contents

List of Tables

List of Figures

Nomenclature

Greek symbols

Δt	Sampling interval.
λ	Eigenvalues.
ϕ	Phase.
ω	Frequency.
ω_n	Undamped natural frequency.
ω_d	Damped natural frequency.

Roman symbols

a	Linear sweep rate.
C	Damping matrix.
f	Frequency.
f_c	Cut-off frequency.
f_{nl}	Nonlinear restoring force.
f_s	Sampling frequency.
f_{ext}	External force.
G_{FF}	Input auto-power matrix.
G_{XF}	Output-input cross-power matrix.
H	Transfer function.
H_1	$H1$ estimator.
K	Stiffness matrix.

k_{nl} Nonlinear stiffness.

M Mass matrix.

N Number of sub-intervals.

n Degrees of freedom.

n_h Number of harmonics.

n_i Number of inputs.

n_o Number of outputs.

n_{sw} Number of sweeps.

S Logarithmic sweep rate.

t Time.

$\ddot{x}$ Acceleration.

$\dot{x}$ Velocity.

x Displacement.

Subscripts

h Harmonic order.

Superscripts

* Complex conjugate.

-1 Inverse.

T Transpose.

Acronyms

AFT Alternating Frequency/Time-domain. 20

BW bandwidth. 24, 31, 32, 39, 48, 58, 68, 78

COLA Constant Output Level Amplitude. 25, 26, 28, 29, 38, 40, 68

DOF Degree-of-Freedom. xvii, 7, 10, 12, 13, 15, 16, 53, 55, 57, 69, 73–75

DSP Digital Signal Processing. 22, 23

DTF Digital Tracking Filter. vii, ix, 1, 2, 4, 22, 25, 53, 77

EMA Experimental Modal Analysis. 7, 12

FEM Finite Element Method. 4

FEP Frequency-Energy Plot. xvii, 14–16

FRF Frequency Response Function. ix, 2, 3, 9, 10, 12–14, 63–67

GVT Ground Vibration Test. 1, 53

HB Harmonic Balance. 18, 20, 41, 51, 52, 77

LNM Linear Normal Mode. 14

MAC Modal Assurance Criterion. 64, 67

MDOF Multiple Degree-of-Freedom. 10

MHDTF Multi-Harmonic Digital Tracking Filter. vii, ix, xviii, xix, 25, 27–30, 33, 36–44, 46–57, 60, 62, 63, 66, 68, 69, 73, 77, 78, 91

NLFRC Nonlinear Frequency Response Curve. xviii, xix, 13, 14, 39, 44, 45, 50, 53, 54, 57–60, 62, 66, 67, 69, 73, 74

NNM Nonlinear Normal Mode. 3, 14–16

RFS Restoring Force Surface. 3

SDOF Single Degree-of-Freedom. 8, 10, 12

SS State-Space. ix, 4, 5, 63–71, 73

Chapter 1

Introduction

1.1 Motivation

The main purpose of system identification is the everlasting improvement of vibrating structures. The reconciliation of the numerical predictions, from the mathematical model, and the experimental observations, from input and output measurements performed on the real structure, allows for its further development. In the aircraft industry, Ground Vibration Test (GVT) aims to perform this evaluation at a large scale, and with the European aircraft industry requiring for costs and time reduction without diminishing the accuracy of the data, swept-sine excitation has emerged as a promising excitation signal for this structural acquisition. In this realm, an accurate estimation and processing of the response is key, especially, due to the inherent disturbances during testing. Two techniques, the Harmonic Estimator and the Digital Tracking Filter (DTF) have demonstrated to give accurate results of the measured amplitude and phase of the response, for this specific type of excitation. Between the two methods, the DTF has shown to reject more efficiently disturbances in the signal [1].

Nonlinearities are inherent in real world structures, and even though the approximation of these systems as linear has allowed great improvements on structural analysis, addressing nonlinear effects is vital to understand and improve the performance of any structure. Ordinary sources of nonlinearity in the aerospace industry can be backlash and friction in control surfaces, engine-to-pylon connections and saturation effects in hydraulic actuators.

The most relevant nonlinear phenomenon for this work is the multi-harmonic response to a single-harmonic excitation. While the response of a linear structure appears only at the frequency of the force ω, called fundamental frequency, a nonlinear structure vibrates also at integer multiples of ω, $n \times \omega$, called harmonics. The impact of the higher order harmonics on the measured response can be considerable, therefore their identification is mandatory. The extension of the DTF for multi-harmonic nonlinear responses is the objective of this dissertation, expanding the amplitude and phase estimations to the higher-orders. This poses a challenge, since the overall reduced content makes them more subjec-

tive to disturbances in experimental testing. In this aspect, it is important to examine if the great noise attenuation capabilities of the DTF are translated to its multi-harmonic equivalent.

1.2 State of the Art

In the field of nonlinear system identification, unlike its linear counterpart, the analytical prediction of the behaviour of the system is not possible. Therefore, only through experimental testing can a structural dynamicist characterize the structure in study. There are three steps in this process:

- Detection - determine the presence of nonlinearity in the structural behaviour;
- Characterization - location, type and functional form of the nonlinearity;
- Parameter Estimation - estimation of the nonlinearity model coefficients.

A more detailed study on nonlinear system identification and its evolution can be found in [2, 3].

1.2.1 Detection

Many assumptions that act as the foundation for the analysis of linear systems do not apply to their nonlinear counterparts. The violation of the superposition can be a prime indicator of nonlinearity presence. Considering the responses $y_1(t)$ and $y_2(t)$ of a structure to the input forces $x_1(t)$ and $x_2(t)$, respectively. The principle of superposition is violated if $\alpha y_1(t) + \beta y_2(t)$ is not the structural response to the input $\alpha x_1(t) + \beta x_2(t)$.

Additionally, for swept-sine excitation, the peculiarities of nonlinear phenomena can also act in favor of its detection, such has the visual inspection of the hardening/softening effects or jump phenomena in resonance. Hysteresis phenomena is also visible in resonance when contrasting the sweep-up and sweep-down responses in swept-sine excitation. Additionally, the multi-harmonic response to single-harmonic excitation is another nonlinear dynamic behaviour, the detection can be made by either visualization of the sinusoidal wave, although it may be harder to verify due the noise presence, or by the unsymmetrical overall response of the signal. These definitions and examples of these phenomena will be manifested throughout this dissertation.

Numerical approaches in the detection step include the ordinary coherence function. This function, ranges from 0 to 1, and it is required to be unity if and only if the system is linear and noise-free. It can be a convenient and rapid detection tool for nonlinear behaviour; however, it is unable to distinguish between the cases of a nonlinear system and noisy signals [4]. The Hilbert transformation is another technique that diagnoses the nonlinearities based on the measured Frequency Response Function (FRF) data [5].

1.2.2 Characterization

To characterize a nonlinear system, the location, type, and functional form of all nonlinearities present in the system must be determined. Prior to parameter estimation, it is essential to accurately characterize

the nonlinear elastic and dissipative behavior of the physical structure and the identification method will fail if the nonlinear mechanisms involved are not understood. This step of the identification procedure is truly difficult since nonlinearity can originate from a wide range of sources and produce a wide range of dynamic phenomena.

Analysing the deformation shapes of the modes that are most corrupt by the nonlinear response can indicate the location, as the biggest relative displacement of these mode shapes may point out to the nonlinearity source.

There are several aspects that amount to the type of the nonlinearity: if it comes from stiffness and/or damping, hardening or softening characteristics, symmetric or asymmetric, smooth or non-smooth restoring force and weak or strong nonlinearity. These aspects may be retrieved by looking at the distortions in measured FRFs of nonlinear systems. However, because one class of nonlinearity can behave like another in a certain input–output amplitude range, this method is not always conclusive of a particular nonlinearity. At last, the functional form is the last step of characterization. Polynomial expansion is the broader attempt to solve the task at hand. Nevertheless, some structures cannot necessarily be modeled accurately even with high-order polynomial or even by integer power series.

These characterization step can be very ambiguous and can be answered by some of the tools detailed in the parameter estimation step.

1.2.3 Parameter Estimation

In the last step of nonlinear system identification, numerous tried-and-true techniques for parameter estimation are listed. It is also possible to group them as:

- By-passing nonlinearity - linearisation: the tools of structural linear analysis, like modal analysis, are very effective. Applying them directly to nonlinear systems would provide a linear system that explains and approaches the nonlinear system best. However, the nonlinear system deeply changes its response as the level of excitation increases. The obtained linear model is then invalid. With modifications on this approach, the techniques of equivalent linearisation, introduced by Caughey [6] and statistical linearisation, found in Roberts and Spanos [7], were developed.
- Time Domain methods: the data is analysed through its time series. In this category, the Restoring Force Surface (RFS) method, initiated by Masri and Caughey [8], has proven to be a strong addition to the toolbox of a structural dynamicist. Other examples include the NARMAX method, developed by Leontaritis and Billings [9] [10].
- Frequency Domain methods: this time, the data is processed in the frequency domain, taking the form of FRFs or spectra. A few examples are the Voltera and Wiener series, as described in Schetzen [11], and the reverse path method [12].
- Modal methods: with the use of the concept of Nonlinear Normal Mode (NNM), approached in subsection 2.1.2, it is possible to extend modal analysis to nonlinear systems.

- Time-frequency analysis: time–frequency transformations aid in understanding the dynamics of nonlinear systems. Some established methods in this category include the wavelet and Hilbert transforms [13, 14].
- Black-box methods: these methods are applied in the absence of proper nonlinearity characterisation. Without prior knowledge of the structure, the methods take advantage of flexible mathematical structure to capture all relevant physics in measured data. From there, mapping to the outputs of the system can be performed with artificial neural networks, fuzzy networks, statistical learning theory and kernel methods.
- Structural model updating: employing a Finite Element Method (FEM), improvements on this model are made in order to approximate the predictions of this model to the experimental results.

1.3 Objectives

The current work pivots on the multi-harmonic identification of nonlinear systems and the possible applications in the nonlinear system identification field. The followings objectives trace the path to achieve said goals:

- Understand nonlinear dynamics and the consequent nonlinear effects on the modal behavior of a structure;
- Conduct experimental campaigns to collect data with strong nonlinear effects from a mock-up airplane;
- Extend the methods for linear system identification, namely the DTF, to nonlinear cases;
- Apply the developed method to nonlinear simulation data from numerical solvers;
- Apply the developed method to the measured data;
- Compare the developed method with other state of the art methods;
- Create a multi-harmonic modal State-Space (SS) model with the estimations with the developed method.

1.4 Thesis Outline

The structure of this thesis can be divided into seven parts:

- Chapter 1: the motivation and objectives behind this work are clearly detailed. Additionally, the layout of the present document is defined;
- Chapter 2: an introduction of the most important concepts required for the development of this work is made. Not only regarding the dynamics of linear and nonlinear systems but also the techniques and theorems behind the developed method;

- Chapter 3: the implementation of the developed method is described in detail, with particular focus on offline processing;
- Chapter 4: application of the method on simulation data and consequent results discussion. The results are compared with other state of the art methods;
- Chapter 5: application of the method on measured data from experimental tests and consequent results discussion. The results are compared with other state of the art methods;
- Chapter 6: the procedure for multi-harmonic modal State-Space model is described in detail, along with key guidelines. A synopsis of the techniques used in this procedure is also written. A lumped parameter simulated model and a demo airplane experimental setup are modelled and simulated responses obtained. These results are discussed;
- Chapter 7: the work of this dissertation is recapped along with its contributions to the state of the art. Directions for future improvements/developments are listed.

Chapter 2

Theoretical Background

2.1 Linear and Nonlinear Dynamics

2.1.1 Modal Analysis

Modal analysis allows the determination of the dynamical behaviour of a mechanical structure under dynamic loading conditions. This process translates the complex structure's response into a set of vibration characteristics: natural frequencies, mode shapes and damping factors.

Before introducing the process of modal analysis, analytical and experimental, it is first convenient to establish the concept of Degree-of-Freedom (DOF). Every deformable structure is composed of infinite number of infinitesimal rigid body masses, therefore all structures have an infinite number of DOFs that allow the location and definition of the structure and its mass in space and time. From this, a faithful approximation of such structure can be made with a finite number of DOFs, n. The dimension of the analytical mass, stiffness, and damping matrices, as well as the number of hypothetically existing natural frequencies and mode shapes, are all defined by n. Furthermore, Experimental Modal Analysis (EMA) will include a n_i input DOFs, where the input forces are applied and n_o output DOFs where the response of the structure is recorded [15].

Analytical Modal Analysis

There are several assumptions for modal analysis theory [15]:

- linear superposition: the response of the system to any combination of loads equals the sum of the individual responses to each of the loads acting separately. Therefore, mathematically, the dynamics can be represented by linear, second order differential equations.
- time invariance: the dynamic characteristics are invariable with respect to time. Mathematically, the coefficients of the differential equations are constants.
- Maxwell's reciprocity principle states that the response at A due to input at B is the same as

response at B due to input at A. This assumption translates to symmetric mass, stiffness and damping matrices.

Starting in the simplest case to analyse, a Single Degree-of-Freedom (SDOF) system. The equilibrium between inertial, damping, elastic and external forces is expressed in the equation of motion:

$$m\ddot{x}(t) + c\dot{x}(t) + kx(t) = f_{ext}(t) \tag{2.1}$$

The system is represented by a mass m, spring with constant k and a damper with coefficient c. The displacement, velocity and acceleration of the mass are portrayed in $x(t)$, $\dot{x}(t)$ and $\ddot{x}(t)$, respectively. These three just mentioned variables and also the external force, $f_{ext}(t)$, are, of course, a function of time, t.

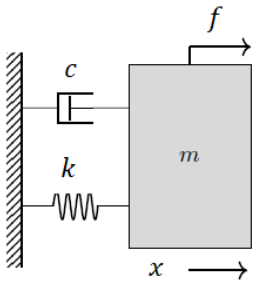

Figure 2.1: Diagram of a SDOF system.

Transforming the time domain into the Laplace domain, variable s, assuming the free vibration response has died out, it is possible to rewrite Equation 2.1:

$$\left(ms^2 + cs + k\right) X(s) = F(s) \tag{2.2}$$

And also define the dynamic stiffness $Z(s)$:

$$Z(s)X(s) = F(s) \tag{2.3a}$$

$$Z(s) = \left(ms^2 + cs + k\right) \tag{2.3b}$$

Inverting Equation 2.3a provides:

$$X(s) = H(s)F(s) \tag{2.4}$$

With the complex valued transfer function $H(s)$:

$$H(s) = Z^{-1}(s) = \frac{1/m}{s^2 + (c/m)s + k/m} \tag{2.5}$$

The denominator of the transfer function designate the characteristic equation of the system, and its roots, are the poles of the system, $\lambda_{1,2}$:

$$\lambda_{1,2} = -\frac{c}{2m} \pm \sqrt{\left(\frac{c}{2m}\right)^2 - \frac{k}{m}} \tag{2.6}$$

From Equation 2.6, some important concepts can be mathematically defined. First, if the system is conservative, i.e. disregarding damping, $c = 0$, the undamped natural frequency w_n, the frequency at which a system tends to oscillate in the absence of any driving force, is calculated as:

$$w_n = \sqrt{\frac{k}{m}} \tag{2.7}$$

The critical damping c_{cr} is obtained equaling to zero the term under the square root in Equation 2.6:

$$c_{cr} = 2m\sqrt{\frac{k}{m}} \tag{2.8}$$

From this, the damping ratio ζ is defined as:

$$\zeta = \frac{c}{c_{cr}} \tag{2.9}$$

Also, Equation 2.6 yields in the time domain a solution of homogeneous system equation:

$$x(t) = x_1 e^{\lambda_1 t} + x_2 e^{\lambda_2 t} \tag{2.10}$$

The critical damping acts as the threshold value between overdamping and underdamping. Systems with $\zeta > 1$ are classified as overdamped, if $\zeta = 1$ critically damped and if $\zeta < 1$ underdamped. The response of overdamped systems consists of decay only with no tendency to oscillate, returning to its equilibrium position. Critically damped systems return to their equilibrium position as quickly as possible, without oscillating, forming the border case between over and underdamped systems. Henceforth, only the underdamped case will be considered, in which case, Equation 2.6 yields two complex conjugate roots, where σ_1 is the damping factor and ω_d the damped natural frequency, also known as resonance:

$$\lambda_1 = \sigma_1 + j\omega_d \quad and \quad \lambda_1^* = \sigma_1 - j\omega_d \tag{2.11}$$

The transfer function can be rewritten as:

$$H(s) = \frac{1/m}{(s - \lambda_1)(s - \lambda_1^*)} \tag{2.12}$$

Having applied partial fraction expansion, where A_1 and A_1^* are the residues:

$$H(s) = \frac{A_1}{(s - \lambda_1)} + \frac{A_1^*}{(s - \lambda_1^*)} \quad with \quad A_1 = \frac{1/m}{j2\omega_d} \tag{2.13}$$

The transfer function, i.e. the relation between the input force and the displacement can be translated to the frequency domain. The transfer function evaluated along the frequency axis ($j\omega$) is called the Frequency Response Function (FRF):

$$H(s)|_{s=j\omega} = H(\omega) = \frac{A_1}{(j\omega - \lambda_1)} + \frac{A_1^*}{(j\omega - \lambda_1^*)} \tag{2.14}$$

In Figure 2.2 it is possible to observe a generic FRF of SDOF system, after the transform of the complex valued response from Equation 2.14 to amplitude and phase.

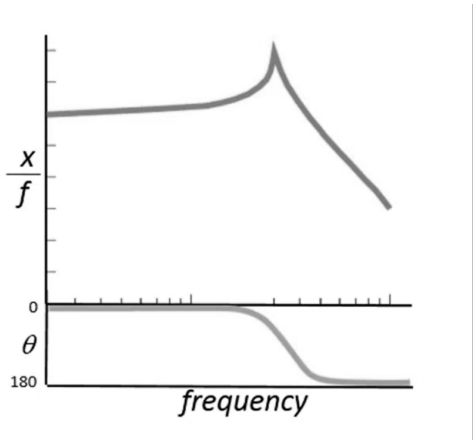

Figure 2.2: Example of an FRF for an SDOF system.

The observed peak in the amplitude, accompanied by a shift in the phase response, corresponds to the resonance frequency. It is also important to remark that the resonance frequency, in this case the damped natural frequency, is proportional to the undamped natural frequency, $w_d = w_n\sqrt{1-\zeta^2}$. Thus meaning that if damping is disregarding, $\zeta = 0$, the resonance assumes the value of the undamped natural frequency.

As previously stated in the introductory chapters of the present subsection, it is required to describe the majority of systems under analysis with several DOFs. Such Multiple Degree-of-Freedom (MDOF) system behaviour can be described with n equations of motion. Subsequently, the translation to matrix notation of such equations leds to:

$$[M]\{\ddot{x}(t)\} + [C]\{\dot{x}(t)\} + [K]\{x(t)\} = \{f_{ext}(t)\} \tag{2.15}$$

The mass $M \in \mathbb{R}^{n\times n}$, damping $C \in \mathbb{R}^{n\times n}$ and stiffness $K \in \mathbb{R}^{n\times n}$ matrices are symmetric. The displacement is represented by $x(t) \in \mathbb{R}^{n\times 1}$, velocity by $\dot{x}(t) \in \mathbb{R}^{n\times 1}$, acceleration by $\ddot{x}(t) \in \mathbb{R}^{n\times 1}$ and force vector by $f_{ext}(t) \in \mathbb{R}^{n\times 1}$.

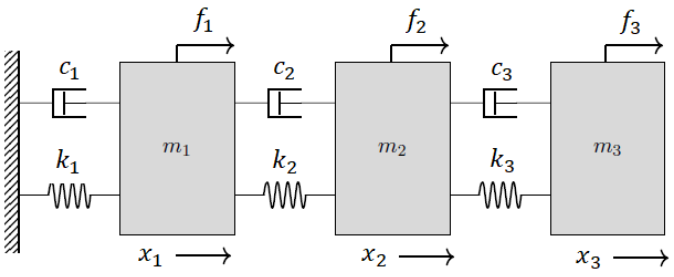

Figure 2.3: Free Body Diagram of a three DOF system.

Translating Equation 2.15 to the Laplace domain:

$$\left([M]\,s^2 + [C]\,s + [K]\right)\{X(s)\} = \{F(s)\} \tag{2.16}$$

Defining the dynamic stiffness matrix, $Z(s) \in \mathbb{C}^{n\times n}$:

$$[Z(s)]\,\{X(s)\} = \{F(s)\} \tag{2.17a}$$

$$[Z(s)] = \left([M]\,s^2 + [C]\,s + [K]\right) \tag{2.17b}$$

Inverting Equation 2.17a provides:

$$\{X(s)\} = [H(s)]\,\{F(s)\} \tag{2.18}$$

With the complex valued transfer function matrix $H(s) \in \mathbb{C}^{n\times n}$, where $adj(Z(s))$ is the adjoint matrix of $Z(s)$:

$$[H(s)] = [Z(s)]^{-1} = \frac{adj\,([(Z(s)])}{|Z(s)|} \tag{2.19}$$

The denominator of the transfer function matrix is the characteristic equation of the system. The roots of this equation contain the poles of the system that define the natural frequencies and damping ratio. To determine these roots, Equation 2.17a is transformed into an eigenvalue problem formulation, with the aid of the identity $(s\,[M] - s\,[M])\{X(s)\} = 0$:

$$(s\,[A] + [B])\{Y\} = \{F'\} \tag{2.20}$$

Where:

$$A = \begin{bmatrix} 0 & M \\ M & C \end{bmatrix} \qquad B = \begin{bmatrix} -M & 0 \\ 0 & K \end{bmatrix} \qquad Y = \begin{bmatrix} sX \\ X \end{bmatrix} \qquad F' = \begin{bmatrix} 0 \\ F \end{bmatrix} \tag{2.21}$$

If the force vector is null, the result is a generalized eigenvalue problem with real valued matrices:

$$(s\,[A] + [B])\{Y\} = 0 \tag{2.22}$$

This generates $2\times n$ complex valued eigenvalues, appearing in complex conjugate pairs, λ_1 to λ_n and λ_1^* to λ_n^*, in which, once again, the damping factor is the real part of the pole whilst the imaginary part corresponds to the damped natural frequency. Associated with each eigenvalue is an eigenvector. These eigenvectors portray the concept of mode shape vectors, or modal vectors, ψ, that also appear in complex conjugate pairs. Physically, a mode shape is the shape of the deformed system when excited by a dynamic force at the same frequency as the natural frequency of the structure. The transfer function matrix $H(s)$, expressed in terms of the poles of the system yields, where E is a constant:

$$[H(s)] = \frac{adj\,([(Z(s)])}{\prod_{r=1}^{n} E(s-\lambda_r)(s-\lambda_r^*)} = \frac{adj\,([(Z(s)])}{\prod_{r=1}^{2n} E(s-\lambda_r)} \tag{2.23}$$

Employing partial fraction expansion, where A_r and A_r^* are the residues:

$$[H(s)] = \sum_{r=1}^{n} \left(\frac{[A_r]}{s - \lambda_r} + \frac{[A_r^*]}{s - \lambda_r^*} \right) \tag{2.24}$$

Making $s = j\omega$ Equation 2.24 provides the FRF of the system, as a sum of the FRFs of n SDOF systems.

Experimental Modal Analysis

Analytically calculating the modal parameters of complex structures can be very challenging due to the difficult description of the structure into M, C and K matrices. Also, as previously stated, for theoretical modal analysis, linearity is required and with the focus of this thesis on nonlinear systems there is a need to estimate the modal parameters of the structure via other methods.

Experimental Modal Analysis (EMA) starts with excitation of the structure under test. The input force is applied to the structure in a certain location and direction, and the amount of force used for each measurement is precisely recorded. After, it is possible to calculate the FRF combining the input force measurement, input, that acts as the reference, with the series of response measurements, output. The typical output used in EMA is the acceleration output.

Ultimately, the FRFs are complex frequency domain functions, with amplitude and phase information, that describe how the structure moves at each measurement location per unit force at the input location. The modal parameters, natural frequencies, damping ratios and mode shapes are included in the FRFs. More information on this parameterisation from the FRFs can be found in Heylen et al. [15].

The H_1 estimator is the most employed algorithm to compute the FRFs. It assumes no noise on the input and minimizes uncorrelated noise in the output. It has a tendency to underestimate the amplitude at resonance, resulting in damping overestimation. Its calculation is done according to:

$$[H_1(\omega)] = [G_{XF}(\omega)] \, [G_{FF}(\omega)]^{-1} \tag{2.25}$$

$H_1 \in \mathbb{C}^{n_o \times n_i}$ requires a posterior translation into amplitude and phase from the complex domain for a clearer system's behaviour interpretation. In the end, there is n_i FRFs for each output DOF.

The output-input cross-power matrix $G_{XF} \in \mathbb{C}^{n_o \times n_i}$ and input auto-power matrix $G_{FF} \in \mathbb{C}^{n_i \times n_i}$ can be obtained:

$$[G_{XF}(\omega)] = [X(\omega)] \, [F(\omega)]^T \tag{2.26a}$$

$$[G_{FF}(\omega)] = [F(\omega)] \, [F(\omega)]^T \tag{2.26b}$$

$X(\omega) \in \mathbb{C}^{n_o \times n_{sw}}$ and $F(\omega) \in \mathbb{C}^{n_i \times n_{sw}}$ contain the amplitude and phase information of the output and input measurements in the complex domain, with n_{sw} referring to the number of sweeps, or runs, in the testing acquisition. To accurately process the FRFs, the input auto-power matrix must be non-singular, therefore the number of performed sweeps must be at least equal to the number of input forces applied to the system, $n_{sw} \geq n_i$. The forces of each sweep cannot be correlated either, that is, the excitation

configuration needs to change from one sweep to another [16].

2.1.2 Nonlinear Dynamics

Nonlinearity is inherent in real world systems. At small amplitudes, the system can be approximated as linear as the nonlinearity sources are not activated. Nonetheless, the transition to a nonlinear system occurs if these are activated by higher excitations. In this nonlinear domain, many of the concepts and techniques risen by modal analysis are not applicable, and any attempt to do so will result in suboptimal design, since linear superposition introduced in the beginning of section 2.1.1 cannot be extended to nonlinear systems. Consequently the concept of FRF needs adaptation, rendering a different frequency response per level of excitation. The equivalent term for nonlinear systems can be defined as Nonlinear Frequency Response Curve (NLFRC) [2].

Attempts have been made to lineariase nonlinear systems, since these simplified models are preferred by the industry where modal analysis techniques are embedded. Nevertheless, there is an ultimate need to accurately portray nonlinear models and the first step is to interpret the peculiar dynamics and phenomena associated with nonlinear systems.

Regarding the model of these nonlinear systems in the equation of motion, the nonlinearity is introduced by f_{nl}, the nonlinear restoring force vector :

$$[M]\{\ddot{x}(t)\} + [C]\{\dot{x}(t)\} + [K]\{x(t)\} + \{f_{nl}(x(t), \dot{x}(t))\} = \{f_{ext}(t)\} \tag{2.27}$$

Moving forward, the following 2 DOF system with a cubic spring is defined, in order to illustrate the phenomena and features of a nonlinear system:

$$\ddot{x_1} + (2x_1 - x_2) + 0.5x_1^3 = F\cos\omega t \tag{2.28a}$$

$$\ddot{x_2} + (2x_2 - x_1) = 0 \tag{2.28b}$$

This example system and its dynamics are featured in Kerschen et al. [17]. Computation and numerical methods for this system are broadly approached in the same article.

Dynamical Features and Phenomena

First, the frequency-energy dependence of free oscillations is a dynamical feature of nonlinear responses. Increase in amplitude/energy will increase the frequency of response of an unforced nonlinear system with hardening properties. The frequency decreases for systems with softening properties. This dynamics leads to instability of the free periodic responses of undamped nonlinear oscillators, the non-existence of analytic solutions for free damped nonlinear responses and complex nonlinear phenomena in the unforced dynamics, such as nonlinear mode localisation in periodic arrays of nonlinear oscillators [17].

To better interpret nonlinear phenomena, the extension of Linear Normal Mode (LNM) to the nonlinear domain needs to be made. Physically, LNM is the vibration in unison of a conservative system, where all material points of the system reach their extreme values and pass through zero simultaneously, with a fixed, linear relation between the displacements of each point. LNM are also orthogonal, the excitation of one mode will never cause motion of a different mode.

The definition of Nonlinear Normal Mode (NNM) was pionereed by Rosenberg [18, 19], as a vibration in unison of the sytem with a nonlinear relation between the displacements, and later continued by Shaw and Pierre [20] with the inclusion of the invariant manifold approach. Ultimately, Kerschen et al. [17] extended this definition to a non necessarily synchronous periodic motion of the conservative system. The frequency of motion of the material points does not need to be equal and the relations between the displacements linear. Figure 2.4 not only shows the nonlinear displacement relation, by visualization of the configuration space, but also hints at another dynamics of nonlinear systems response: the time series of the displacement x_1 defines a sinusoidal response that is clearly composed by multiple harmonics.

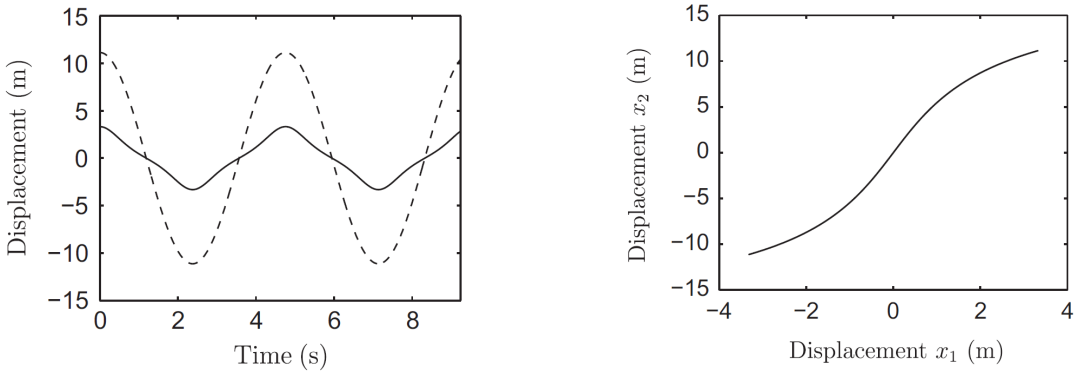

(a) Time series (— x_1, - - x_2)

(b) Configuration space

Figure 2.4: NNMs of the nonlinear system of Equation 2.28 in free vibration [17].

One of the properties of NNMs is the frequency-energy dependence of their oscillations. The modal curves and frequencies of oscillation depend on the total energy of the system, preventing the direct separation of space and time in the equation of motion of the system and its analytical calculation and also rendering invariant the FRFs of nonlinear systems. In Figure 2.5 the NLFRCs of a system in Equation 2.28, that possesses hardening properties, is observed. The increase in forcing amplitude leads to further separation from the peak of the smallest amplitude, that can be approximated as linear, and the subsequent increase in the resonance frequency.

The representation of this property is most clear in a Frequency-Energy Plot (FEP). In a FEP, NNM motion is represented by a point, attached to the corresponding frequency of motion and total conserved energy in the system. The solid lines represent a branch, that is, a family of NNM motions with the same qualitative features.

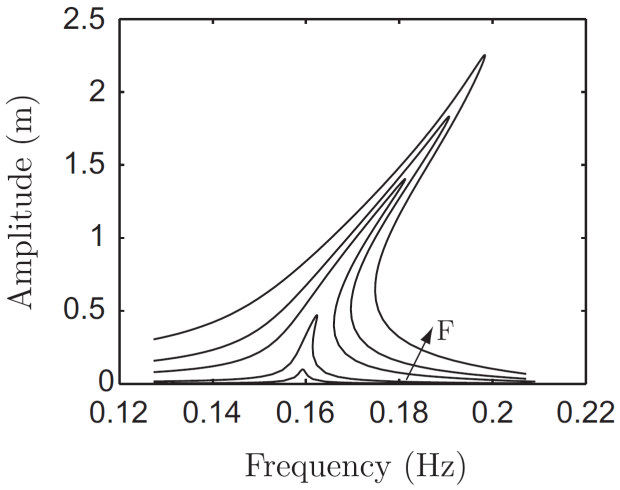

Figure 2.5: NLFRCs of system in Equation 2.28, with added damping, as the level of excitation increases [17].

In the following image, the FEP of the system in Equation 2.28 is observed. The branches $S11+$ and $S11-$ represent the in-phase and out-of-phase synchronous NNMs, respectively. The letter S refers to symmetric periodic solutions, while unsymmetric periodic solutions are denoted by the letter U. The indices in notation reference the relation between the frequency of motion of the two DOFs. The con-

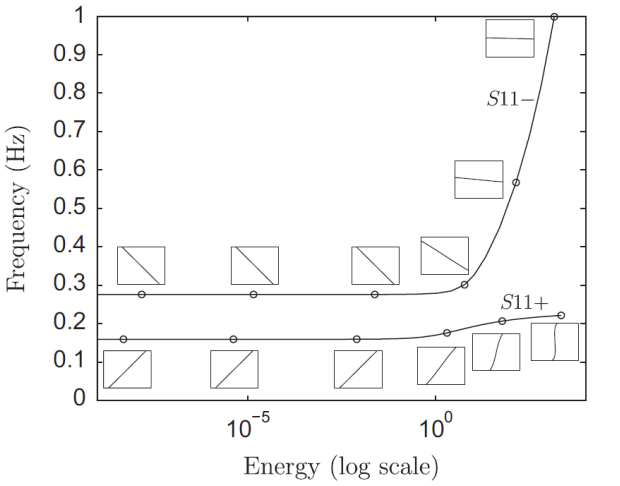

Figure 2.6: FEP of system in Equation 2.28 in free vibration [17].

figuration space is also attached to the corresponding NNM. The interpretation of this FEP evidentiates the frequency-energy dependence of NNMs, as they can be approximated as linear at small energy values. When the energy increases the frequency of these NNMs also increases for both branches and the configuration spaces indicate nonlinear relations between the displacements of the 2 DOFs.

Another property of NNMs is that they may interact during general motion of the system. Modal interactions may result in internally resonant frequencies due to energy exchange between the different

modes, in a reversible or irreversible fashion. For the same nonlinear system, the FEP in Figure 2.7 shows the appearance of another branch of periodic solutions for higher energy values. This branch, termed tongue, emerges from the backbone branch $S11+$. On this tongue, there is a 3:1 internal resonance between the in-phase and out-of-phase NNMs. Both the FEP and the time series for this 3:1 internal resonance are pictured below.

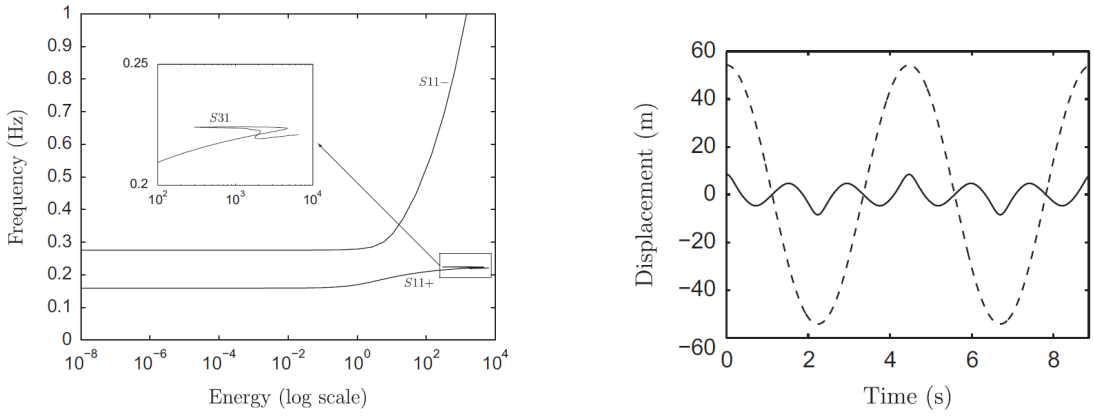

(a) FEP

(b) Time series (— x_1, - - x_2)

Figure 2.7: FEP and time series featuring a 3:1 internal resonance of system in Equation 2.28 in free vibration [17].

The third property of NNMs is that they can exceed in number of DOFs in the system, due to mode bifurcations that lead to mode instabilities and bifurcating branches of nonlinear localised modes. Bifurcation occurs when different dynamics develop in the vicinity of a point in space.

The aforementioned dynamic features and NNMs properties contribute to the following dynamics only associated with nonlinear systems:

- Multiple co-existing stable equilibrium positions;
- Chaotic motion, that possess unpredictable, irregular and random-like dynamic behaviour;
- Multi-harmonic response for single-harmonic input;
- Harmonic excitation may lead to forced resonances, such as subharmonic, superharmonic, combination or autoparametric resonances;
- Sudden nonlinear transitions, also known as jumps, caused by nonlinear hysteresis phenomena. These jumps are essentially transitions between co-existing stable branches of solutions that may result in swift changes in amplitude and phase of the motion for abrupt variations of the excitation frequency. In Figure 2.8, two jumps are perceptible in the vicinity of resonance, for a softening nonlinearity. The I-II jump occurs for a forward sweeping frequency and jump III-IV for backward sweeping.

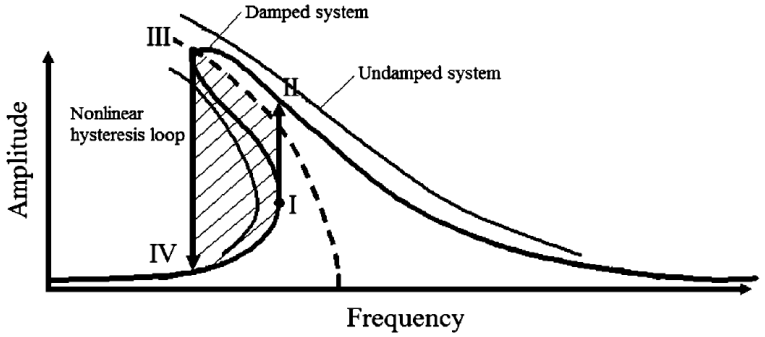

Figure 2.8: Nonlinear jump phenomena [17].

2.1.3 Dynamic Forcing

In experimental modal analysis, in order to evaluate the response of the structure it is first needed to excite the structure. There are several types of excitation signals waveforms, such as random-stochastic signals that include pure random excitation and pseudo random. Also, there are periodic signals like multi-sine signals and transient signals like swept-sine signals.

As stated before, the current thesis pivots on swept-sine excitation. In the analysis of aerospace structures, swept-sine excitation provides a good trade-off between magnitude of excitation level needed for large aircraft and testing time. Additionally, it allows for the excitation of all resonances of the structure in the frequency range of the forcing excitation [21].

A swept-sine signal is a sinusoidal signal whose frequency increases, sweep-up, or decreases, sweep-down. The excitation force can be written as:

$$f(t) = F(t)\sin(\varphi(t)), \qquad \dot{\varphi}(t) = \omega(t) \tag{2.29}$$

$F(t)$ represents the amplitude of the signal. The phase of the signal, $\varphi(t)$ is the derivative of the instantaneous angular frequency $\omega(t)$. The time evolution of $\omega(t)$, besides increasing or decreasing, can also be linear or logarithmic. For a linear sweep it yields:

$$\omega(t) = \omega_s + at, \qquad a = \frac{\omega_e - \omega_s}{T} \tag{2.30}$$

The linear sweep rate, a, expressed in rad/s^2, is a function of the start frequency, ω_s and the end frequency, ω_e, over the excitation time period T. Therefore, the excitation can be calculated according to these parameters as follows:

$$f(t) = F(t)\sin\left(\frac{a}{2}t^2 + \omega_s t + \varphi_0\right) \tag{2.31}$$

The instantaneous angular frequency of the logarithmic sweep, the most commonly applied in the current

work, is calculated by:

$$\omega(t) = \omega_s 2^{St/60} \tag{2.32}$$

Where the logarithmic sweep rate, represent by S, is expressed in octaves per minute. Thus leading to a logarithmic sweep excitation function:

$$f(t) = F(t)\sin\left(\frac{60\omega_s}{S\ln(2)}(2^{St/60} - 1) + \varphi_0\right) \tag{2.33}$$

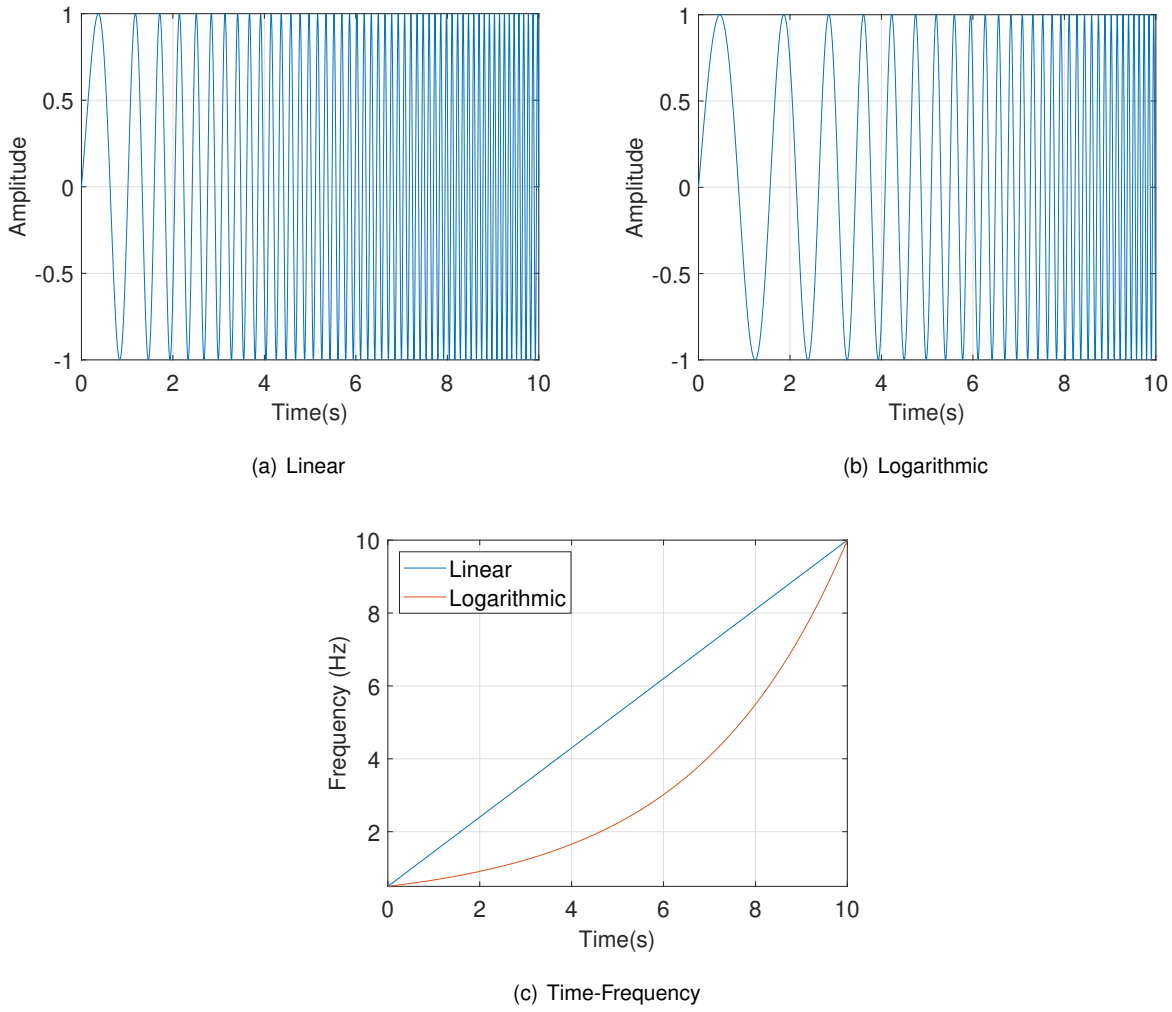

(a) Linear

(b) Logarithmic

(c) Time-Frequency

Figure 2.9: Logarithmic and linear swept-sine signals.

2.2 Harmonic Balance Method

The Harmonic Balance (HB) method is a numerical approximation method that is able to compute steady-state periodic solutions of the dynamics of nonlinear systems, described by ordinary differential equations. It provides computational efficiency, reduced numerical instability and computation of physically unstable conditions [22].

As introduced before, it is possible to describe a nonlinear dynamical system with n DOFs through the following equation of motion:

$$[M]\{\ddot{x}(t)\} + [C]\{\dot{x}(t)\} + [K]\{x(t)\} = \{f(x(t), \dot{x}(t), \omega, t)\} \tag{2.34a}$$

$$where \quad \{f(x(t), \dot{x}(t), \omega, t)\} = \{f_{ext}(\omega, t)\} - \{f_{nl}(x(t), \dot{x}(t))\} \tag{2.34b}$$

M, C and K portray the mass, damping and stiffness matrices, respectively. The two vectors, $x(t)$ and $f(x, \dot{x}, \omega, t)$, both periodic, can be approximated by Fourier Series truncated to the n_h^{th} harmonic:

$$x(t) = \frac{c_0^x}{\sqrt{2}} + \sum_{k=1}^{n_h} \left(s_k^x \sin(\frac{k\omega t}{\nu}) + c_k^x \cos(\frac{k\omega t}{\nu}) \right) \tag{2.35}$$

$$f(t) = \frac{c_0^f}{\sqrt{2}} + \sum_{k=1}^{n_h} \left(s_k^f \sin(\frac{k\omega t}{\nu}) + c_k^f \cos(\frac{k\omega t}{\nu}) \right) \tag{2.36}$$

In Equation 2.35 and Equation 2.36, the integer ν accounts for sub-harmonics of the excitation frequency ω and s_k and c_k represent the vectors of the Fourier coefficients associated to the sine and cosine terms, respectively. The new unknowns of the problem are the Fourier coefficients of the displacement $x(t)$. It should also be known that the coefficients of $f(t)$, s_k^f and c_k^f, are dependent on s_k^x and c_k^x. All these coefficients can be arranged into $(2n_h + 1)$ $n \times 1$ vectors:

$$z = \begin{bmatrix} (c_0^x)^T & (s_1^x)^T & (c_1^x)^T & ... & (s_{n_h}^x)^T & (c_{n_h}^x)^T \end{bmatrix}^T \tag{2.37}$$

$$b = \begin{bmatrix} (c_0^f)^T & (s_1^f)^T & (c_1^f)^T & ... & (s_{n_h}^f)^T & (c_{n_h}^f)^T \end{bmatrix}^T \tag{2.38}$$

This allows for a more compact representation of displacement and force:

$$x(t) = (Q(t) \otimes I_n) \ z \tag{2.39}$$

$$f(t) = (Q(t) \otimes I_n) \ b \tag{2.40}$$

I_n represents the identity matrix, size *n*, and $\otimes$ the Kronecker tensor product. $Q(t)$ contains the cosine and sine series as follows:

$$Q(t) = \begin{bmatrix} \frac{1}{\sqrt{2}} & \sin(\frac{\omega t}{\nu}) & \cos(\frac{\omega t}{\nu}) & ... & \sin(n_h \frac{\omega t}{\nu}) & \cos(n_h \frac{\omega t}{\nu}) \end{bmatrix} \tag{2.41}$$

From this notation, Equation 2.34 can be compactly written in as Equation 2.42, with all due mathematical justifications demonstrated in [22].

$$h(z, \omega) \equiv A(\omega)z - b(z) = 0 \tag{2.42}$$

The matrix A, $(2n_h+1)n \times (2n_h+1)n$ describes the linear dynamics of the system:

$$A = \nabla^2 \otimes M + \nabla \otimes C + I_{2n_h+1} \otimes K \tag{2.43}$$

In matrix form:

$$A = \begin{bmatrix} K & & & & & \\ & K - \left(\frac{\omega}{\nu}\right)^2 M & -\frac{\omega}{\nu} C & & & \\ & \frac{\omega}{\nu} C & K - \left(\frac{\omega}{\nu}\right)^2 M & & & \\ & & & \ddots & & \\ & & & & K - \left(n_h \frac{\omega}{\nu}\right)^2 M & -n_h \frac{\omega}{\nu} C \\ & & & & n_h \frac{\omega}{\nu} C & K - \left(n_h \frac{\omega}{\nu}\right)^2 M \end{bmatrix} \tag{2.44}$$

Since Equation 2.42 is nonlinear, it has to be solved iteratively, with, for example, a Newton solver. At each iteration, an evaluation of b and of $\frac{\partial h}{\partial z}$ has to be provided. When f has an established analytical sinusoidal expansion and when it can be precisely approximated by a small number of harmonics, along with expression of the Jacobian matrix of the system, the analytical expressions relating the Fourier coefficients of the forces b and of the displacements z can be determined.

A different method is the Alternating Frequency/Time-domain (AFT) technique, with the intent of computing b. More information on this method can be found in Cameron and Griffin [23]. Another efficient alternative, termed trigonometric collocation is explored in Xie and Lou [24], also with further mathematical justifications and procedure in Detroux et al. [22].

At last, since the HB method is computed to only a specific frequency ω, a continuation procedure must be applied and coupled with the HB to ensure the computation over a vast range of frequencies. In Detroux et al. [22], a continuation procedure based on tangent predictions and Moore-Penrose corrections is demonstrated.

2.3 Digital Signal Processing

A signal is defined as any physical quantity that varies with time, space, or any other independent variable or variables. The majority of the signals encountered in research and engineering are analog in nature. These signals are function of a continuous variable, often time, and usually undertake values on a continuous range. Althought, there are tools capable of processing analog signals for diverse applications, frequently these analog signals are converted into digital signals, which are function of a discrete variable, time, with discrete values as well [25].

Since an analog signal is defined at every point in time and value/amplitude, it contains an infinite number of points. Such is not feasible to digitize. Additionally, since processing infinite points requires an endless amount of memory and processing capacity, it is inappropriate to use a digital signal processor or a computer. Sampling resolves this problem by taking samples at the fixed time interval. This sampling

interval or sampling period ΔT is then defined as the time span between consecutive sample points [26].

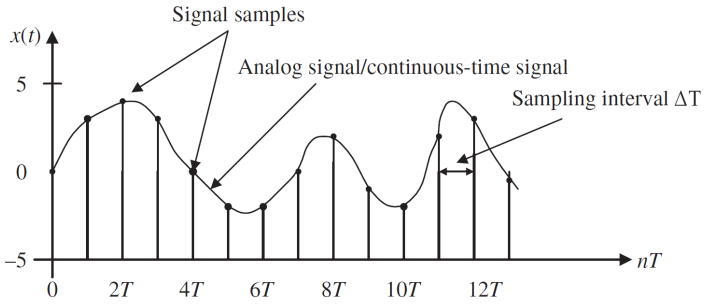

Figure 2.10: Analog signal and display of sampling [26].

Sampling can also be defined by its sampling rate or frequency, f_s, expressed in samples per second or Hz:

$$f_s = \frac{1}{\Delta T} \tag{2.45}$$

One concern that needs to be tackled is that sampling occurs at a high enough rate so that the original analog signal can be reconstructed or recovered and no information is lost. If such is not verified, aliasing occurs, resulting in undesirable signals in the desired frequency band. The Nyquist–Shannon sampling theorem implies that an analog signal must be sampled at least twice of the highest frequency component of the signal, $f_s \geq 2f_{max}$.

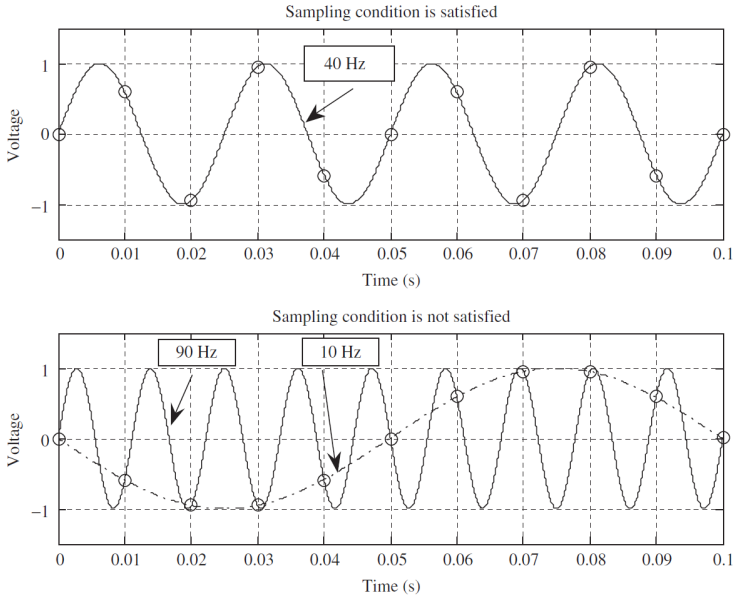

Figure 2.11: Example of appropriately and inappropriately sampled signals [26].

Figure 2.11 portrays two sinusoidal waves where $\Delta T = 0.01s$ and consequently the sampling frequency is 100 Hz. A sine wave with a frequency of 40 Hz and its sampled amplitudes are shown in the first plot of the figure. Since $2f_{max} = 80Hz < f_s$, the sampling theorem condition is met. The circles in the first plot are used to label the sampled amplitudes. Given that the sampled values are clearly originated from the analog representation of the 40 Hz sine wave, it can be concluded that this is sufficiently sampled.

The sine wave with a frequency of 90 Hz is sampled at 100 Hz, as can be seen in the second plot. The signal is undersampled due to $2f_{max} = 180Hz > f_s$. As a result, the requirement of the sampling theorem is not fulfilled. Once again, analysing the sample amplitudes labeled with the circles on the second plot, it cannot be determined if the sampled signal originates from sampling a 90 Hz sine wave (solid line) or a 10-Hz sine wave (dot-dash line). They are not distinguishable, hence, they are aliases of one another. The 10 Hz sine wave is referred in this example as the aliasing noise.

From the Nyquist–Shannon sampling theorem also rises the definition of Nyquist frequency, which is half of the sampling frequency $\frac{f_s}{2}$.

Another important step of the analog to digital conversion is the quantization. It has been seen that a digital signal consists of a series of numbers (samples), each of which is represented by a certain number of digits (finite precision). Quantization is the process of transforming a discrete-time continuous-amplitude signal into a digital signal by representing each sample value as a limited (as opposed to an infinite) number of digits. Quantization error, also known as quantization noise, transpires from the representation of a continuous valued signal by a limited collection of discrete value levels. Nowadays, quantization error is minimized due to large bit levels in today's computing.

2.3.1 Heterodyning

Heterodyning is a processing technique that mixes two different signals. The components from this mixing can be obtained according to the following trigonometrical identity:

$$\sin(\theta_1) \times \sin(\theta_2) = \frac{1}{2}(\cos(\theta_1 - \theta_2) - \cos(\theta_1 + \theta_2)) \tag{2.46}$$

From this equation, acknowledging two signals at frequencies f_1 and f_2, the mixing of these signals generates two new signals. One at the sum of the two original frequencies, $f_1 + f_2$, and other at the difference of the original frequencies, $f_1 - f_2$. These new signal frequencies are labelled heterodynes.

In most applications, including the DTF, this technique is used to shift signals from one frequency range to another, therefore transferring the content of the signal to a frequency where it can be more easily processed, transported or filtered. For this effect, one of the signals to be mixed contains the information, the input signal, whilst the other, the reference signal, is typically a local oscillator.

2.3.2 Digital Filter

Transfer Function

Interpreting $x(n)$ and $y(n)$ as the input and output, respectively, of a Digital Signal Processing (DSP) system, the relation between the output and input can be expressed by the following difference equation [27]:

$$y(n) = b_0x(n) + b_1x(n-1) + ... + b_Mx(n-M) - a_1y(n-1) - ... - a_Ny(n-N) \tag{2.47}$$

where b_i and a_j depict the coefficients of the system and *n* is the time or sample index.

It is observable from Equation 2.47 that the output of this DSP system is the weighted sum of the current and previous input values, $x(n)$ and $x(n-1), ..., x(n-M)$ and the past output values: $y(n-1), ..., y(n-N)$. This processing technique is referred as digital filtering and it can be verified as linear, time invariant and causal.

Starting from the difference equation it is possible to derive the z-transfer function of the filter, which is the ratio of the z-transform of the output and input of the system. The z-transform of a causal sequence $x(n)$, designated by $X(z)$ is defined as:

$$X(z) = \sum_{n=0}^{\infty} x(n)z^{-n} \tag{2.48}$$

After the z-transforms of the $x(n)$ and $y(n)$ the Equation 2.47 can be rewritten::

$$Y(z) = b_0X(z) + b_1X(z)z^{-1} + ... + b_MX(z)z^{-M} - a_1Y(z)z^{-1} - ... - a_NY(z)z^{-N} \tag{2.49}$$

Rearranging this equation:

$$H(z) = \frac{Y(z)}{X(z)} = \frac{b_0 + b_1z^{-1} + ... + b_Mz^{-M}}{1 + a_1z^{-1} + ... + a_Nz^{-N}} = \frac{B(z)}{A(z)} \tag{2.50}$$

The transfer function, termed $H(z)$, represents the digital filter in the z-domain, allowing for better stability and frequency response analysis. In order to verify stability, a translation to the analytical form and multiplication of the numerator and denominator of the transfer function by z^n is made, where *n* is the filter order. This parameter is the largest delay in the difference equation or the largest power of z in the transfer function.

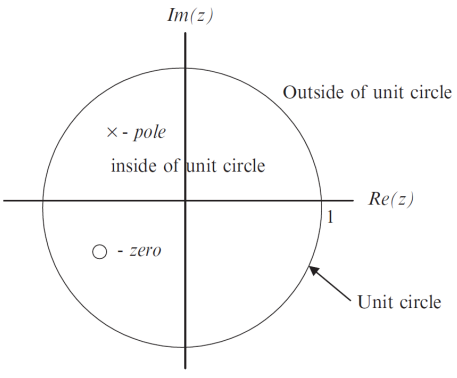

Figure 2.12: z-*domain* and unit circle [27].

The multiplication by the same value on the top and bottom accounts for equality. The locations of the zeros are the roots of our numerator equation, and the poles are the roots of our denominator equation, in analytical form. The magnitudes of the poles must be less than 1 for stability. Poles directly on the unit circle provide for marginal stability and poles outside will cause instability.

Types of Digital Filters

Digital filters can be categorized in four main types, each with a specific application in DSP: lowpass, highpass, bandpass, and bandstop. In general, the passband, stopband, and transition band of the filter frequency response serve as the primary design criterion for the filter. The frequency range where the amplitude gain of the filter response is about equal to one is known as the filter passband, also referred as bandwidth (BW). The frequency range across which the filter magnitude response is attenuated to exclude the input signal whose frequency components fall within that range is known as the filter stopband. The frequency region between the stopband and the passband is referred to as the transition band [27]. In the context of this dissertation, it is important to establish the lowpass filter. Its design criteria and framework are shown in Figure 2.13. As visible from its normalized magnitude response, the low frequency components pass through whilst the high frequency components are filtered. Ω_p and Ω_s represent the cut-off frequency and the stopband cut-off frequency, respectively. Additionally, the design parameter of the ripple (fluctuation) of the frequency response in the passband is δ_p, whereas the ripple in the stopband is specified by δ_s.

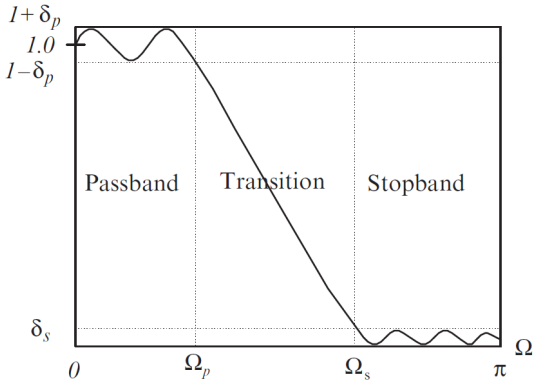

Figure 2.13: Normalized magnitude response of a lowpass filter [27].

Phase Response and Filter Delay

The phase response $\Theta(\omega)$ of a digital filter is defined as the phase (or angle) of the frequency response $H(e^{j\omega T})$, that is given by its transfer function $H(z)$ evaluated on the unit circle [28]:

$$\Theta(\omega) = \angle H(e^{j\omega T}) \tag{2.51}$$

The real-valued phase response $\Theta(\omega)$ gives the radian phase shift added to the phase of each sinusoidal component of the input signal. It is often more intuitive to consider instead the phase delay $P(\omega)$, defined as:

$$P(\omega) = -\frac{\Theta(\omega)}{\omega} \tag{2.52}$$

The phase delay gives the time delay in seconds experienced by each sinusoidal component of the input signal. That is, the offset between the input and output of the phase. Group delay $D(\omega)$, a more common representation of filter phase response, may be interpreted as the time delay of the amplitude envelope of a sinusoid at frequency ω:

$$D(\omega) = -\frac{d}{d\omega}\Theta(\omega) \tag{2.53}$$

It is the offset between input and output amplitude envelope.

Chapter 3

Multi-Harmonic Digital Tracking Filter

The capability of tracking the amplitude and phase of the multi-harmonic response of a nonlinear system is paramount in the detection of modal interactions and the overall understatement of said structure. The proposed technique for this tracking, particular to structures subjected to sinusoidal excitation with a known frequency content over time, such as swept-sine excitation, is the Multi-Harmonic Digital Tracking Filter (MHDTF).

This technique has evolved from the Digital Tracking Filter (DTF), capable of only tracking the fundamental harmonic, that contains the same procedure as the widely electronics industry used Lock-In Amplifier [29]. The procedure, pictured in Figure 3.1, is carried out in three stages: dual-phase homodyning, followed by lowpass filtering and amplitude and phase extraction.

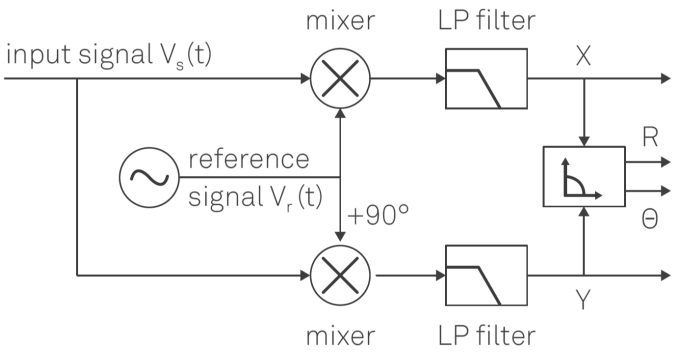

Figure 3.1: Sketch of a typical lock-in measurement[29].

It is convenient to explain the simpler procedure of the DTF, also interpreted in Musella et al. [1], before diving in the divergences and the details of the implementation of the MHDTF developed in this thesis.

The dual-phase homodyning is the first stage. Deriving from heterodyning, introduced in subsection 2.3.1, homodying is the mixing of two signals with same frequency content. In the particular application of amplitude and phase tracking of the DTF, the input signal would be the response of the system, which of course occurs at the excitation frequency. The reference signal is then a Constant

Output Level Amplitude (COLA) that has the same frequency as the excitation by design. Therefore, since the frequency of both signals, that is the input and reference signal, are identical, this technique is termed homodyning. It is then easy to observe how after the mixing, the obtained homodynes are a zero frequency signal (DC component) and a double excitation frequency signal.

As the title of this stage suggests, two homodyning mixing processes take place: the input signal is multiplied with the COLA reference signal and also with a 90° phase shifted COLA reference signal. Considering a signal at frequency ω, $resp\_signal(t) = A(t)\sin(\omega \times t + \phi(t))$, $A(t)$ and $\phi(t)$ are the amplitude and phase to track, respectively, and also the COLA reference signal $ref\_signal(t) = \sin(\omega \times t)$, the resultant homodynes, two per equation, yield:

$$resp\_signal(t) \times \sin(\omega \times t) = \frac{1}{2}A(t)\big(\cos(\phi(t)) - \cos(2\omega \times t + \phi(t))\big) \tag{3.1a}$$

$$resp\_signal(t) \times \sin(\omega \times t + 90°) = \frac{1}{2}A(t)\big(\sin(\phi(t)) + \sin(2\omega \times t + \phi(t))\big) \tag{3.1b}$$

The outcome of each mixing, or homodyning, can be separated into two new homodynes, that is, two new signal frequencies: a DC component, 0 Hz, and a 2ω component, with all the required tracking information easily obtained from the DC components.

Following is the lowpass filtering stage, aiming to attenuate all components above DC: the 2ω homodyne component and all other disturbances in the signal. The representation of these two stages and the consequent development of the input signal is best visualized by their Fourier transform:

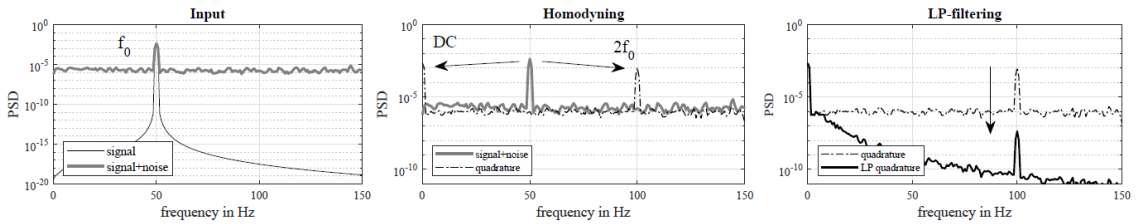

Figure 3.2: Two stages of a digital tracking filter applied on a 50 Hz sine tone signal [1].

After a successful filtering stage, only the DC homodynes remain. Increasing twofold these components, originated from Equation 3.1a and Equation 3.1b, equates the in-phase and quadrature components, respectively:

$$in - phase(t) = A(t)\cos(\phi(t)) \tag{3.2a}$$

$$quadrature(t) = A(t)\sin(\phi(t)) \tag{3.2b}$$

The amplitude and phase is obtained:

$$A(t) = \sqrt{(in - phase(t))^2 + (quadrature(t))^2} \tag{3.3}$$

$$\phi(t) = \arctan\left(\frac{quadrature(t)}{in-phase(t)}\right) \tag{3.4}$$

Starting from this procedure, extra stages and adaptations to the already established ones were implemented to meet some of the problems encountered due to the multi-harmonic content of the tracked nonlinear responses.

3.1 MHDTF Offline Implementation

The MHDTF procedure, with particular focus on offline processing, is summarized in Figure 3.3. In this section, each block of the diagram is introduced and explained. The MATLAB code of this procedure is present in section A.1.

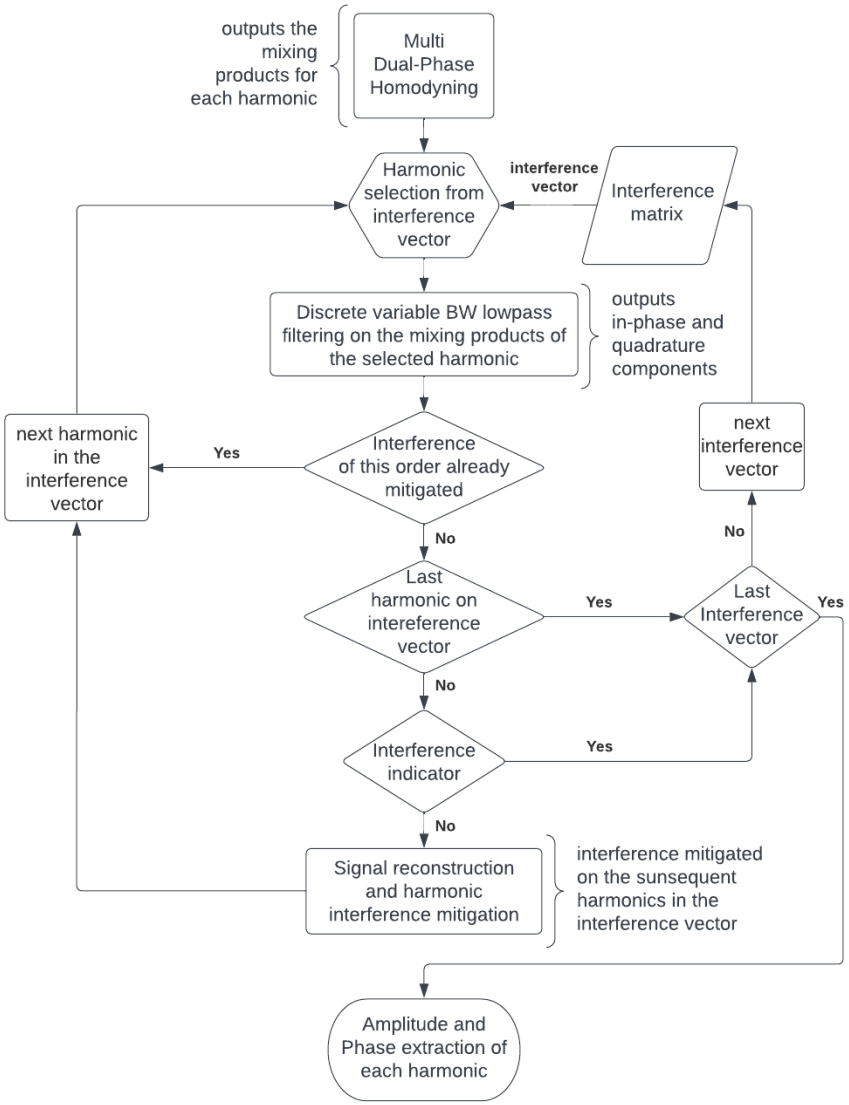

Figure 3.3: MHDTF procedure diagram.

3.1.1 Multi Dual-Phase Homodyning

The MHDTF procedure starts with the multi dual-phase homodyning. Since the response of a nonlinear structure is composed not only of the fundamental frequency but also of its harmonics, the homodyning mixing products differ from the single harmonic homodyning of Figure 3.1. For illustration, a multi-harmonic example signal, with two components, is defined: fundamental component at 10 Hz, with unit amplitude and null phase and a 2^{nd} harmonic component, trivially at 20 Hz, with half unit amplitude and null phase. The difference in amplitude permits to more easily distinguish the two components in the Fourier transform, not only of the signal itself, Figure 3.4, but also of the following Fourier transforms of the mixing products with this example signal.

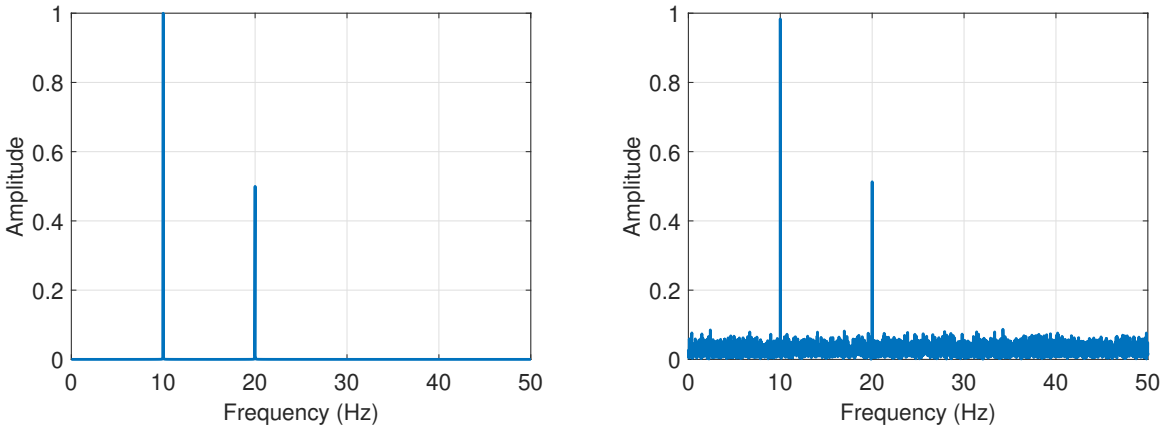

(a) without noise.

(b) with noise.

Figure 3.4: Fourier transform of the example multi-harmonic signal.

The mixing products of this signal with the reference signal, $ref\_signal(t) = \sin(\omega \times t)$, provide two homodynes at DC and 20 Hz, resultant of the mixing of the fundamental harmonic component, and two heterodynes at 10Hz and 30Hz, resultant of the mixing of the 2^{nd} harmonic component, as visualized in Figure 3.5. All these homodynes and heterodynes have an amplitude of half of the component in the signal that originated them. In the presence of noise in the signal, it may surprass this value. The mixing product of this multi-harmonic signal with the 90° phase shifted COLA reference signal is identical to the one pictured with the exception of a null component at 0 Hz.

In general, the mixing product of the multi-harmonic response signal with the reference signal, as well as the 90° phase shifted reference signal, will contain two homodynes, mathematically demonstrated in Equation 3.1, and as many pair of heterodynes as there are higher-order harmonics in the response signal.

The products of this dual-phase homodyning with the COLA reference signals at the fundamental frequency contain information regarding the 2^{nd} harmonic, at the heterodynes. However, it is more convenient to also perform a dual-phase homodyning targeted at the 2^{nd} harmonic-order, in an effort to bring the respective harmonic content to DC where it is more easily extracted after the lowpass filtering.

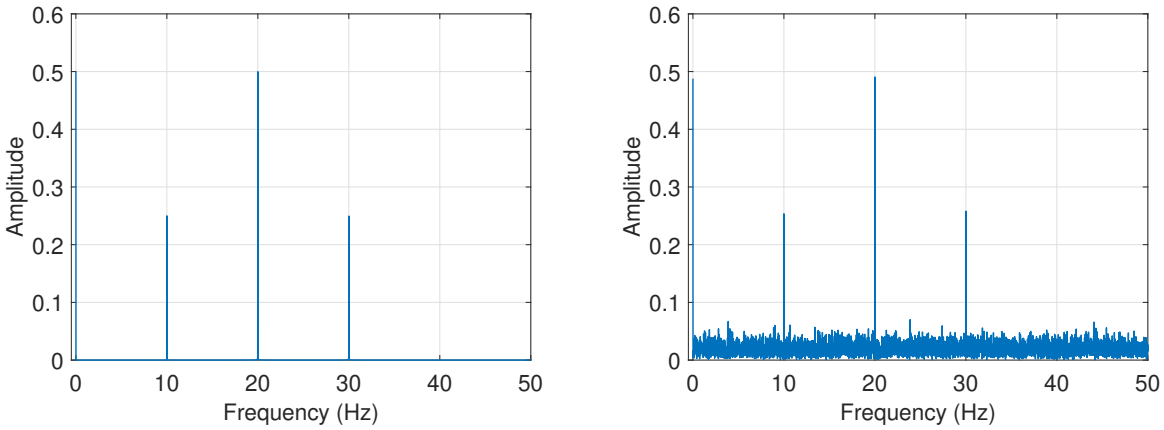

(a) without noise. (b) with noise.

Figure 3.5: Fourier transform of the mixing products of the multi-harmonic example signal and reference signal.

Mixing the example signal with a COLA reference signal at double the fundamental frequency, $ref\_signal(t) = \sin(2\omega_0 \times t)$, provides the Fourier transforms in Figure 3.6. As observed, there are two homodynes, DC and 40 Hz, and two heterodynes, 10 Hz and 30 Hz. The latter resultant of the mixing with the fundamental harmonic component of the example signal.

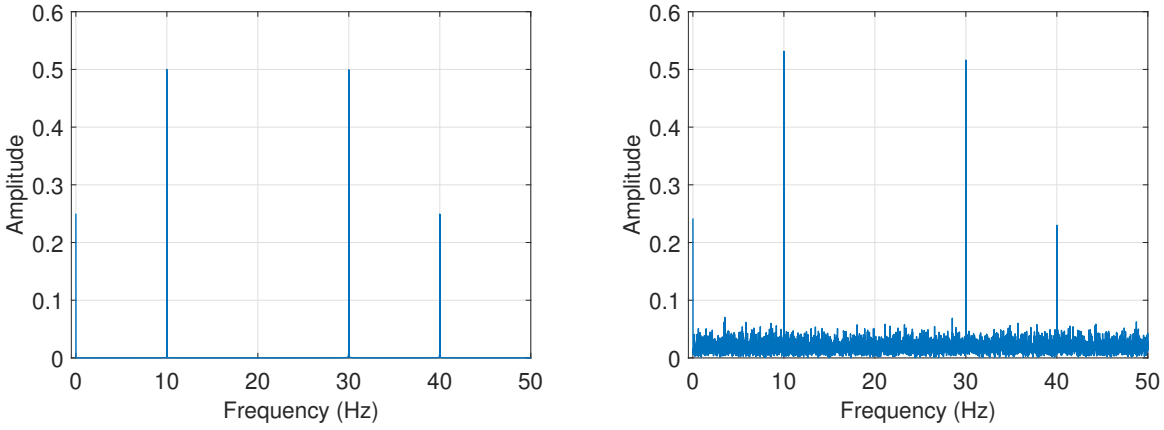

(a) without noise. (b) with noise.

Figure 3.6: Fourier transform of the mixing products of the multi-harmonic example signal and 2^{nd} order reference signal.

Ultimately, the multi dual-phase homodyning stage of the MHDTF procedure provides for a pair of mixing products per harmonic-order, with the content of the respective harmonic conveniently situated at 0 Hz, with other pairs of heterodynes respective to the other harmonic-orders also present. Of course, more heterodynes may appear due to noise or tonal disturbances in the signal, as observed in Figure 3.5 and Figure 3.6. This multitude of homodynes and heterodynes is very relevant as they may interfere with each other and disturb the amplitude and phase estimation.

3.1.2 Discrete Variable Bandwidth Lowpass Filtering

At this stage, ideally, all frequencies above DC are filtered out. Not only the $h_{order} \times 2\omega$ homodyne and other heterodynes stemming from the different harmonics but also noise and tonal disturbances present in experimental measurements.

Filter Parameters

The parameters of the employed lowpass filter influence the tracking accuracy and a practical analysis around these is required to ensure the best outcome. The most influential parameters are: design method, filter order and cut-off frequency.

The design method implemented in the development of the MHDTF is the Butterworth design. As suggested by All [30], the Butterworth design is versatile and it offers a smooth monotonic frequency response that is maximally flat in the passband. Figure 3.7 backs this claim when comparing to a regular IIR lowpass filter that has a higher passband ripple, less filtering capability in the vicinity of the cut-off frequency and the same transition band footprint at later frequencies.

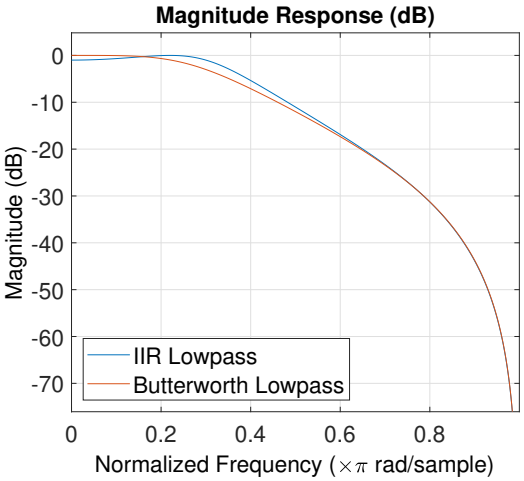

Figure 3.7: Magnitude response comparison between lowpass IIR and Butterworth filters, both with order 2.

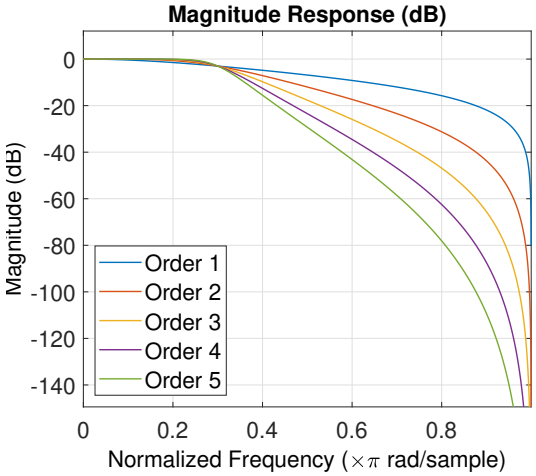

Figure 3.8: Magnitude response comparison between several lowpass Butterworth filters, order 1 to 5.

The filter order also plays a significant roll on the performance of the filter. Increasing the order of a filter improves unwanted components rejection, as the transition is steeper, Figure 3.8, at a cost of a slower response, as seen by the group delay per filter order in Figure 3.9.

In Figure 3.10 it is also possible to observe the rise in delay for the decrease in cut-off frequency, f_c. Again, another trade-off choice must be made as lower cut-off frequencies reject the unwanted homodyne, heterodynes and noise components more efficiently.

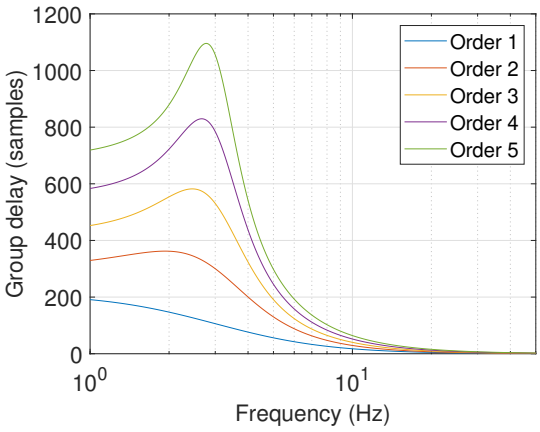

Figure 3.9: Group delay (in samples) of lowpass Butterworth per filter order, for the same normalized cut-off frequency.

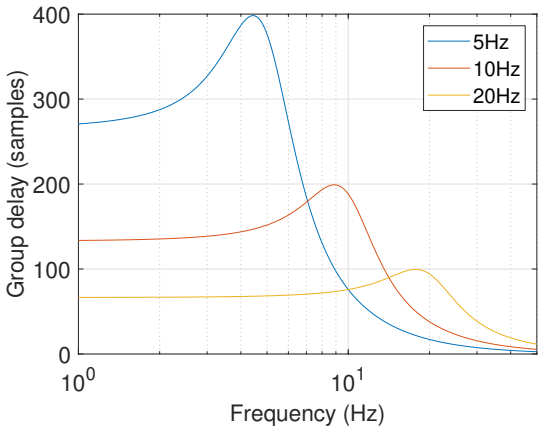

Figure 3.10: Group delay (in samples) of lowpass Butterworth per cut-off frequency, for the same filter order.

Since the filtering purpose is to attenuate all frequencies above DC, delineating the cut-off frequency evolves around this purpose. Previous studies on single harmonic DTF, carried out by Musella et al. [1] have shown that the cut-off frequency is optimal in the vicinity of 15% of the lowest signal frequency of the signal, f_0, for good response and noise rejection, $\frac{f_c}{f_0} \approx 0.15$.

For multi-harmonic purposes, the cut-off ratio should regard the lowest signal frequency of the respective harmonic, $\frac{f_c}{h_{order} f_0} \approx 0.15$. That is, when filtering the mixing products relative to the fundamental harmonic-order content of the example signal, the cut-off frequency should be $\approx$ 15% of 10 Hz. As for filtering the 2^{nd} harmonic-order content, the cut-off frequency should be $\approx$ 15% of 20 Hz. Additionally, with multi-harmonic content, cut-off ratios in the vicinity of the 15% value also accomplish the attenuation of heterodynes that may be present near to the DC component, when this DC component has a significant amplitude over the nearing heterodyne.

More importantly, for swept sine excitation, as the signal frequency increases, the constant passband bandwidth (BW) imposed by this cut-off ratio of the lowest signal frequency results in poor filter performance at higher frequencies, as visible in Figure 3.12. Therefore, a variable bandwidth filter should be employed to be assure tracking quality, with the cut-off frequency evolving at the same pace of the sweeping frequency, f, to which the notion of cut-off ratio is redefined as the ratio of the cut-off frequency and the sweeping frequency of the specific harmonic-order to track, $\frac{f_c}{h_{order} f} \approx 0.15$.

Discrete Varying Bandwidth Filtering

Althought there are already solutions to create varying bandwidth filters, such as in Moorer [31], with the use of Conformal Mapping, and pre-designed implementations in mainstream numerical and simulation software such as SIMULINK, the employed method is much more discrete and simple, aiming to use the MATLAB *filtfilt* function. The method consists of dividing the entire sample interval in N sub-intervals.

The cut-off frequency of each filter is then proportional to the sweeping frequency at the start of each sub-interval. All the other parameters are equal for all filters. For optimal results and computation efficiency, the number of sub-intervals N must be correlated to the excitation bandwidth since the decrease in performance at the end of the sub-interval occurs for bigger frequency differences between the start and end of the sub-interval.

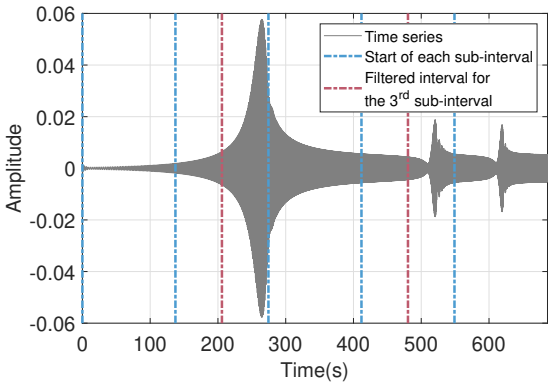

Figure 3.11: Response divided in 5 sub-intervals, $N = 5$, equally divided in samples/time. The red lines represent the wider interval for the 3^{rd} sub-interval.

Additionally, another relevant discrete varying filtering detail emanates from the delay and poor performance associated with the start and end of each filtering cycle, a wider sub-interval must be filtered and then the correct sample allocation must be done to the original sub-interval, as visualized in Figure 3.11.

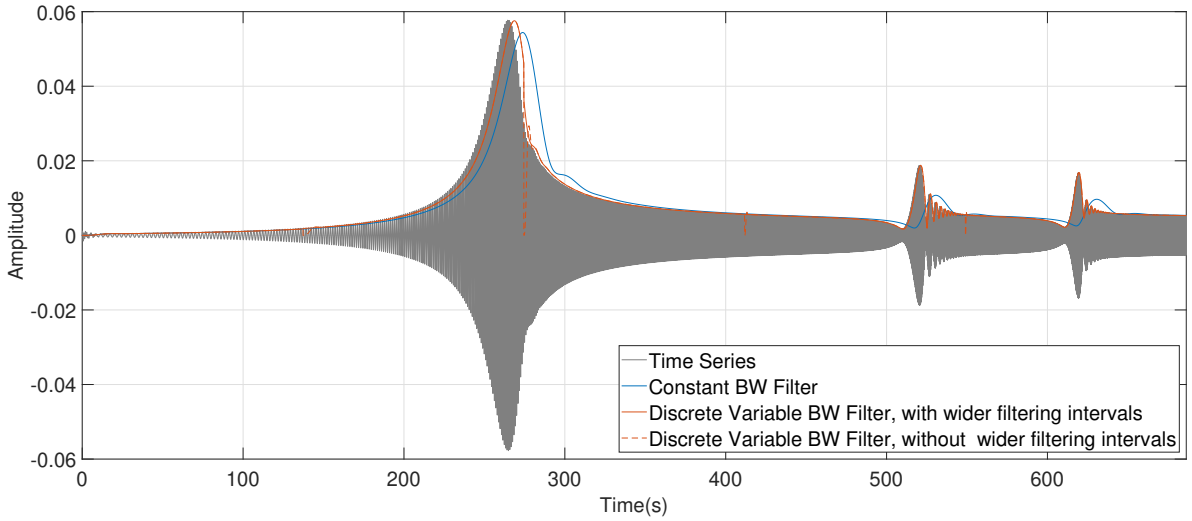

Figure 3.12: Amplitude tracking of a single harmonic logarithmic response signal, with constant or discrete variable bandwidth filtering. The use or not of wider filtering intervals is also pictured for the variable bandwidth filtering. $N = 5$, equally divided in time, and cut-off ratio = 15%.

Figure 3.12 displays the importance of a varying bandwidth lowpass filter for sweeping excitations. The performance decrease from the constant bandwidth and the improvements of the current method are clear, as well as the need for filtering wider intervals. The discrete variable filtering also accounts for smaller group delays at higher frequencies, since the cut-off frequency itself is higher, for the same cut-off ratio. This smaller group delay translates in two significant aspects at higher frequencies: the amplitude tracking delay to the signal itself is smaller as well as the filter delays at the start of each

interval, that is the difference between the red dashed (- -) and continuous (–) lines.

One more discrete varying filtering facet is the signal interval division: either equally divided in samples/time, as in Figure 3.11, or in frequency. Both options are identical when the sweep is linear. However, when the sweep is logarithmic, the time dividing option accounts for small frequency differences between the start of consecutive sub-intervals at the first sub-intervals and a large difference at the later sub-intervals, as interpreted from Table 3.1. This may result in poor filter performance at these later sub-intervals and, therefore, frequency dividing is advised.

Table 3.1: Frequency at sub-interval start for different interval division. Bandwidth of 10 to 110Hz, $N = 5$.

Interval Division	
Time/samples	*Frequency*
10 Hz	*10*
16.15 Hz	*30*
26.1	*50*
42.16	*70*
68.1	*90*

To obtain the sample location for each sub-interval, represented by $aux1$, for linear sweeps and for time divided intervals:

$$aux1(n) = 1 + n \times \frac{n\_samples}{N}, \qquad n = 0, 1, ..., N-1 \tag{3.5}$$

Where $n\_samples$ is the number of samples of the response signal. For logarithmic, frequency divided sub-intervals, where f_{start} and f_{end} represent the start and end frequencies of the excitation bandwidth:

$$aux1(n) = 1 + n\_samples \times \log_{\frac{f_{end}}{f_{start}}} \left(\frac{n}{N} \left(\frac{f_{end}}{f_{start}} - 1 \right) + 1 \right) \qquad n = 0, 1, ..., N-1 \tag{3.6}$$

After defining all the parameters for each filtering interval, the filtering process is executed with the MATLAB function *filtfilt*. This function has the convenience of performing zero phase filtering by processing the input data in both the forward and reverse directions. After filtering the data in the forward direction, the function reverses the filtered sequence and runs it back through the filter. Consequently, this function is only practicable for offline processing. The outcome has zero phase distortion, it removes the phase response associated with causal digital filters. As seen in Figure 3.13, the group delay is eliminated as the amplitude tracking clearly matches the envelope of the response signal.

This proved to be a major asset of the filtering stage, as the zero phase filtering results in the proper sample/time/frequency allocation of amplitude and phase. It also allows the use of higher filter orders and lower cut-off ratios thus improving the noise rejection and estimation, without the drawback of higher group delays. However, when the variations in response amplitude are extreme, resultant of dynamic phenonema such as beating, observed in the 2^{nd} and 3^{rd} modes of the response signal in Figure 3.13 [32], or signal perturbations from tonal disturbances, these changes in cut-off ratios are noticeable and therefore must remain changeable by the user of the MHDTF in order to obtain better results for that specific application.

The best trade-off for the current application is a 4^{th}-order filter with a cut-off ratio of 15% of the sweeping frequency. The latter can possibly be scaled downwards to 10% without major estimation drawbacks.

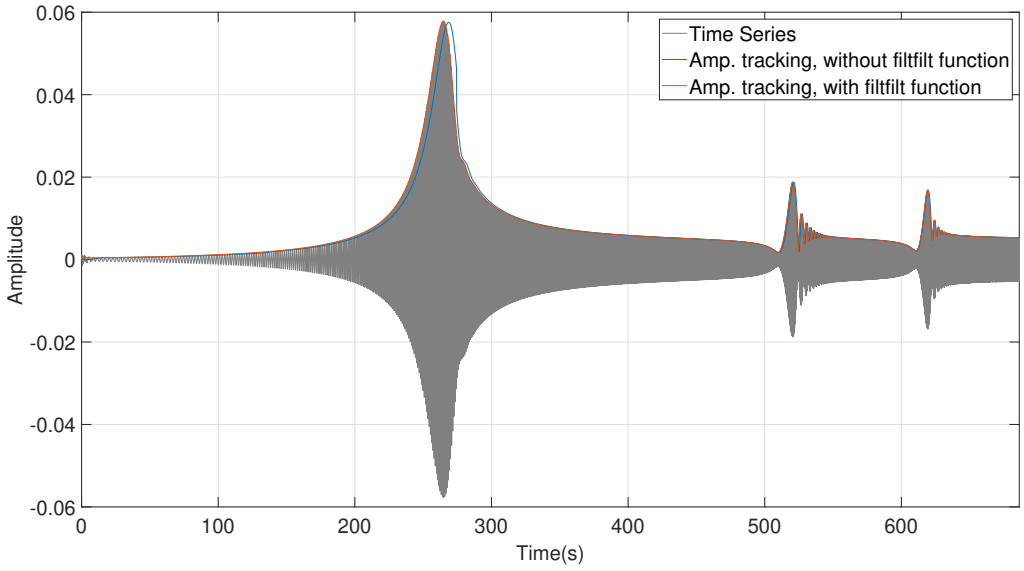

Figure 3.13: Amplitude tracking of a single harmonic response signal due to a logarithmic swept-sine excitation, with discrete variable bandwidth filtering. The use or not of the *filtfilt* function is portrayed. $N = 5$, equally divided in time, and cut-off ratio = 15%.

3.1.3 Harmonic Interference Mitigation

Harmonic interference mitigation is an extra stage of this procedure that rises solely from the multi-harmonic content of the nonlinear responses. The clearest way to demonstrate the need of this mitigation is to apply the described multi-harmonic identification procedure on a single harmonic signal. Theoretically, without interference, the higher-order harmonics content is expected to be irrelevant.

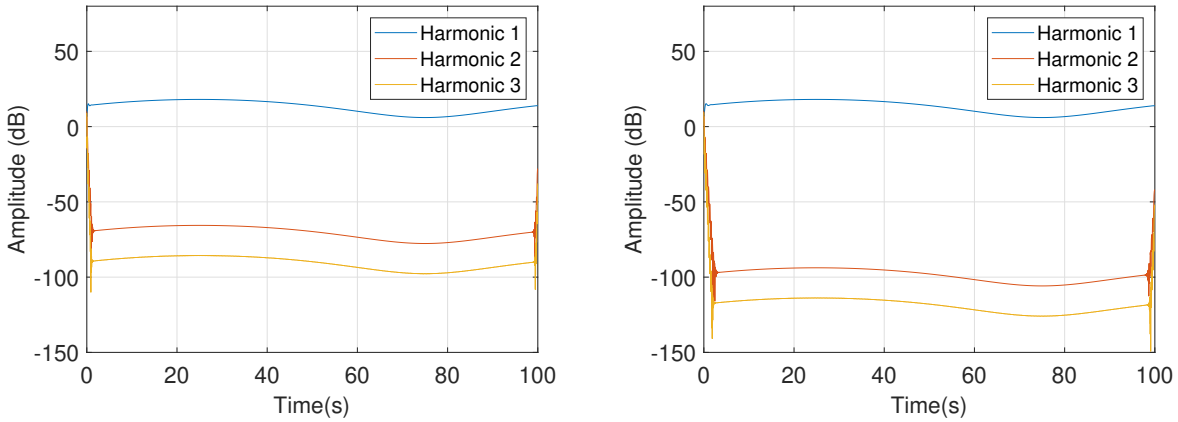

(a) cut-off ratio = 15%

(b) cut-off ratio = 10%

Figure 3.14: Amplitude tracking of the 1^{st}, 2^{nd} and 3^{rd} harmonic-orders of single harmonic sine signal with varying amplitude.

Instead, Figure 3.14 shows that the tracking of the 2^{nd} and 3^{rd} order harmonics is not null. This is due to the influence of the 1^{st} harmonic heterodyne on the mixing products of the 2^{nd} and 3^{rd} order, as the similar shape of the curves might suggest. Additionally, decreasing the cut-off ratio reduces the influence

of the 1^{st} harmonic on the 2^{nd} and 3^{rd} orders, as expected. It also makes sense that the influence on the 2^{nd} order is greater than the 3^{rd} order, plainly because the first order heterodyne is further away from DC for the 3^{rd} order homodyning products than for the 2^{nd} order products.

Decreasing the amplitude of the fundamental harmonic, which is the interfering harmonic in this situation, also decreases the interference curves by the same amount, which is an indicator of the primary influence of the difference between the higher and lower amplitude harmonics.

If the amplitude content of the 2^{nd} and 3^{rd} harmonic-orders in the signal are substantially higher than the interference levels of Figure 3.14 there is no concern of harmonic interference. On the contrary, if it is substantially lower, only interference is tracked and the same results of Figure 3.14 are obtained.

Concluding, harmonic interference arises from all the heterodyne products resultant of the multi dual-homodyning stage. All orders interfere with each other, it is only when the amplitude difference between these orders is large enough to interfere with the amplitude and phase estimation that there is a need to mitigate this phenomena.

Since in experimental data there is an inherent noise intrusion in the measured response signals, interference mitigation is not required as the interference levels are situated well below the noise levels. However, for simulated data, the demand is clear.

Mitigation Procedure

The current method for the harmonic interference mitigation is to recreate the interfering order signal as described further ahead in subsection 3.3.1, and then subtract the heterodyne products of this recreated single harmonic signal with the different order reference signals to the mixing products of the initial dual-phase homodyning stage. Ultimately, this is identical as eliminating the interfering component from the response signal and then perform the dual-phase homodyning of the interfered orders, but much more compact.

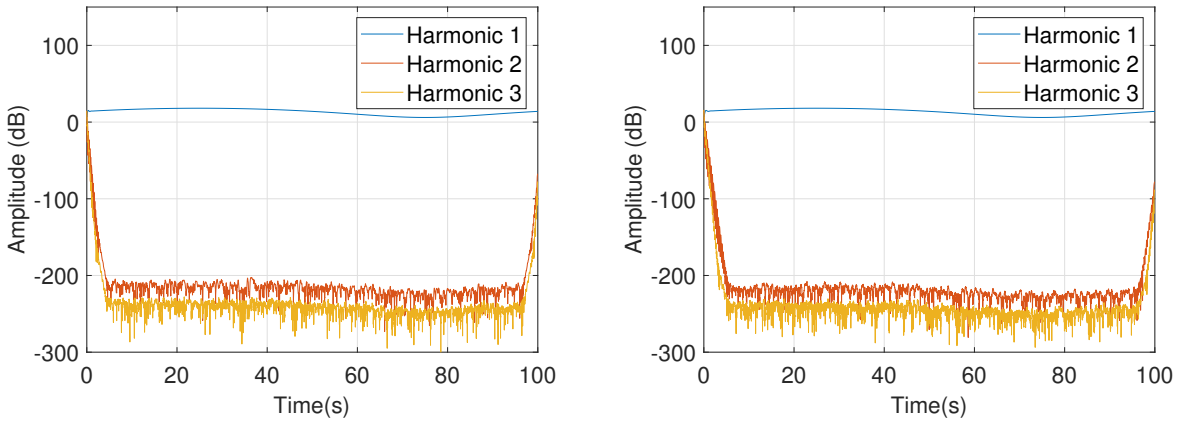

(a) cut-off ratio = 15%

(b) cut-off ratio = 10%

Figure 3.15: Amplitude tracking of the 1^{st}, 2^{nd} and 3^{rd} harmonic-orders of single harmonic sine signal with varying amplitude. Harmonic interference mitigation was applied.

Figure 3.15 shows the results of this interference mitigation method. The mitigation is not fully achieved since the recreated single harmonic signal is only an approximation of the single harmonic signal itself. However, it does allow to lower the interference level and the resultant amplitude estimation of the higher-orders that reside below this cap are clear to the user as erroneous. In contrast to the previous amplitude estimation that could induce the user in error. From Figure 3.15, it is also possible to infer that for different cut-off ratios, the result after mitigation is sensitively the same.

For swept-sine applications of the MHDTF, when $N > 1$, an interference indicator function was created to verify if the amplitude tracking of a certain harmonic-order is composed or not of interference. This function operates by verifying the initial and previous sample of a filtering interval and assessing the difference in amplitude between these two points. If this difference is bigger than a stipulated amount, an amplitude leap occurs. Examples of amplitude leaps are visible below, at 20, 30 and 40 Hz for the 2^{nd} and 3^{rd} harmonic-orders:

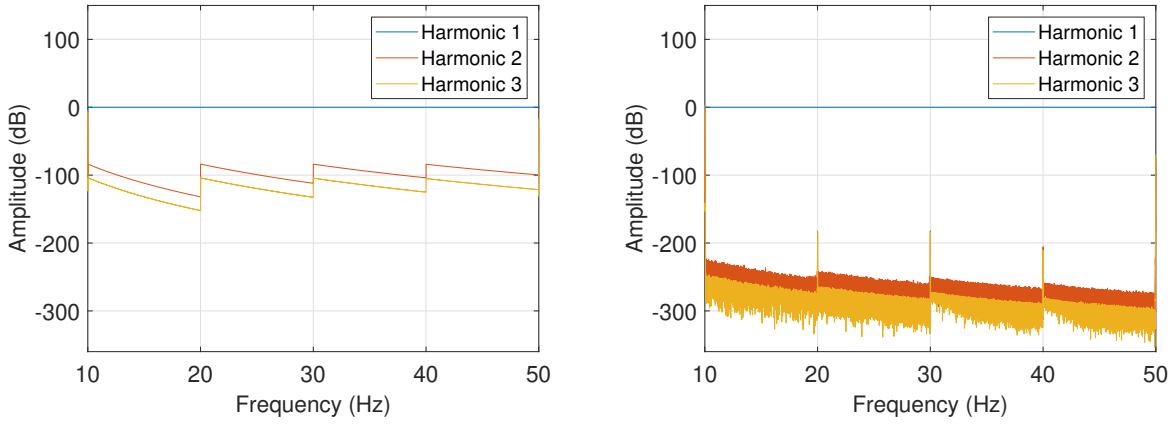

(a) without interference mitigation

(b) with interference mitigation

Figure 3.16: Amplitude tracking of a single harmonic logarithmic signal, 10 to 50 Hz. Amplitude leaps are visible due to harmonic interference. N = 4, equally divided in frequency, and cut-off ratio = 15%.

This amplitude leap occurs due to the different cut-off frequencies of each interval. As the cut-off frequency increases for the next interval, it instantly rejects less the interfering heterodyne, which causes the sudden increase in amplitude. This method has proven sufficient enough in the assessment of harmonic interference and remains tunable by the user according to the obtained results.

There are two settings that adjust this interference indicator, whose MATLAB can be found in section A.2: $leap\_detection$ is the amplitude difference limit before it is considered a leap and $leap\_percentage$ is the percentage limit of leaps allowed, in relation to the amount of leaps possible, i.e. $N - 1$, before the harmonic is appraised as composed by interference or not. The demand for this $leap\_percentage$ comes from the big difference in amplitude that some harmonics may have, in their lowest value they may reach the limit of the interference mitigation and present leaps resultant of the mitigation procedure, as the ones visible for DOF3 in Figure 4.7.

To tie the interference indicator in a procedure that evaluates and mitigates interference, the information

of what harmonic interferes with the others is required. This information is stored in the interference vector. For illustration, a vector as [1 2 3] delineates that the 1^{st} harmonic, the fundamental harmonic, interferes with the 2^{nd} and the 3^{rd}. Additionally, the 2^{nd} harmonic interferes with the 3^{rd}. The mitigation procedure follows this same order. The interference of harmonic 1 is mitigated on harmonics 2 and 3 and the interference of harmonic 2 is mitigated on harmonic 3.

The interference matrix is then composed of several interference vectors, resultant of the permutation of the several harmonic-orders, with the fundamental order always being the first order of each vector. For example, when tracking the 1^{st}, 2^{nd} and 3^{rd} harmonics, the interference matrix is:

$$interference\_matrix = \begin{bmatrix} 1 & 3 & 2 \\ 1 & 2 & 3 \end{bmatrix} \tag{3.7}$$

From this, the mitigation procedure on Figure 3.3 focuses on rejecting the interference vectors that have the wrong interference order and tries to find the most appropriate vector. It's also important to reassure in this procedure that the interference that one harmonic causes on the others is only mitigated once.

After the filtering and harmonic interference mitigation stages, there is one in-phase and quadrature component for each harmonic-order, from which the amplitude and phase is obtained according to Equation 3.2a - Equation 3.2b.

3.2 MHDTF Online Implementation

The knowledge obtained from multi-harmonic estimations can have diverse applications. One of them resides in the Control field. In the end, that is the application of the single-harmonic DTF and harmonic estimator developments in Musella et al. [1] and also of other state of the art methods such as the adaptive filter in Abeloos et al. [33]. Consequently, it is also of the interest of the author to briefly expand the methodology constructed in section 3.1, for offline processing, to online processing.

The adopted procedure, developed in the SIMULINK software, is reduced to essentials. The harmonic interference mitigation stage is neglected and the lowpass filtering simplified, largely due to the existence of a Butterworth variable bandwidth lowpass filter block. As a result, since the processing is online, the filters must be causal and the group delay associated is inevitable.

In Appendix B. is displayed the block diagrams relative to the online methodology as well as a brief explanation of its implementation.

3.3 Additional Computations

The following computations and estimations are capable due to the MHDTF outcomes. It is important to briefly explain the implementation of these computations as they not only portray the estimations of MHDTF in different techniques but are also required in the interference mitigation procedure such as the

signal recreation computation.

3.3.1 Signal Recreation

It is important to remark that the in-phase and quadrature components of all harmonic-orders correspond to instantaneous Fourier coefficients, in similar fashion to what is mentioned in section 2.2. With these coefficients, it is possible, by definition, to attempt to recreate the original response signal. This is even extra convenient in the MHDTF procedure since the already created COLA reference signals are the necessary pair for the coefficients.

A specific single harmonic signal is calculated with multiplication of the respective harmonic-order instantaneous Fourier coefficients and COLA reference signals, as demonstrated in Equation 3.8a. Summing all n_h these single-harmonic signals provides the multi-harmonic response signal, Equation 3.8b.

$$response_h(t) = in-phase_h(t) \times \sin(h \times \omega_0 \times t) + quadrature_h(t) \times \sin(h \times \omega_0 \times t + 90°) \tag{3.8a}$$

$$response(t) = \sum_{h=1}^{n_h} response_h(t) \tag{3.8b}$$

3.3.2 Harmonic Sum

The harmonic sum is the combined amplitude of all harmonics. Consequently, it is also the amplitude envelope of the recreated multi-harmonic signal. To calculate this pretended amplitude, at each sample, a single fundamental period sinusoidal wave is created for each harmonic-order, with the respective amplitude and phase values. The maximum value of the sum of all sinusoidal waves, for this single period, is regarded as the harmonic sum for that sample point. As visualized in Figure 3.17.

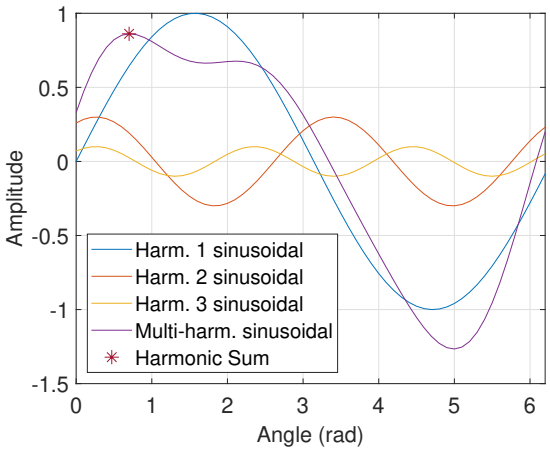

Figure 3.17: Illustration of the computation of the harmonic sum for a single sample point.

The MATLAB code of this computation is present in section A.3.

3.3.3 Nonlinear Frequency Response Curve

At this stage, it is important to better explain the concept of Nonlinear Frequency Response Curve (NLFRC) and how it is approached in this dissertation: the NLFRC of a certain harmonic-order relates the behaviour of this order to the input force that originated it, more particularly to this thesis, to the tracking of the 1^{st} harmonic of the aforementioned force.

The NLFRC, obtained using the $H1$ estimator is calculated according to the mathematical expressions detailed in section 2.1.1. Each harmonic-order has its own set of NLFRCs, with the input of the H_1 always being the harmonic 1 estimation of the input forces and the output is the response estimation of the relative harmonic-order.

The MATLAB code of the H_1 algorithm is present in section A.4.

3.4 Limitations and Improvements

The MHDTF accuracy finds its limitations from the procedure itself and also from input signal characteristics. Internal to this procedure, these limitations may rise from the techniques and filter performance and also from improper defined settings. Because of the latter, it is paramount for the MHDTF to remain tunable by the user.

The harmonic interference governs the capability and accuracy of the relative lower amplitude harmonics tracking. Additionally, since the harmonics to track are selected by the user, stored in the harmonic selection vector, if the interfering harmonic is not being tracked, it is not possible to mitigate its interference. Furthermore, from Figure 3.15 and Figure 3.16, the limit of the harmonic interference mitigation method is exposed at around 200 dB amplitude difference to the interfering harmonic.

Adding to the importance of correctly defined settings is the proper selection of the interference indicator parameters. There may be examples, like harmonic 3, DOF3, in Figure 4.7, where the appearance of leaps at the lower amplitudes of the tracked harmonic, due to the mitigation method, may induce the interference indicator in a wrong evaluation. Increasing the $leap\_percentage$ is advised in these cases.

The MHDTF performance is also dependent on the number of intervals N. Higher the N, the less discrete the filtering process and the better the performance. However, this comes at the cost of extremely increased CPU time due to the wider filtering intervals. The use of a variable bandwidth lowpass filter would erase this trade-off, however it must be paired with a different interference indicator.

External to the MHDTF, certain characteristics of the input signal may induce difficulties in its tracking. First, complying with Nyquist–Shannon sampling theorem is of extreme relevance in the application of the MHDTF since, due to the system nonlinearity, the response also occurs for the harmonics of the excitation frequency. If it's desired to track the h^{th} harmonic response, it is required to assure the conformance of the sampling frequency in regards to this h^{th} harmonic frequency, $f_s > 2 \times h \times f_{max}$, where f_{max} is assumed to be the maximum value of the excitation bandwidth. From the experience of

the author of processing undersampled and borderline undersampled signals, f_s must be conservatively 20% higher than what is proposed in the Nyquist–Shannon sampling theorem.

Jumps between several solution branches, a unique phenomenon of nonlinear systems, and beating phenomena, as entailed in [32], cause sudden variations in the measured signal. In these situations, the tracking accuracy decreases, the MHDTF cannot react quickly enough. The influence of the cut-off ratio will be studied further ahead for these situations. Nevertheless, beating phenomenon can be avoided with lower sweep rates.

The presence of signal disturbances in the signal also affects the estimations. Different categories can be used to differentiate noise. Electrical noise from the circuit that turns measured accelerations into a voltage signal causes some tonal disturbances at the alternate current frequency. In experimental testing, this was identified at a frequency of 50 Hz. In some sensors, short circuits can also happen, resulting in the capture of an incorrect signal. It is necessary to eliminate the measurements of these sensors from the analysis. Mechanical noise can come from a variety of sources, such as vibrational noise from the surroundings or noise from thermomechanical sources, inducing a constant white noise in the measurements. The influence of the cut-off ratio on signal disturbances will also be studied further ahead in this document.

At last, the time-frequency evolution of the signal is not flawlessly clear. The discrepancies from the input signal frequency and its numerical assumption, used in the COLA reference signals and consequently in the reconstructed signal, may limit the estimation.

Chapter 4

Application on Simulation Data

Simulation data are very helpful in the development stage of any technique, since the perturbance free signal ensures that any estimation mistake stems from the method, assuring its validation before processing experimental data. A lumped parameter system and its mathematical model are defined, granting the calculation of simulation data, through a Newmark solver, expressed in acceleration and displacement time series.

In this chapter, these resultant responses act as input of the Multi-Harmonic Digital Tracking Filter (MHDTF). The results will be analysed as well as the influence that some parameters have. The same signals will also be processed with the adaptive filter and the consequent results compared with the MHDTF. The mathematical model of the system, translated into the equation of motion is also solved by the Harmonic Balance (HB) method. Contrasting this solution with the MHDTF results is paramount on the validation of the proposed procedure.

4.1 Simulated Lumped Parameter System

In this chapter, the simulation data refers to a 3 DOF lumped parameter system, Figure 4.1, consisting of 3 masses and 4 springs and dampers. Between the 1^{st} mass and the ground there is a cubic spring, which is the source of nonlinearity in the system.

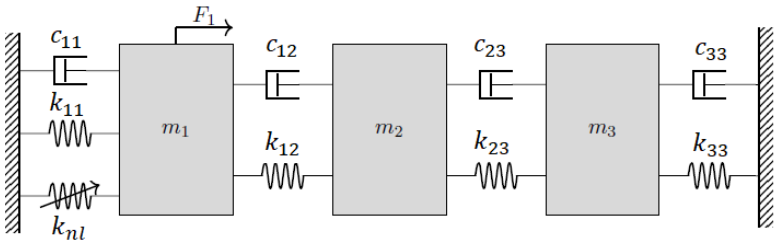

Figure 4.1: 3 DOF system. Cubic spring at the 1^{st} mass is the source of nonlinearity.

The structural parameters of the employed system are depicted in Table 4.1.

Table 4.1: 3-DOFs system 1 parameters.

Mass(Kg)	Stiffness (N/m)	Nonlinear cubic stiffness (N/m^3)	Damping (Ns/m)
$m_1 = 10$	$k_{11} = 1$	$k_{nl} = 1$	$c_{11} = 0.3$
$m_2 = 1$	$k_{12} = 3$		$c_{12} = 0.01$
$m_3 = 1$	$k_{23} = 1$		$c_{23} = 0.01$
	$k_{33} = 1$		$c_{33} = 0.01$

From the structural parameters, disregarding the nonlinear cubic spring, the natural damped frequencies can be analytically calculated: 0.36 rad/s, 1.29 rad/s and 2.15 rad/s.

In order to obtain the time series of the response of the system, a 0.05N constant amplitude logarithmic swept-sine input force, bandwidth of 0.1rad/s to 3 rad/s, was applied at the 1^{st} mass. From there, a Newmark solver constructed the following displacement and acceleration response signals processed in this chapter.

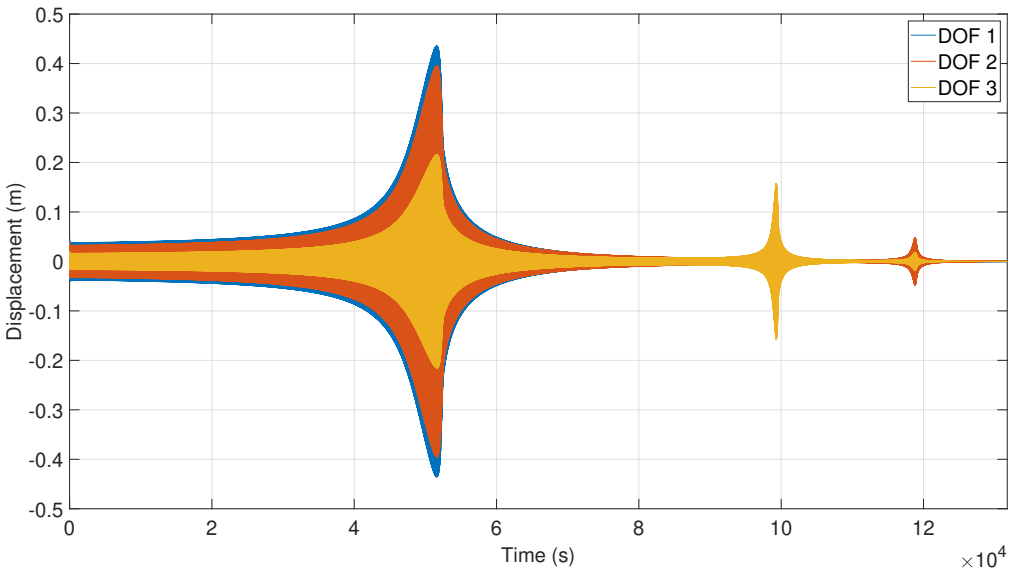

Figure 4.2: Simulation displacement signals.

Figure 4.2 and Figure 4.3 are the displacement and acceleration response time series, respectively. At first sight, in the 1^{st} mode, nonlinear phenomena is visible, particularly, jump phenomenon. The sudden transition in amplitude and the non-symmetry, around the resonance frequency, are visible for both responses due to the hardening nonlinearity. Therefore, a significant higher harmonic-order amplitude is expected at the first mode. The other two modes, however, do not resemble any of the just mentioned nonlinear effects and can be approximated as linear. The higher harmonic-orders should have insignificant contributions in the response. The goal of the MHDTF is to quantify this and identify exactly their amplitude and phase.

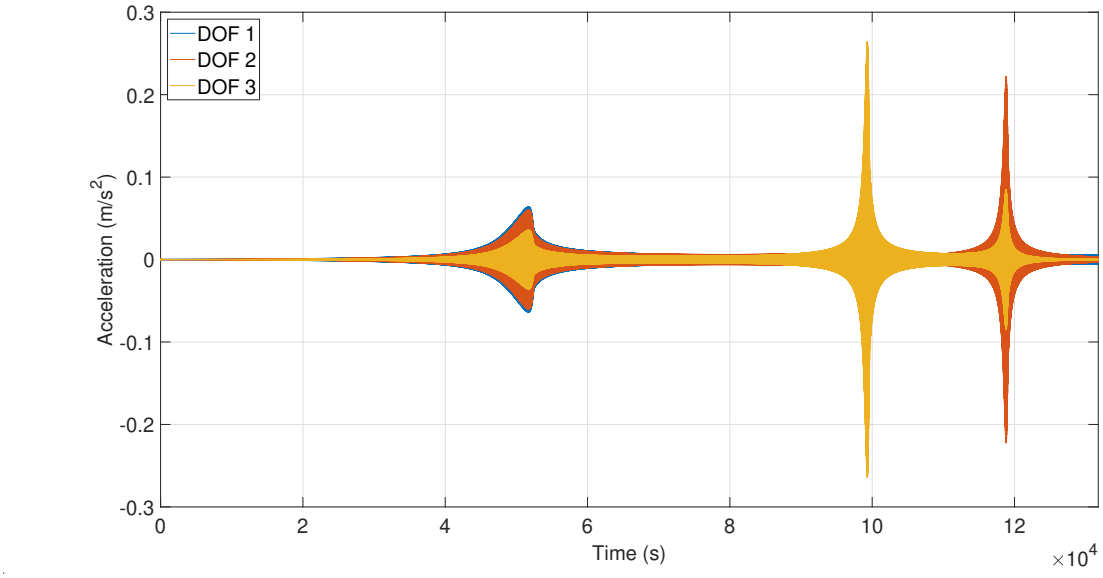

Figure 4.3: Simulation acceleration signals.

4.2 MHDTF Application

The MHDTF procedure is applied on the acceleration response signal of Figure 4.3. The number of sub-intervals N is equal to 10 and the cut-off ratio is 15%. The interference indicator parameters, $leap\_percentage$ and $leap\_detection$, were set at 30% and 5dB, respectively. These parameters can be considered as universal for unprecedented data processing.

The first result to analyse is the amplitude estimation. In Figure 4.4, Figure 4.5 and Figure 4.6, the envelopes of the estimated amplitude are contrasted with the time series of the acceleration. By virtue of the cubic nonlinearity, harmonics 1 and 3 are the most significant, hence only the ones being tracked.

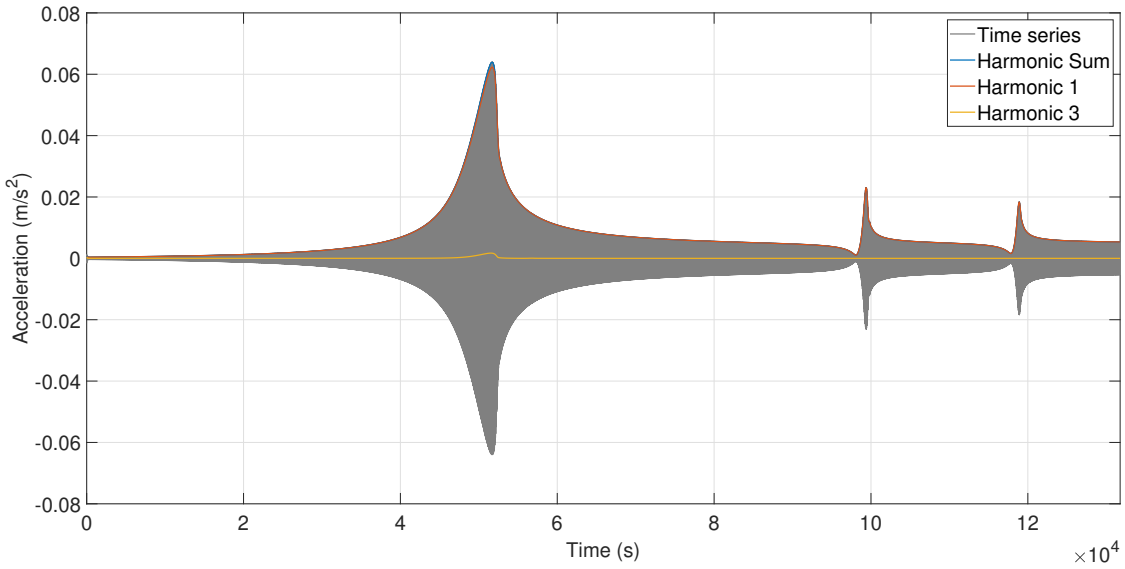

Figure 4.4: DOF1 acceleration signal and respective MHDTF tracking.

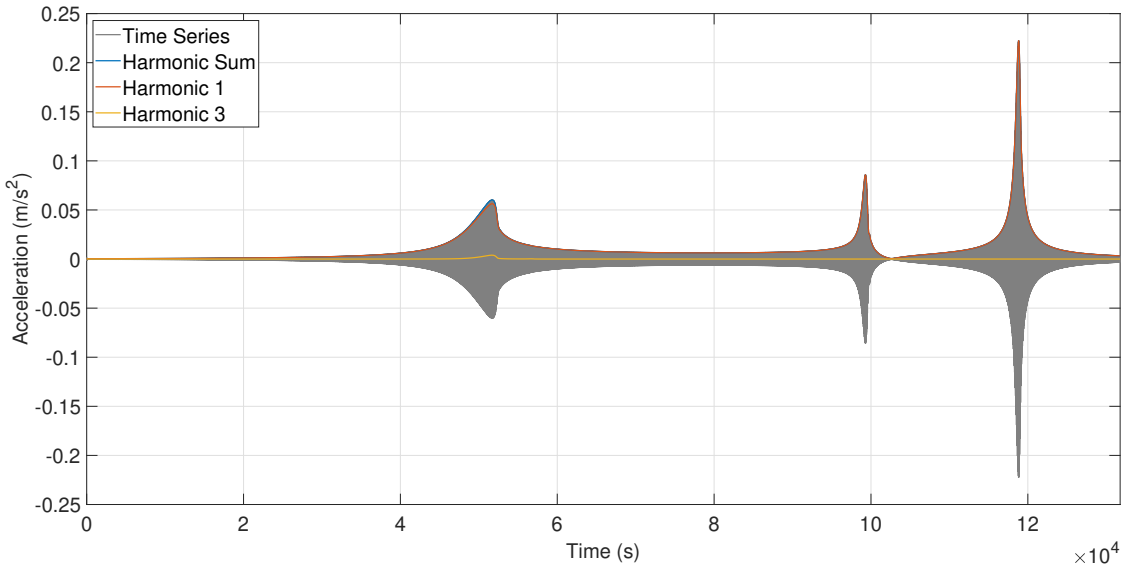

Figure 4.5: DOF2 acceleration signal and respective MHDTF tracking.

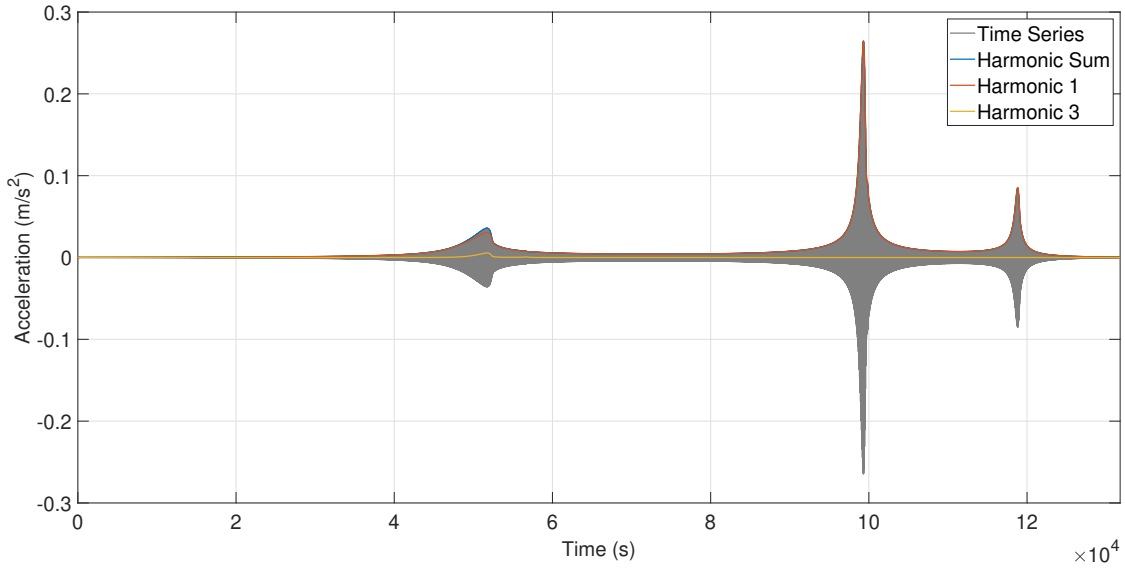

Figure 4.6: DOF3 acceleration signal and respective MHDTF tracking.

Visualizing the amplitude envelopes, that is, the harmonic 1 and 3 tracked amplitudes and their sum, the assumptions made in section 4.1 appear to be correct. In all DOFs, the influence of harmonic 3 can not be neglected for the first mode, the harmonic sum better approximates the time series amplitude and the identification error that is committed in identifying the fundamental harmonic only is hence very clear. For the remaining orders, at this scale, they are irrelevant in the overall response, the harmonic sum and harmonic 1 amplitudes match and approximate the time series evenly.

The structural Nonlinear Frequency Response Curve (NLFRC) also provides great insight of the nonlinear effects on the response. The amplitude of the NLFRC, expressed in dB, and the absolute phase, in degrees, of all DOFs of the described system are portrayed, for the 1^{st} and 3^{rd} harmonic-orders in Figure 4.7.

Once again, strong nonlinearity at the 1^{st} mode is verified as well as the constant decay of the nonlinear

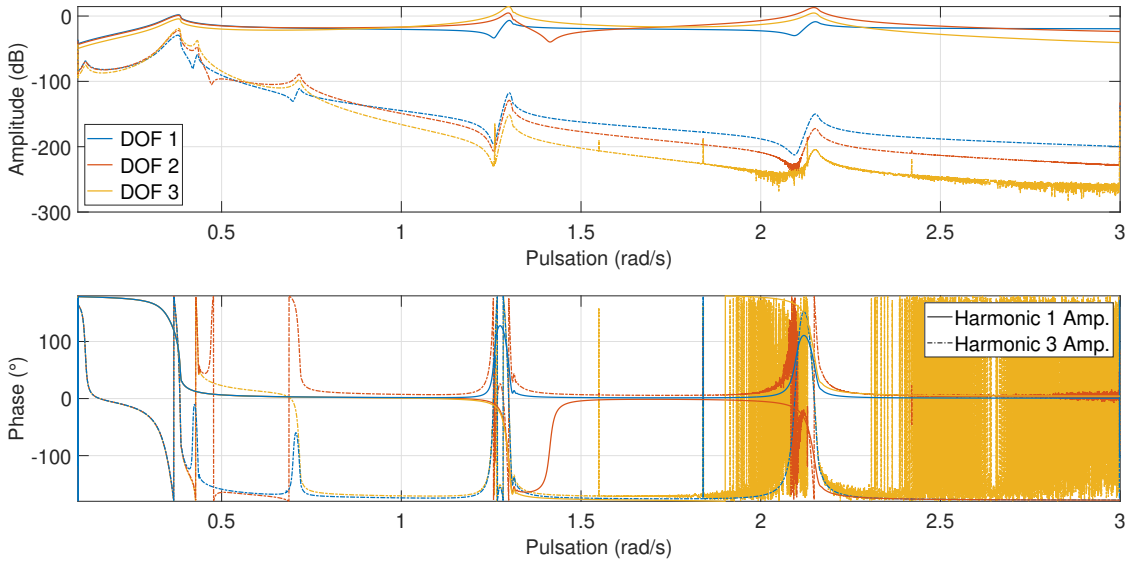

Figure 4.7: Acceleration NLFRC estimation of all 3 DOFs.

effects at higher frequencies, hence the imperceptible contribution of harmonic 3 in Figure 4.4, Figure 4.5 and Figure 4.6 on the 2^{nd} and 3^{rd} modes.

Moreover, due to the shift of the $x - axis$ from time to frequency, the resonance frequencies can be identified. The frequency of the 1^{st} fundamental mode is approximately 0.39 rad/s, while the natural damped frequency of the underlying linear system ($k_{nl} = 0$) is 0.36 rad/s. This increase in resonance frequency due to the hardening nonlinearity is not remarkable in the other modes.

In harmonic 3, superharmonic resonance also occurs. For all DOFs, in the amplitude of this order are 6 peaks: 3 corresponding to the resonance peaks, at the same frequency of the peaks in the fundamental harmonic, and 3 superharmonic resonance peaks. The latter occur at $1/3$ of the resonance frequency, that is, the 1^{st} superharmonic takes place at $0.39/3 = 0.13$ rad/s, the 2^{nd} at $1.29/3 = 0.43$ rad/s and the 3^{rd} at $2.15/3 = 0.72$ rad/s. Once again, another particular nonlinear phenomenon identified!

The amplitude and phase estimations are very clear up until the -230 dB amplitude level where the tracking of harmonic 3 is clearly corroded. This can be due to the tolerance error used in the Newmark simulation and in general the difference between 1^{st} and 3^{rd} harmonic-order amplitude, underlining the possible limitations of the harmonic interference mitigation. Furthermore, there is no interest in estimating such a low response contribution, also because in experimental measurements the signal-to-noise ratio is expected to be lower than 200 dB. In the NLFRC of DOF 3, in harmonic 3, there is also some unwanted traces of amplitude leaps, resultant of the harmonic interference mitigation procedure.

The construction of the NLFRCs for the same data without the harmonic interference mitigation and posterior contrast with Figure 4.7 demonstrates the importance of this step on simulation data. Portrayed in Figure 4.8, up until the amplitude level of -120 dB, the estimations are clear. The amplitude range of -120dB to -150dB signals the extremely oscillatory in amplitude transition from harmonic 3 content to harmonic 1 interference content, mimicking the harmonic 1 amplitude combined with amplitude leaps,

from the frequency of 1 rad/s forward.

The CPU time of performing harmonic mitigation increased 17 %, referenced to not performing this procedure. This may increase rampantly with the inclusion of higher-orders, due to the permutation operation that calculates the interference matrix.

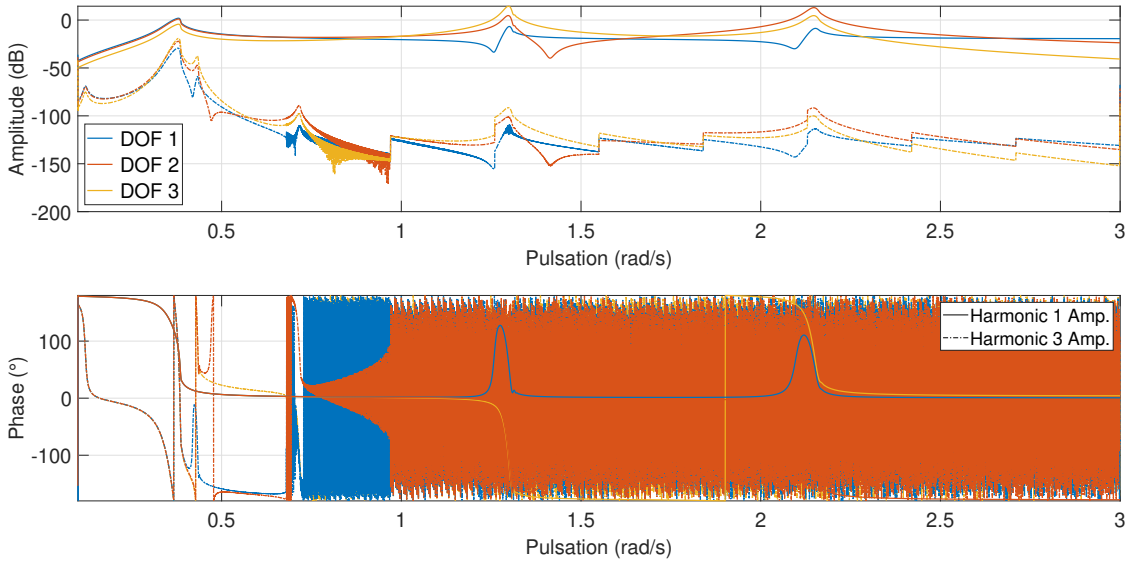

Figure 4.8: Acceleration NLFRC estimation of all 3 DOFs, without harmonic interference mitigation.

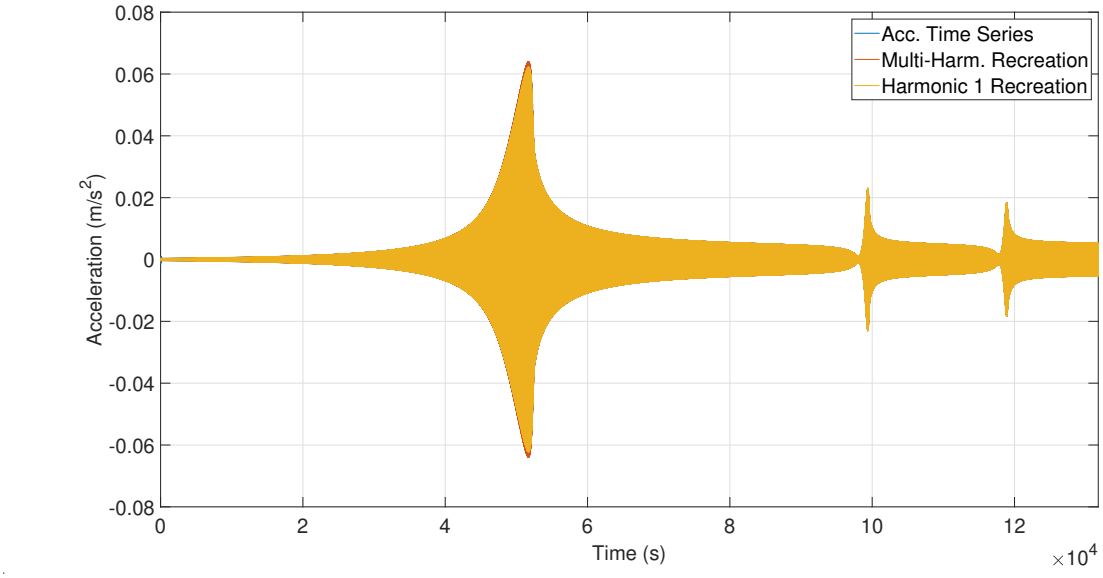

Figure 4.9: DOF1 acceleration signal and respective multi-harmonic and 1^{st} order single-harmonic signal recreation.

Another possible outcome of the MHDTF is the reconstruction of the tracked signal. In Figure 4.9, two recreated signals are contrasted with the tracked response signal, for DOF1. The multi-harmonic signal

was constructed with the sum of reconstructed signals from harmonic 1 and 3, as entailed in subsection 3.3.1, inherently, its envelope is the multi-harmonic sum of Figure 4.4. The other reconstructed signal is solely composed of the reconstructed harmonic 1 signal, and its envelope matches the tracking of harmonic 1 in Figure 4.4.

The multi-harmonic reconstruction matches faithfully the tracked time series and its distinction is not visually possible, however, the comparison with the harmonic-order 1 reconstruction is another indication of the identification error that is committed in identifying the fundamental harmonic only.

Due to the lack of disturbances in the signal, the mathematical difference of this recreated signal and the tracked signal appoints to the errors committed on the estimation. Of course, associated with this error are some of the already described limitations of the MHDTF procedure and the analysed signal: discrepancies from the input signal frequency and its numerical assumption, however in simulation data this discrepancy should be very minimal, or null; harmonic interference mitigation limitations; significant variations in the signal, although, from Figure 4.3, there is not any trace of this phenomena in the tracked signals.

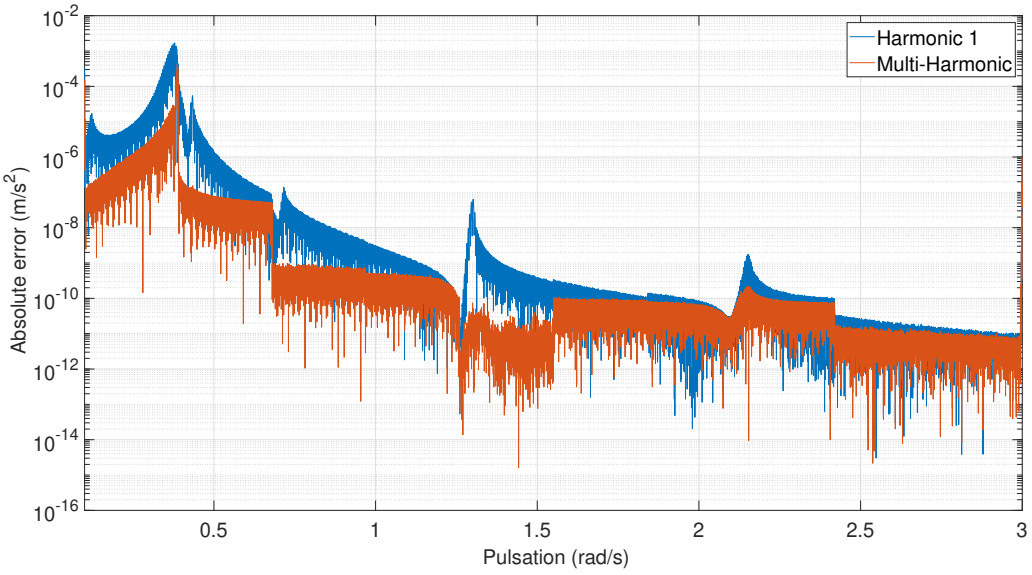

Figure 4.10: Multi-harmonic and 1^{st} order single-harmonic estimation error, for DOF1.

Nevertheless, the difference between estimation errors extends great insight as to the importance of multi-harmonic identification as well as the influence of the parameters of the proposed procedure, as investigated in subsection 4.2.1. The identification error of only estimating the fundamental harmonic is portrayed in Figure 4.10, as well as the error of multi-harmonic identification. As expected, the error difference of including harmonic 3 in the estimation is as greater as the significance of harmonic 3, that is, in the first mode.

In general, the estimation error is consistently greater in the vicinity of the 1^{st} resonance and decays with the sweeping frequency. The nonlinear effects appear to heavily influence the error and may appoint to

the necessity of including higher-order harmonic or even sub-harmonics in the estimation.

4.2.1 MHDTF Parameter Influence

The MHDTF has the advantage of being fundamentally tuned by the user according to their results and needs. In this context, it is important to investigate the impact of different parameters, namely the number of sub-intervals N and the cut-off ratio. In principle, both of these parameters influence the filtering stage in the same way, that is, the cut-off frequency f_c relation to the sweeping frequency f.

The impact of the number of sub-intervals is difficult to interpret. First of all. it was defined in section 3.1 that the cut-off frequency of a sub-interval is calculated according to the frequency at the start of that sub-interval f_{start}, therefore $f_c = cut-off\_ratio \times h\_order \times f_{start}$. When the next sub-interval starts, f_{start} is updated. The higher N, the more f_{start} corresponds to the actual sweeping frequency and the filtering stage is less discrete. With this in mind, for small values of N the filter performance starts to deteriorate at end of the sub-interval, since the sweeping frequency is demanding the same evolution it presents to the cut-off frequency that remains constant in that sub-interval.

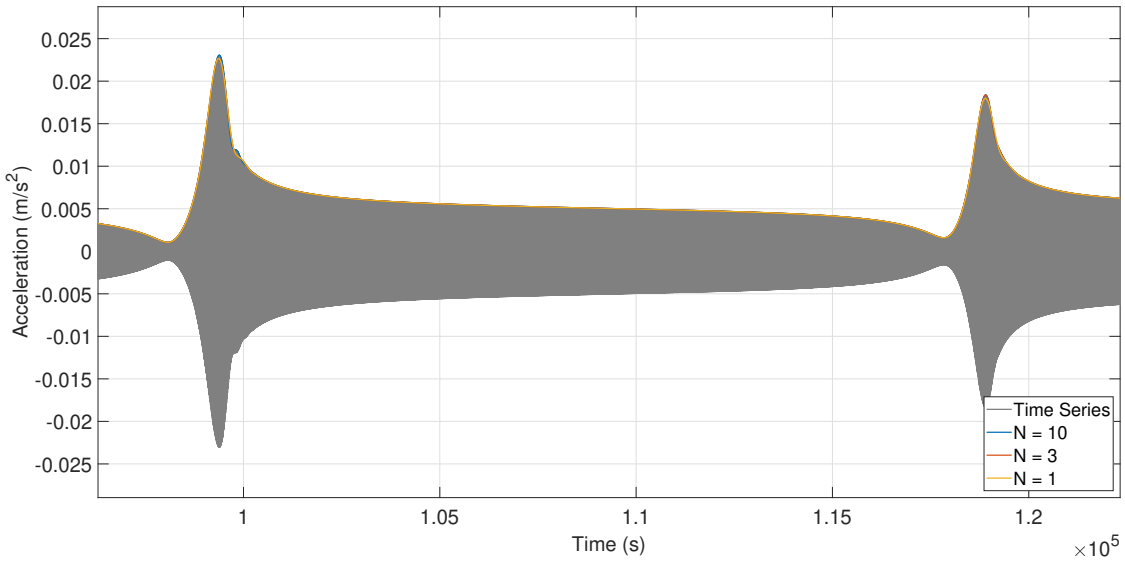

Figure 4.11: Cut-off ratio influence on estimation error, for DOF1.

In the current work it is important then to understand what values of N equate to the perfect scenario, continuous variable bandwidth filtering stage. The easy answer for this would be to consider very large values of N, however the CPU time would increase at the same rate, due to other wider filtered intervals. A compromise must be achieved. Figure 4.11 displays, by zooming in on the last two modes of the acceleration of DOF1, Figure 4.3, that the employemnt of $N = 10$ resulted in good tracking of the entire bandwidth, demonstrating why this is the referenced value for this work. The CPU time increased 12%, for $N = 3$, and 96%, for $N = 10$, when referenced to $N = 1$. It is also interesting to visualize the updating event of this procedure as the $N = 3$ curve equals the $N = 1$ curve for the 2^{nd} mode. Between

the two modes, the sub-interval for curve $N = 3$ is updated and good tracking is observed for the 3^{rd} mode.

The estimating error considering constant variable bandwidth $N = 1$ can be seen as satisfactory for this example, due to the absence of sudden variations in amplitude. The clear advantage is the simplicity and decreased CPU time it presents. However, there are situations with sudden amplitude variations, referring to Figure 3.12, where the need of $N > 1$ is clear.

Assuming an adequate value of N, in such a way that $f_{start} \approx f$, the impact of the cut-off ratio can be studied and its understanding is very important for future users of this technique, as it impacts the filtering performance uniformly in the excitation bandwidth. Its influence is more easily interpreted since f_c is proportional to this ratio. This analysis is done through the estimation error, in Figure 4.12. The differences are consistent all across the bandwidth. Higher cut-off ratios are associated with increased performance and the estimation error is smaller. The difference of 5% cut-off ratio and the 10% and 15% is more accentuated than the difference between 10% and 15%. Decreasing the ratio more than this exponentially increases this difference and the estimation error. The major drawback of increased cut-off ratios is the noise rejection, however due to the lack of signal disturbances, further conclusions on the influence of this parameter must be retrieved from experimental data.

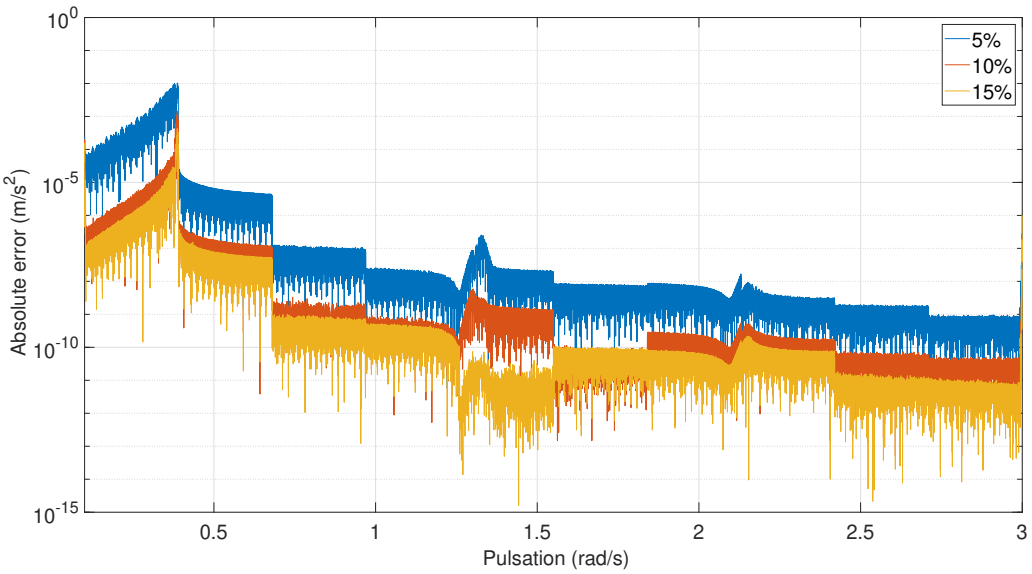

Figure 4.12: Cut-off ratio influence on estimation error, for DOF1.

4.2.2 Comparison with the Adaptive Filter

The adaptive filter is an LMS data driven method. A complete mathematical derivation of the algorithm can be found in Haykin and Widrow [34], with pratical applications in Abeloos et al. [33].

The adaptive filter and the MHDTF have the same purpose, obtain instantaneous Fourier coefficients.

The methodologies are non-identical, however both methods suffer from some of the same limitations. Most importantly is the discrepancy from the input signal frequency and its numerical assumption. Therefore, the estimation error, or residual error in the adaptive filter terminology, should provide an accurate contrast of the performance of both methods. The constructed NLFRCs are also a great benchmark to analyse.

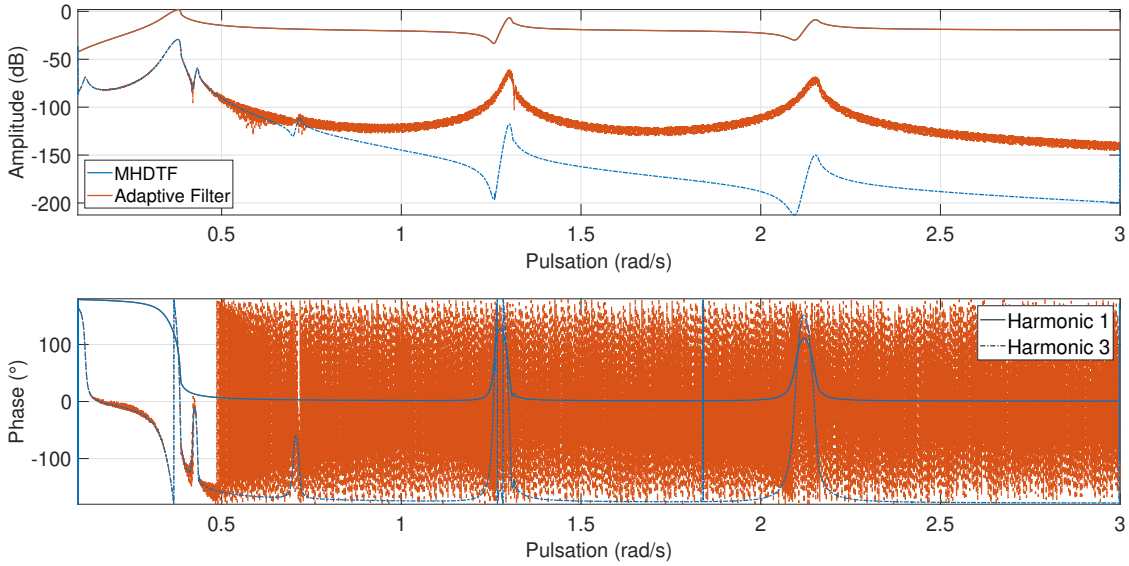

Figure 4.13: DOF1 acceleration NLFRC estimation, via MHDTF and Adaptive Filter.

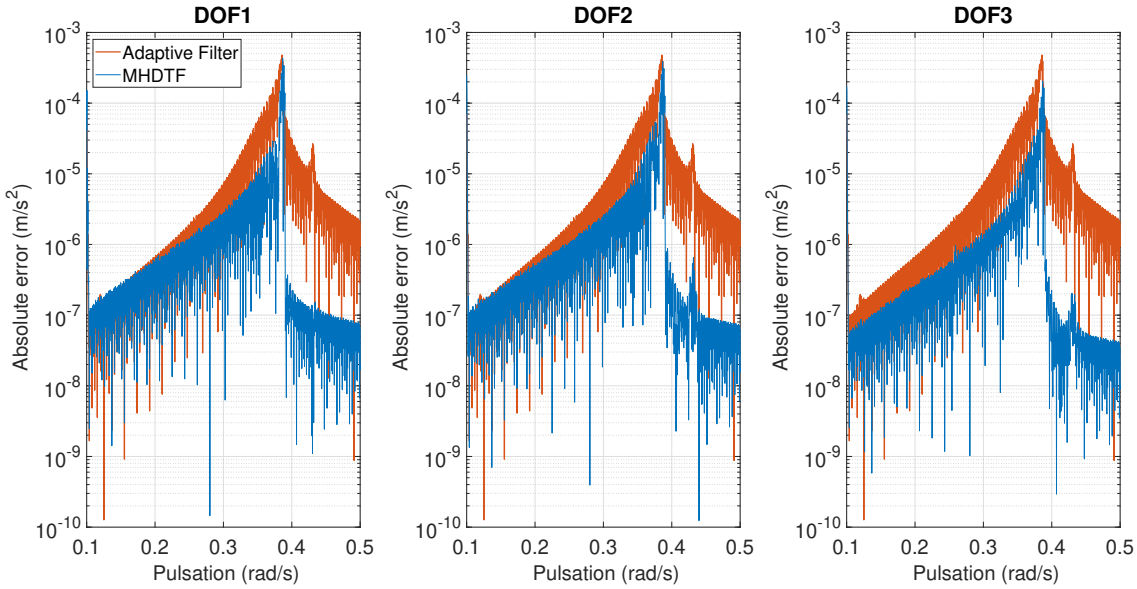

Figure 4.14: MHDTF and Adaptive Filter estimation error, for DOF1.

The structural NLFRCs are plotted in Figure 4.13 for the two methods. The estimations of harmonic 1 are clear and identical, in both amplitude and phase. Harmonic 3 is also very similar up to the vicinity of

0.5 rad/s. Beyond this range, the amplitude and phase of harmonic 3 for the adaptive filter estimation is clearly corroded. It is not the objective of this thesis to understand or explain the phenomena leading to this inaccurate estimation. As far as the author knows, this error may occur due to the unfamiliarity with the adaptive filter leading to a wrongful use of the algorithm, even though the guidelines of the state of the art were followed.

With this in mind, only the range of 0.1 rad/s to 0.5 rad/s is considered when evaluating the estimation error of both methods, plotted in Figure 4.14 for all DOFs. The MHDTF can be regarded as a more accurate tracking tool by a small margin, with both methods presenting the same peak of estimation error.

The comparison between these two methods is continued with experimental data.

4.3 Harmonic Balance Method Validation

Another important step to validate the MHDTF procedure is to compare the obtained results to the HB method. This numerical method produces a steady-state solution that establishes a great benchmark to compare to the MHDTF results.

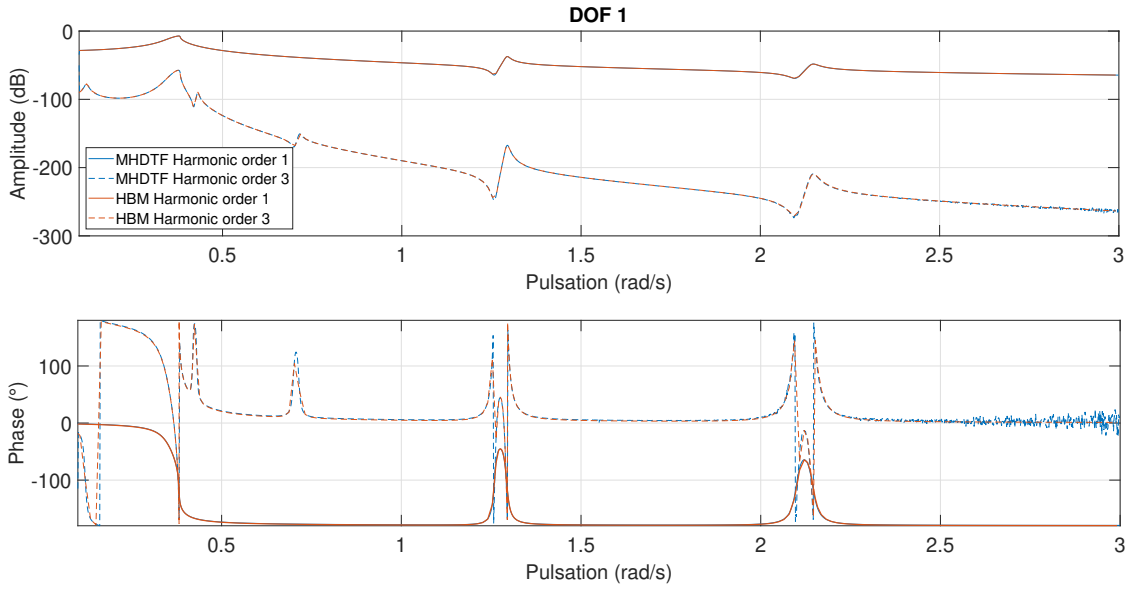

Figure 4.15: DOF1 displacement amplitude and phase of harmonic 1 and 3 per HB method and MHDTF tracking.

Regarding the two methods, there is a clear correspondence between the two responses for both harmonics up until the -250 dB amplitude level, where the interference mitigation reaches its limit and the tracking of harmonic 3 is clearly corroded. This is more evident for DOF2 and DOF3, where the amplitude of harmonic 3 is lower and it reaches this threshold value earlier in the simulation.

Discrepancies in the results may also stem from the simulation data itself, besides the already appointed limitations of the MHDTF procedure. For instance, tolerance errors used in the Newmark simulation, as well as transient. These flaws were not relevant in the analysis estimation error since the contrast was made with the simulated data. Now it is done with the HB method results, that are steady-state solutions.

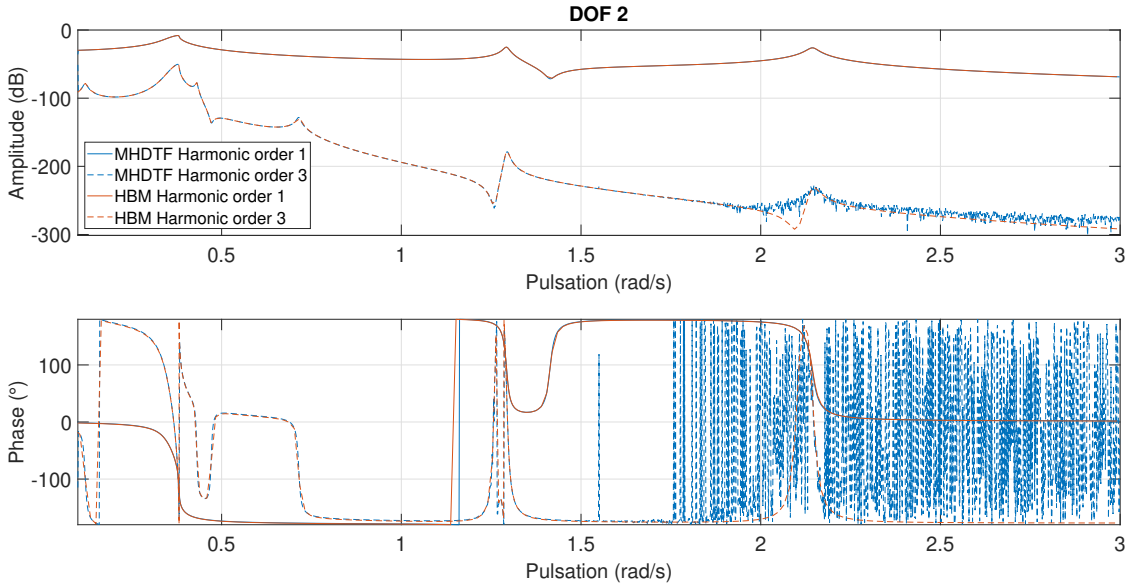

Figure 4.16: DOF2 displacement amplitude and phase of harmonic 1 and 3 per HB method and MHDTF tracking.

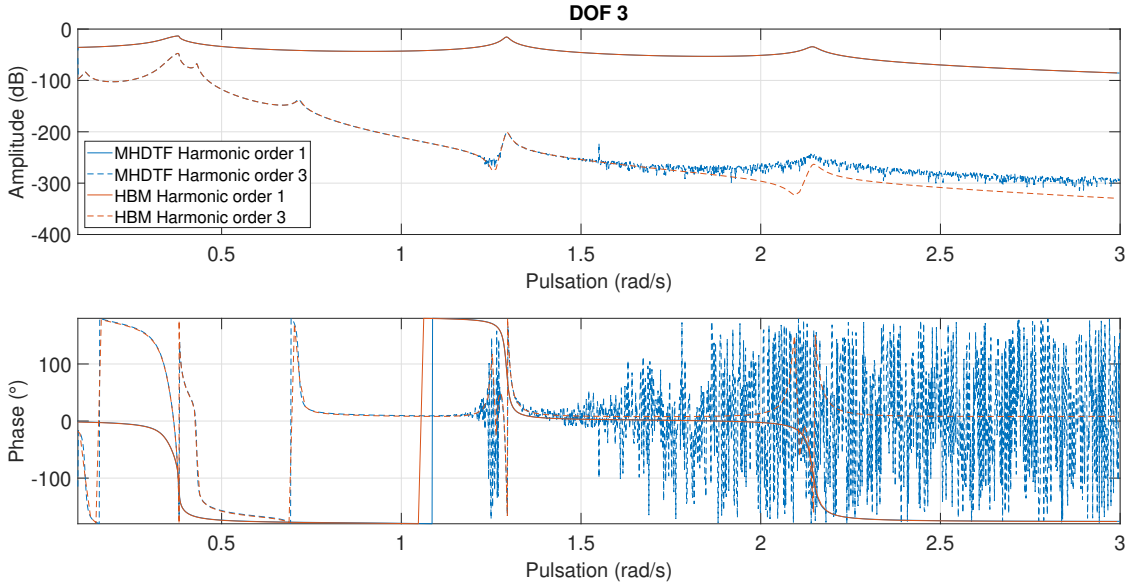

Figure 4.17: DOF3 displacement amplitude and phase of harmonic 1 and 3 per HB method and MHDTF tracking.

Chapter 5

Application on Experimental Testing Data

After the validation of the method with simulation data, analysing experimental data poses different challenges. The disturbances in the signal can lead to errors in the estimation. In Musella et al. [1], the single-harmonic DTF has proven to be more effective at attenuating these disturbances than the harmonic estimator and it is important to verify if this is true for the higher orders.

Since the higher harmonics frequently respond at lower amplitude, the estimation of these is more influenced by the disturbances, specially when pairing to this estimation are higher cut-off frequencies, as higher as the harmonic order is, that reject disturbances less efficiently.

Therefore, it is vital in the assessment of the MHDTF performance the analysis of experimental data and the particular effect of lower cut-off ratios in Nonlinear Frequency Response Curves (NLFRCs) construction and multi-harmonic sum. The MHDTF will also be contrasted with the adaptive filter.

5.1 Experimental Setup

The experimental setup of an airplane mock-up is shown in Figure 5.1. It is composed of wings, tail, with horizontal and vertical stabilizers, fuselage and two masses simulating the engines connected via pylons to the wings. Despite of the simple design, its dynamic behavior presents several complex nonlinear phenomena. The source of nonlinearity arises mainly from the two pylons under the wings, but also the bolted connections between the different components. Moreover on the pylon, its nonlinearity emanates from large beam deformations and contact beam-top masses.

The airplane is suspended through elastic bungees, as in a Ground Vibration Test (GVT), reproducing free-free conditions. The acceleration response was measured using 27 accelerometers placed along the entire structure. A total of 21 accelerometers used were uniaxial and six triaxial for a total of 39 DOFs. The excitation is provided by two eletrodynamic shakers approximately at the center and beneath

each wing. The connection between the shakers and the experiment object was done with stingers. On top of the stinger, force cells record the excitation to the structure. The accelerometers and force cells are connected by cables to a Simcenter SCADAS Lab. It is important to avoid their interference with the mechanical system. Tape was also placed beneath the accelerometers in order to attenuate any electrical interference between the devices. The effect of the accelerometers mass loading on the experiment must be minimized, therefore, the accelerometers of the engine masses are the lighter miniature models. All the data acquisition was made using the Simcenter Testlab.

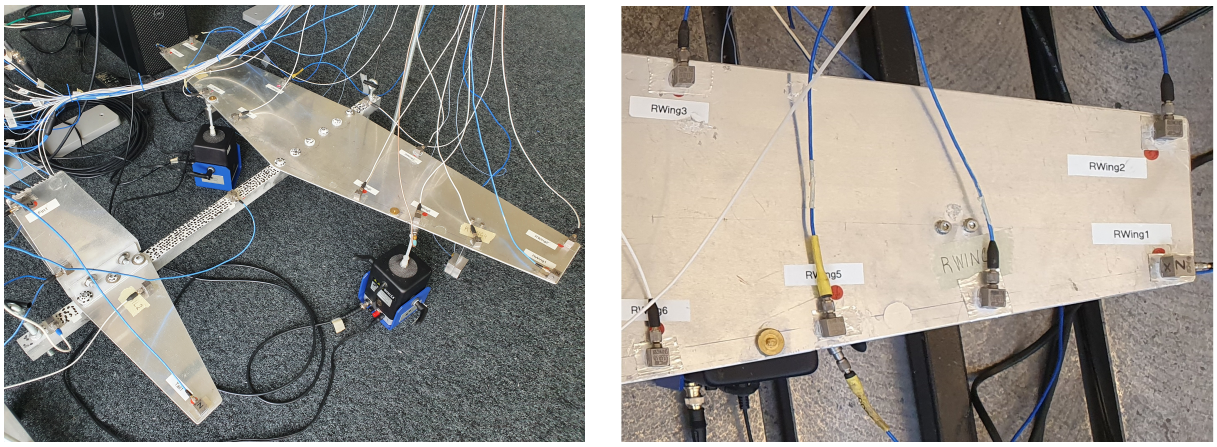

Figure 5.1: Experimental setup.

The input of the shakers, the drives, have a constant spectrum along the excitation bandwidth, with a determined voltage amplitude. However, the excitation force of the experiment is not so straightforward. Some coupling between the shaker and the structure can not be avoided, the shaker becomes an active part of the tested system and the response of the structure may impact the input force. As a consequence, it differs significantly from the constant spectrum drive inputted to the shaker. Therefore, it must be recorded and processed by the MHDTF to compute the structural NL-FRCs.

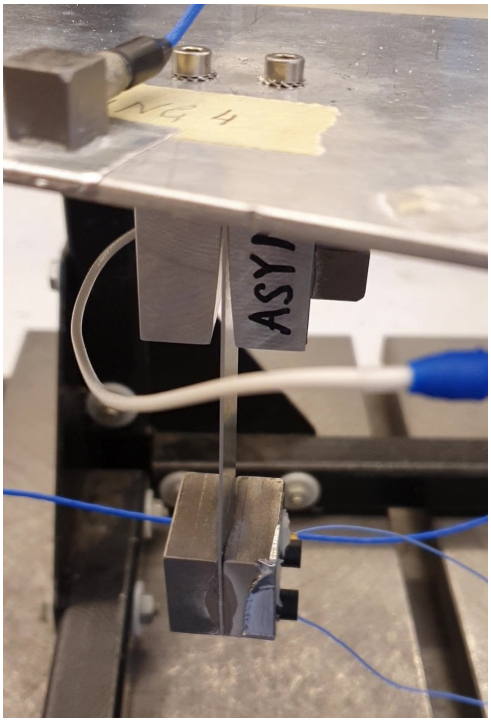

Figure 5.2: Nonlinear pylon connection.

The experimental runs had a logarithmic excitation bandwidth of 5Hz to 110Hz, for a sweep rate of 0.4 octaves per minute, totalling 11 minutes and 9 seconds per run. Section 2.1.1 demands that, since two forces are applied, two testing sweeps, or runs, must be done. Additionally, the force configurations of the sweeps must differ, so, in the second sweep the force applied on the right wing, cited as RWing Force, has a phase difference of $180°$ referencing to the force on the left wing, LWing Force. The first sweep is symmetric and second one is

antisymmetric.

5.2 MHDTF Application

The MHDTF procedure is applied on the measured acceleration time series. In an effort to reduce data processing, out of all the 39 DOFs, particular attention is given to the pylon and wings DOFs, since these are most affected by the pylon nonlinearity. These DOFs are labeled as LWing and LPyl if they reside on the left side of the wing and RWing and RPyl for the right side of the wing. They are also numbered from LWing1 to LWing6,according to Figure 5.1, and LPyl1 to LPyl3. As visible in Figure 5.2, Pyl1 is situated at the pylon connection as Pyl2 and Pyl3 in the mock-up engine mass itself. This configuration is chosen to detect the pylon torsional mode.

The MHDTF processing parameters were: number of sub-intervals N equal to 10 and the cut-off ratio 10%, instead of the previously referenced values for simulation data due to disturbance presence in the signal. This presence can also be more disruptive to the estimation than the harmonic interference. Therefore, for computation efficiency, the harmonic interference mitigation stage is ignored in the shown identifications.

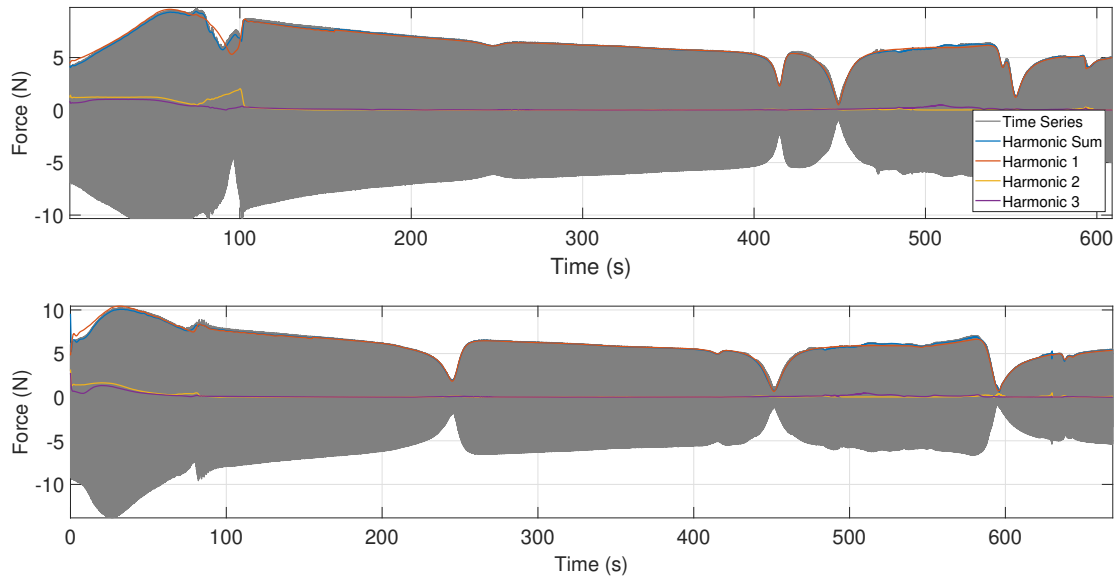

Figure 5.3: LWing (top) and RWing (bottom) force signals and respective amplitude tracking, sweep 1.

First, it is convenient to point at the nonlinear effects on the input forces of the structure, labelled LWing Force and RWing Force, due to the aforementioned shaker-structure relation. In Figure 5.3, the amplitude tracking of harmonic 1, 2, 3 and their sum is displayed. A moderate impact of harmonic 2 and 3 on the signal is verified from 0s to 100s. The shaker-structure coupling effects are clear: the harmonic sum is not leveled or even single-harmonic, even though the voltage inputted to both shakers is. Sweep 2, not displayed in this work, presents the same features.

The time series of the measured acceleration and respective tracking of harmonics 1, 2 and 3 from the MHDTF, and their sum, of RWing3, sweep1, and Rpyl2, sweep2, are portrayed in Figure 5.4 and Figure 5.5, respectively.

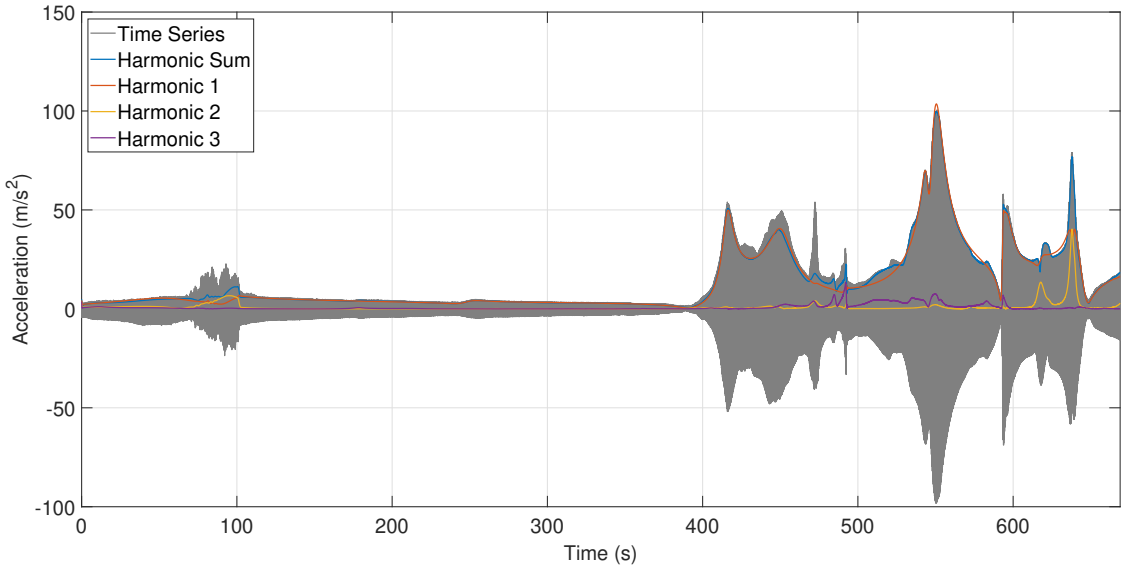

Figure 5.4: RWing3 acceleration amplitude envelope, sweep 1.

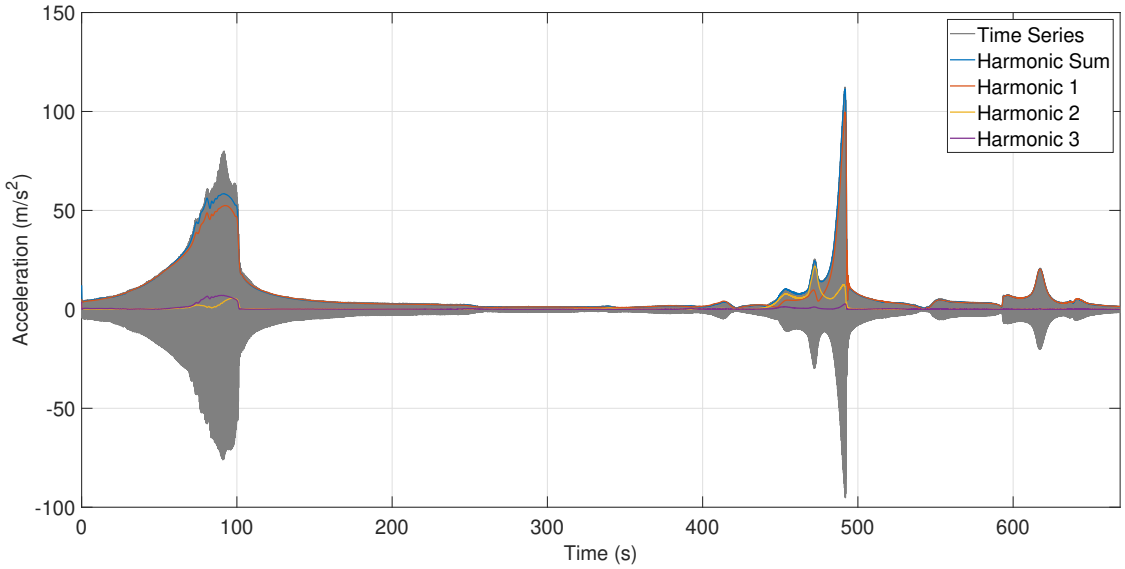

Figure 5.5: RPyl2 acceleration amplitude envelope, sweep 2.

The harmonic 2 and 3 contribution in these estimations is significant, specially when resonances are excited. In Figure 5.4, these can be mainly identified at 90s and at 620s and 640s with a primary

harmonic 2 contribution. Figure 5.5 indicates a sizeable harmonic 3 contribution at 90s and harmonic 2 at 460s and 490s. the consequent identification error that is committed in identifying the fundamental harmonic only is hence very clear at these time ranges.

In all the time series presented and consequent estimations, Figure 5.3, Figure 5.4 and Figure 5.5, the difference of the harmonic sum and the time series amplitude envelope may manifest efficient noise rejection of the MHDTF and/or the need of higher order harmonics tracking. However, the tracking of harmonic 4 and 5, not presented in this thesis, lead to insignificant contributions, that is why only harmonics 1, 2 and 3 were tracked. Additionally, regarding Figure 5.4 and Figure 5.5, this difference is very noticeable in the 70s to 100s range. It is in the 10% range for Figure 5.5 but it is even more accentuated for Figure 5.4. Noise may be disregarded as the cause in this extreme situation and there can be a clear estimation error. Less trivial causes could point to nonlinear chaos phenomenon or other particular nonlinear effects.

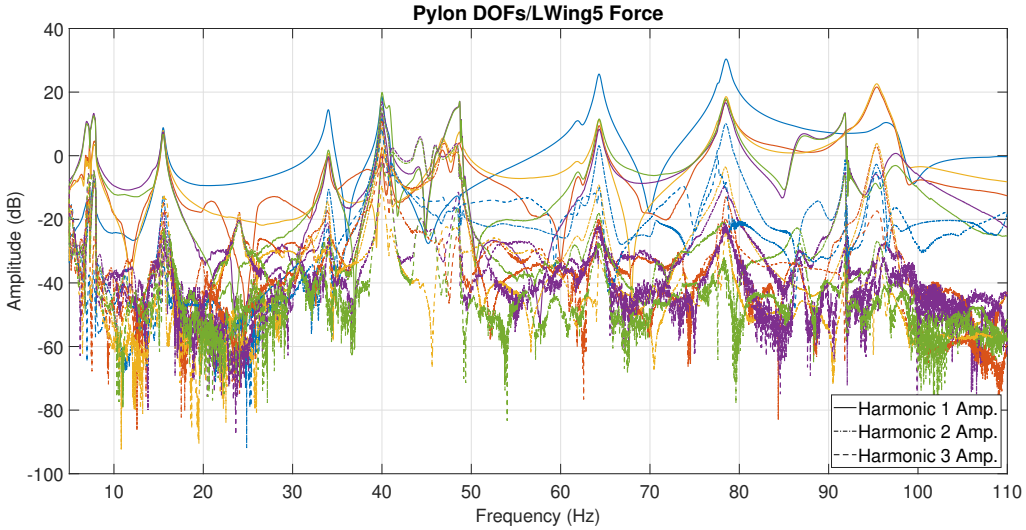

Figure 5.6: NLFRC amplitude estimation for RPylon and LPylon DOFs/LWing Force.

Moving on to structural NLFRCs. All the pylon DOFs, except for RPyl1 since its acceleration was incorrectly captured, are included in Figure 5.6. In Figure 5.7, the NLFRCs LWing5,6 and RWing5,6 are also displayed. The computation of these NLFRCs for the various harmonic orders was done as detailed in subsection 3.3.3.

The amplitude of the NLFRCs is expressed in dB. Due to the many DOFs displayed, the interpretation of these figures is not trivial. Nonetheless, the goal from the point of view of the reader is to perceive the clear contribution of the higher-orders. At some modes, the amplitude of harmonic 2 and 3 is higher than harmonic 1, for example, at 40 Hz. The $x - axis$ shift to frequency and the overlap of the many DOFs allows the identification of the modes of the structure. This identification is not detailed as it is not the objective of this dissertation.

Furthermore on the NLFRCs, the MHDTF is not fully capable of attenuating the noise. The estimations of harmonic 2 and 3 at lower amplitudes are close to noise floor and it becomes very hard to identify

clean curves. This occurs for almost the entire bandwidth of Figure 5.6 and mainly from 5Hz to 30Hz for Figure 5.7. As investigated further in subsection 5.2.1, cleaner NLFRCs would have been obtained if a 5% cut-off ratio was considered.

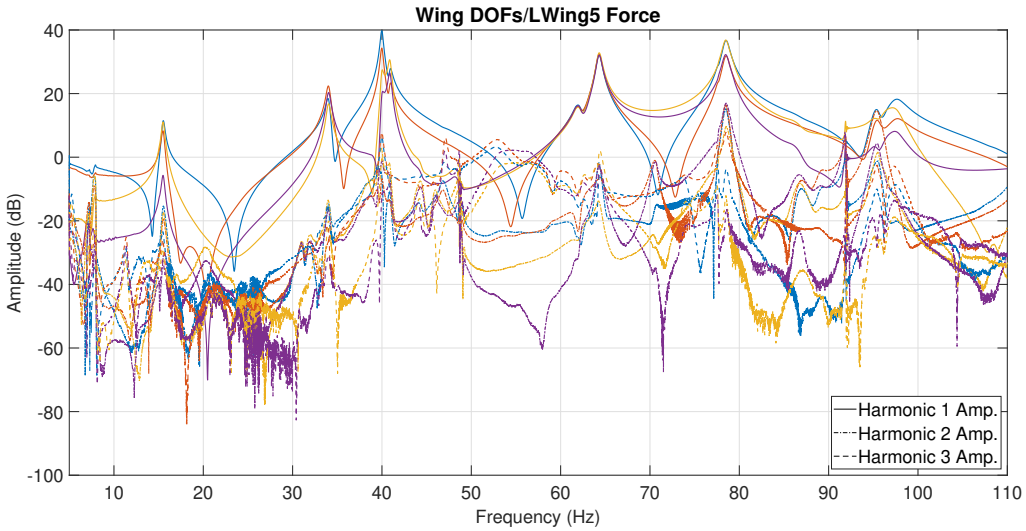

Figure 5.7: NLFRC amplitude estimation for LWing5,6 and RWing5,6 DOFs/LWing Force.

5.2.1 MHDTF Parameters Influence

The analysis of the MHDTF parameters in experimental data is crucial in the full awareness of its performance. The parallel analysis made on simulation data, subsection 4.2.1, gave a great foundation of what to expect in experimental data. Recollecting what was previously concluded, it is important to identify the number of sub-intervals N that induces $f_{start} \approx f$. In Figure 5.8, it is perceived that once

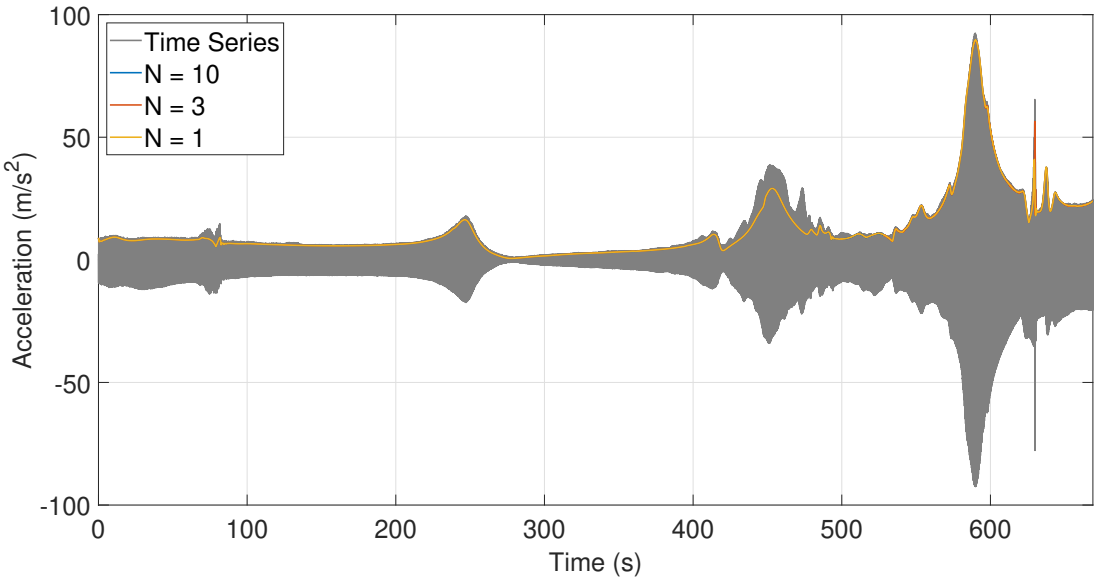

Figure 5.8: Number of sub-intervals influence on harmonic sum estimation for RWing3, sweep1.

again $N = 10$ is a conservative value, hence the one being employed in this chapter.

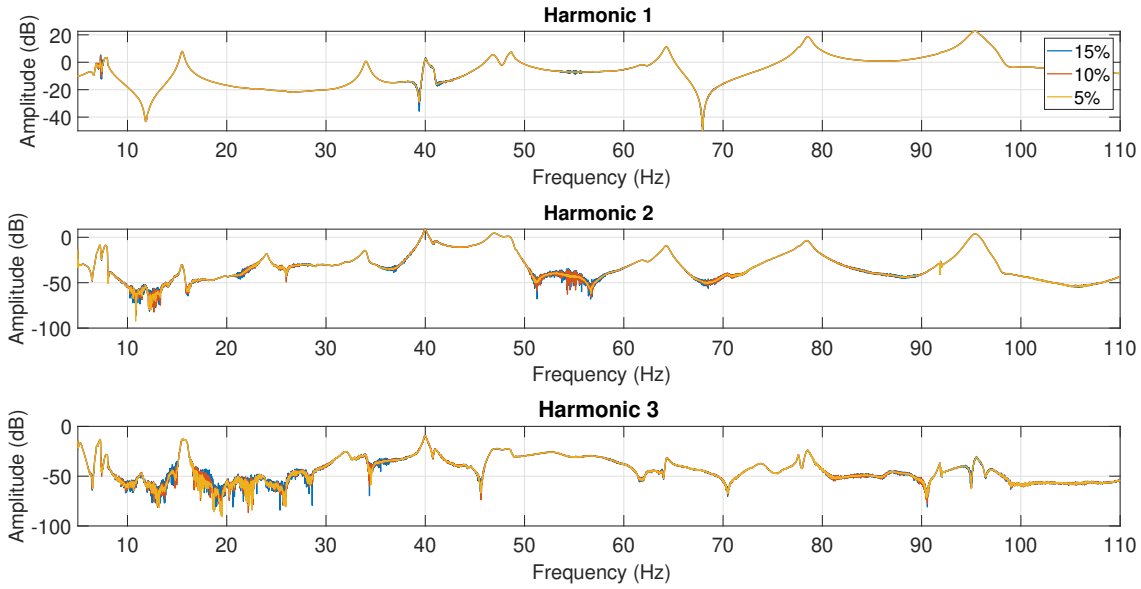

Figure 5.9: Cut-off ratio influence on NLFRC amplitude estimation for LPyl3/LWing Force.

From here, the influence of the cut-off ratio, central in this process, can be studied. The objective is to understand the balance between efficient noise rejection, leading to better NLFRCs that are paramount in the grand scheme of system identification, while assuring the tracking is adequate in general and particularly on sudden amplitude variations like beating phenomenon, consequently improving the signal reconstruction and its possible applications.

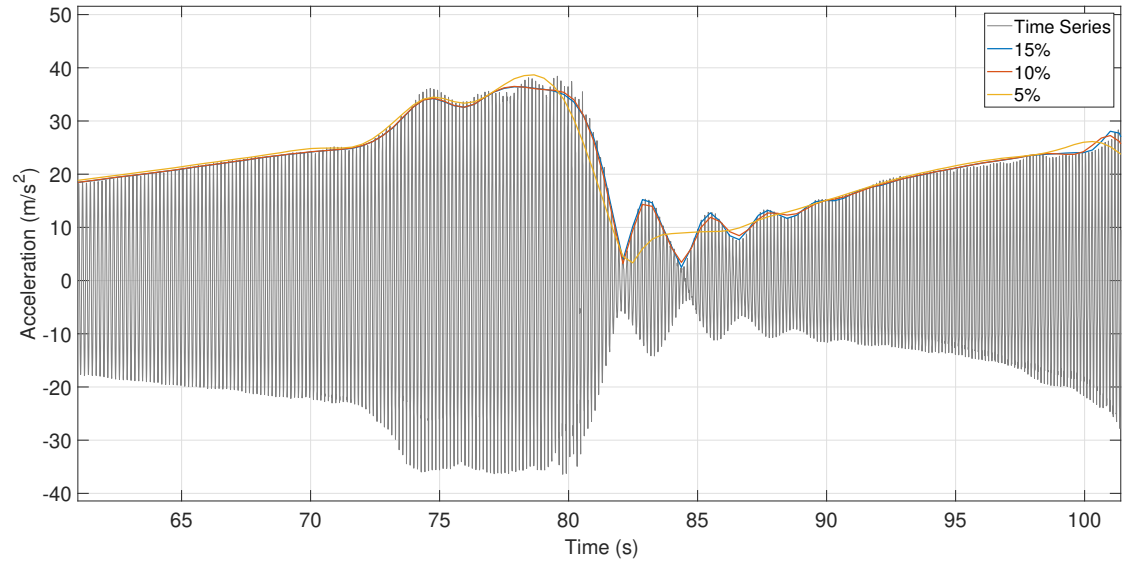

Figure 5.10: Cut-off ratio influence on harmonic sum estimation, for LPyl3, sweep2.

The performance associated with 10% cut-off ratio appears to be the best of both worlds. In Figure 5.9, the noise rejection is better, comparing to the results for 15%, and slightly inferior, referenced to 5% cut-off ratio, being significant for harmonic 2, at 54Hz. From Figure 5.10, the implications of the 5% cut-off ratio are clear, it fails to track the sudden variations in amplitude. The estimations of 10% and 15% are more responsive, with the latter being marginally better, as expected.

5.2.2 Comparison with the Adaptive Filter

Comparing the estimations of the MHDTF on experimental data with other techniques create a great benchmark for industry applications, understanding where the advantages and disadvantages are of both methods. The adaptive filter, as already introduced, has the capability of tracking higher order harmonics and a previous comparison with the MHDTF was initiated with simulation data. It was concluded that the MHDTF was able to better track the lower amplitude of the higher-orders but the major challenge resides on the noise rejection efficiency.

From Figure 5.11, the MHDTF is more effective in rejecting disturbances when comparing to the adaptive filter. This is evident for harmonic 1, at around 45 Hz, and for harmonics 2 and 3 all across the bandwidth. The MHDTF cut-off ratio utilized is 10%, meaning that there is more room for improvement as analysed in Figure 5.9.

From Figure 5.12, the tracking accuracy is compared for the adaptive filter. The adaptive filter harmonic sum is more reactive to the sudden amplitude variations. It better aproximates the time series, however it also displays a noisier sum. The accuracy of the MHDTF could be maximized at the cost of noise rejection, by employing a higher cut-off ratio.

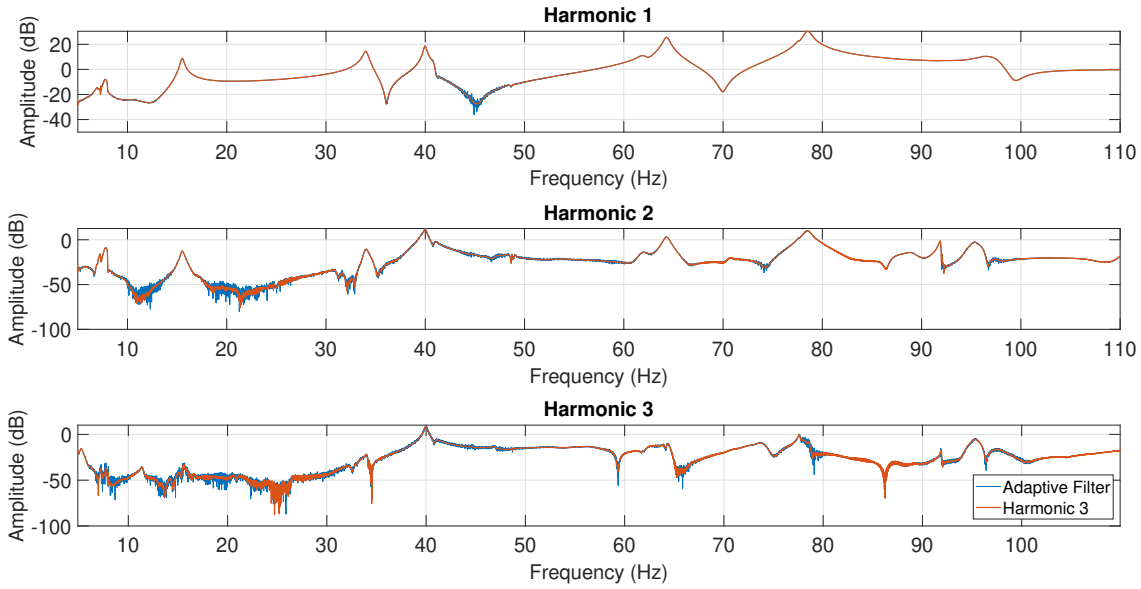

Figure 5.11: NLFRC amplitude estimation for LPyl1/LWing Force, via MHDTF and Adaptive Filter.

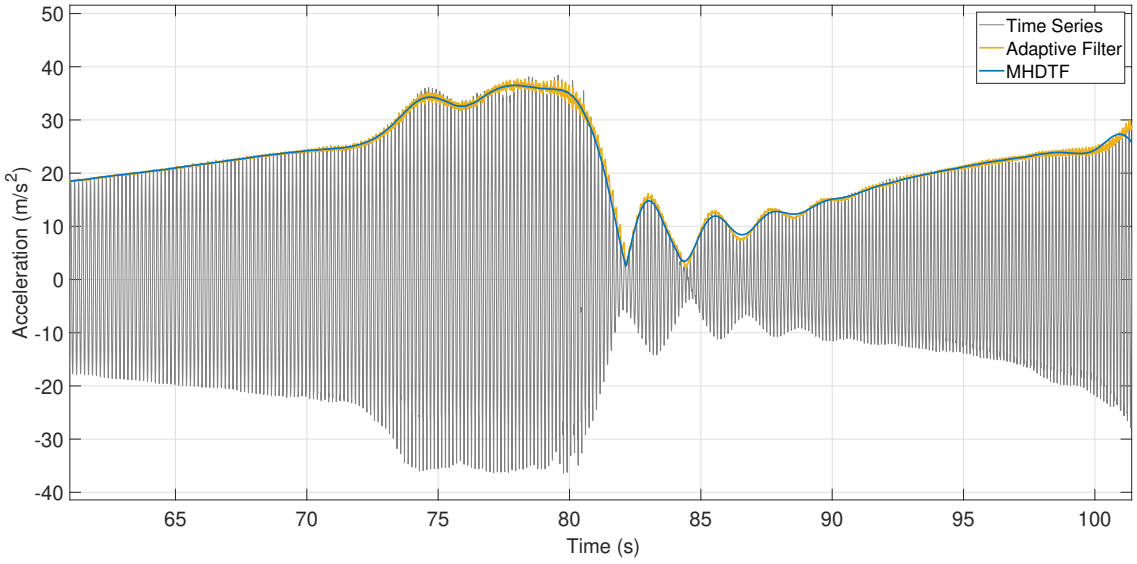

Figure 5.12: LPyl3, sweep2, acceleration signal and respective harmonic sum estimation, via MHDTF and Adaptive Filter.

5.2.3 Control Applicability

In this section, it is discussed the potential applicability of the MHDTF in real-time controllers. The method developed in SIMULINK, section 3.2, emulates what would be online processing. As a result, the *filtfilt* function is not applicable: the filtering stage is causal and the group delay inherent to the filter will be manifested in the resultant estimations.

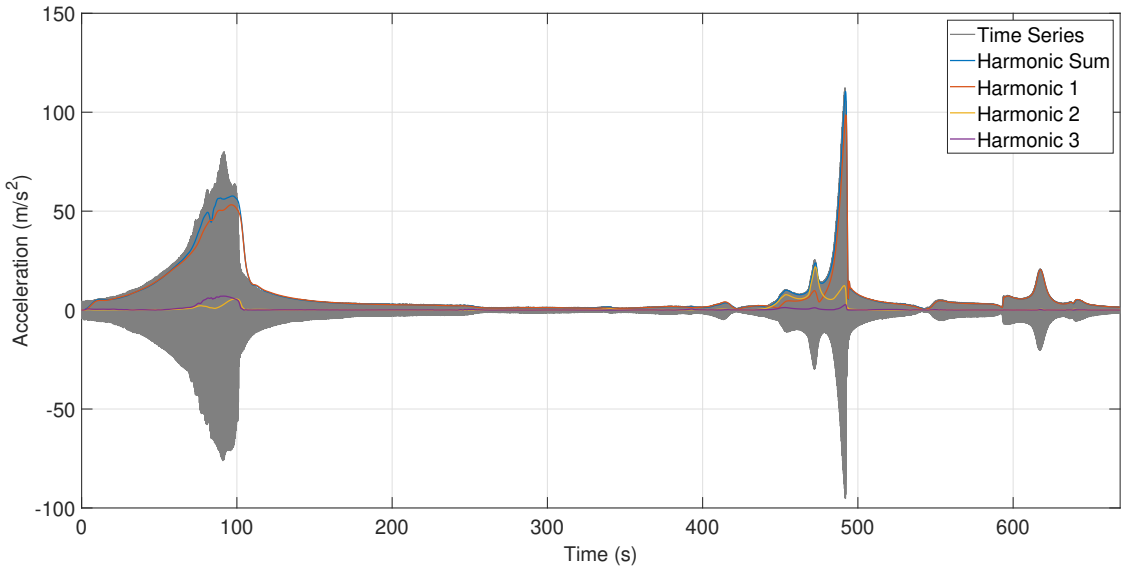

Figure 5.13: RPyl2, sweep2, acceleration signal and respective online MHDTF tracking.

The group delay is visualized in Figure 5.13. The shift of the amplitude envelope of the time series and the harmonic sum is significant in the early instants of the time series. In the later modes, it is much less detectable, confirming the higher cut-off frequency, less group delay relation indicated in Figure 3.10.

Besides analysing the performance of the online tracking, it is also interesting to compare it to its offline counterpart. Both lowpass filters employed have the same parameters: Butterworth design, filter order 4 and 10% cut-off ratio.

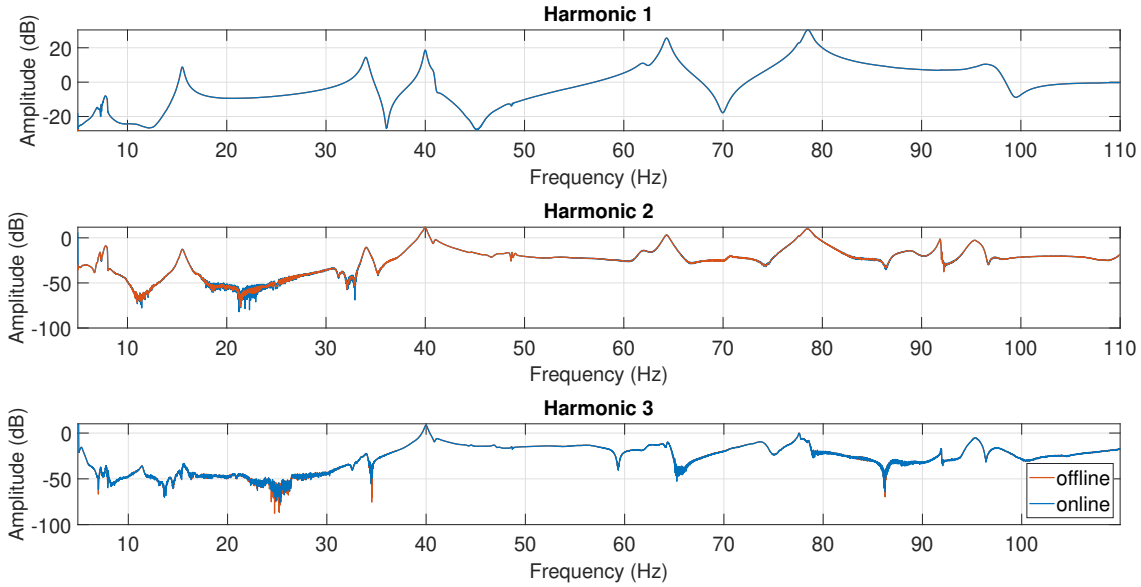

Figure 5.14: LPyl1/LWing Force acceleration NLFRC estimations, online and offline.

In Figure 5.14, the NLFRCs amplitude estimations of harmonic 1,2 and 3 of the online MHDTF procedure are compared with the offline MHDTF procedure. Althought not very perceptible, the group delay is also visible. Regarding the noise rejection, it is very similar as expected. Harmonic 2 is somewhat more clear for the offline procedure, while the reverse happens for harmonic 3.

Chapter 6

Multi-Harmonic State-Space Modelling

From the results obtained in chapter 4 and 5, the Multi-Harmonic Digital Tracking Filter (MHDTF) is proven to be an efficient tool to estimate the multi-harmonic response of a nonlinear system under swept-sine excitation. The subject of this chapter is then to investigate potential use in the nonlinear system identification area.

Hugely facilitated by state-of-the-art tools in the linear system identification and modal analysis fields, many conveniently embedded in the Siemens Testlab software, the proposed methodology attempts to linearise a nonlinear structure, through its harmonic estimations provided by the MHDTF, and create a multi-harmonic State-Space (SS) model. The advantage of this approach is its simple use and the possibility to better approximate a response with multi-harmonic contributions. The clear drawback lies in the linearisation, hence, its accuracy only at the level of excitation used during the identification.

6.1 Theoretical Synopsis

In this section, the employed techniques are briefly introduced: PolyMAX and MLMM to obtain the modal model and then the posterior conversion to SS model.

6.1.1 PolyMAX and MLMM

PolyMAX is referenced as a new standard for modal parameter estimation, as introduced in Peeters et al. [35]. It is a non-iterative frequency-domain parameter estimation method based on a weighted least-squares approach. It constructs a modal model, by extracting, from MIMO FRFs, a meaningful set of modes and their associated modal parameters including: natural frequencies, damping values and mode shapes.

PolyMAX relies on modal fitting process, comparable to that used for curve fitting. Different polynomial orders are tested during the curve fitting process, and the polynomial coefficients are then calculated to reduce the discrepancy between the curve and the data. Similar steps are taken in the calculation of

modal curves, where varying numbers of modes are taken into account before determining the modal shapes, natural frequencies, and modal damping values to best match the measured FRFs.

Shortly, PolyMAX, in its procedure, starts with the creation of a stabilization diagram containing frequency, damping and participation information. From here, the modal modes are selected, either by the user or automatically. A faithful mode selection is important, they must correlate the modes from the inputted FRFs. After, the mode shapes and the upper and lower residuals are calculated. The modal model is then characterized by its transfer function, or FRF, $H(s) \in \mathbb{C}^{n_o \times n_i}$, Equation 6.1, as a linear sum of the different n_m modes, with the inclusion of the upper $UR \in \mathbb{R}^{n_o \times n_i}$ and lower $LR \in \mathbb{R}^{n_o \times n_i}$ residuals. $\psi_r \in \mathbb{C}^{n_o \times 1}$ corresponds to the mode shape column vector, $\lambda_r \in \mathbb{C}$ to the mode from which the natural frequency and damping ratio are obtained and $L_r \in \mathbb{C}^{1 \times n_i}$ is the participation factor row vector.

$$H(s) = \left(\sum_{r=1}^{n_m} \left(\frac{\psi_r L_r}{s - \lambda_r} + \frac{\psi_r^* L_r^*}{s - \lambda_r^*} \right) \right) + \frac{LR}{s^2} + UR \tag{6.1}$$

The equation is more compactly written as Equation 6.2. $\Psi \in \mathbb{C}^{n_o \times 2n_m}$ contains the mode shape vectors and their complex conjugates, $\Lambda \in \mathbb{C}^{2n_m \times 2n_m}$ contains all the modes and their complex conjugates and $L \in \mathbb{C}^{2n_m \times n_i}$ contains all the participation factors and their conjugates.

$$H(s) = \Psi \left[sI - \Lambda \right]^{-1} L + \frac{LR}{s^2} + UR \tag{6.2}$$

Validation of the obtained modal model can be obtained with the comparison of the synthesized FRFs, as constructed in Equation 6.2, and the originally inputted FRFs. Additionally, validation can also be obtained from the Modal Assurance Criterion (MAC). An in-depth guide on the correct utilization of PolyMAX is found in [36].

In order to improve the fit of the modal model, that is, a better match of the synthesized FRFs, the Maximum Likelihood estimation of a Modal Model (MLMM) algorithm can be employed [37]. MLMM automatically iterates on the parameters of the initial modal model to optimize the fit between the identified model and the inputted FRFs. A guide on its use can be found in [38].

6.1.2 State-Space and Modal Model Conversion to Modal State-Space Model

The SS model is a method of representing dynamical systems. It transfers observations of a response variable to unobserved states or parameters by an observation model. These state variables describe a system of first-orders differential equations, reducing its complexity. The continuous-time state space model consists of Equation 6.3a, state equation and the observation equation, Equation 6.3b. The calculated output response, in the time domain, $y \in \mathbb{R}^{n_o \times 1}$ is calculated as a function of the n internal states vector $x \in \mathbb{R}^{n \times 1}$ of the system through the output matrix $C \in \mathbb{R}^{n_o \times n}$ and of the input vector $u \in \mathbb{R}^{n_i \times 1}$ through the direct throughput matrix $D \in \mathbb{R}^{n_o \times n_i}$. In this case, D is null. $A \in \mathbb{R}^{n \times n}$ corresponds to the state matrix and $B \in \mathbb{R}^{n \times n_i}$ to the input matrix.

$$\dot{x} = Ax + Bu \tag{6.3a}$$

$$y = Cx + Du \tag{6.3b}$$

The state space model also allows for the construction of the transfer functions of the system, as in equation Equation 6.4.

$$H(s) = C\left[sI - A\right]^{-1} B + D \quad \in \mathbb{C}^{n_o \times n_i} \tag{6.4}$$

The similarities of Equation 6.2 and Equation 6.4 provide the basis for the conversion of the modal model to SS model where the calculation of a time series response is possible. The work of Elkafafy and Peeters [39] covers in depth this pairing of the modal and SS model.

6.2 Methodology and Guidelines

As in chapter 3, it is easier to first introduce the procedure and outcomes for linear systems and then dive into the nonlinear implications and consequent changes.

Briefly, the response time series contain the behaviour of the structure to a specific input force. This behaviour is then generalized in the FRFs. From here, the curve fitting algorithm creates the modal model that best approximates these FRFs and therefore the structure itself. This model is converted to a SS model, in the aforementioned A, B and C matrices. From Equation 6.3, only the input force u is missing to calculate the simulated time response y. In structural utopia, if the same input vector that originated the time series and FRFs of the system is provided to the SS simulation, y matches the response time series. Additionally, different input force u should numerically predict the actual response of the structure to the same u.

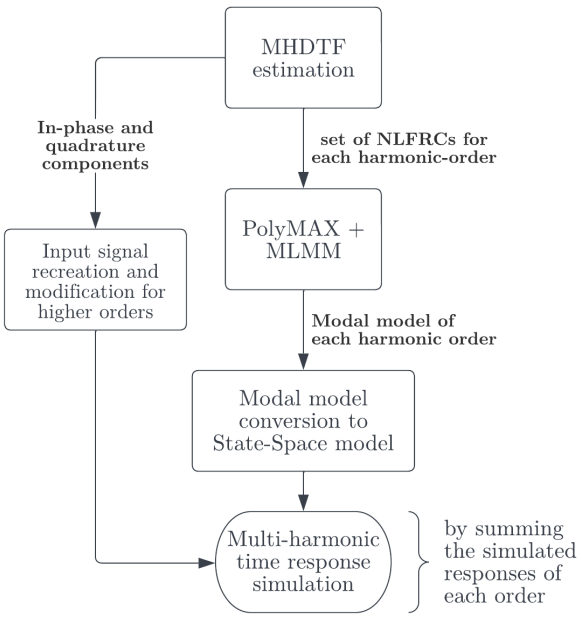

Figure 6.1: Multi-harmonic State-Space modelling and simulation procedure.

The first predicament of nonlinear systems is that they also respond at their harmonics. Therefore, directly applying this procedure on the fundamental harmonic only, as is only possible without the multi-harmonic estimations of the MHDTF, would register the same errors that the single-harmonic DTF does, as many times indicated in this thesis.

Second predicament is that the concept of FRF falls. The behaviour of the structure is not generalized and the NLFRCs are only specific to the input force that generated it. Therefore, predicting the behaviour of the response of the structure to different inputs than the one that originated this modal system will not lead to good predictions. The main objective of this work is then to accurately predict the response for the same input that originated the SS model.

The proposed procedure of multi-harmonic SS modelling and respective time domain simulation is proposed in Figure 6.1. In this section, each block of the diagram is introduced and explained. Certain guidelines of the procedure are also provided.

6.2.1 MHDTF Estimation

Utilizing the MHDTF is the first step. The time series, either simulated or acquired from experimental testing, are processed. The purpose is to obtain a set of high-quality NLFRCs for each tracked harmonic. For this, the estimator employed is the H_1 estimator. Just like the previous NLFRCs estimations in this thesis, the harmonic 1 tracking of the input force were considered as the input of the estimator and, as outputs, the tracking of the respective harmonic-order. In this phase, it is important to consider the influence of the different cut-off ratios, in the 5% to 15% range, on the quality of the NLFRCs, specially for the higher orders. The analysis of the influence of this parameter in subsection 5.2.1 has shown that the employment of a 5% cut-off ratio leads to increased noise rejection at the cost of tracking accuracy. This disadvantage may be ignored in the pursuit of more refined NLFRCs that are more easily interpreted by PolyMAX.

Another requirement of the use of estimated NLFRCs in PolyMAX is the associated frequency vector. While in this thesis, the plotted results are always associated with the fundamental sweeping frequency, for ease of representation, the sets of this procedure must be related to their ”true” frequency. As an example, if the excitation BW is from 1Hz to 10Hz, the harmonic 2 estimations must be represented from 2Hz to 20Hz.

Additionally, if the simulated time response objective is to compare its results to the time series that originated it, the MHDTF also has the purpose of providing the in-phase and quadrature components of harmonic 1. More on this will be more conveniently entailed further in this section.

6.2.2 PolyMAX + MLMM

Following, the modal models of each harmonic order are obtained utilizing PolyMAX. In a nutshell, each harmonic order is processed as its own individual system to process, with its own modal model and respective modal parameters.

In this framework, particular guidelines towards this methodology are detailed. Modal validation from the perspective of the user should focus on obtaining a proper fit of the synthesised FRFs, as the modeset and consequently MAC validation have a secondary value in this application. The fit really is of primary importance to have good time predictions. While this has proven to be fairly achievable for the fundamental harmonic, the higher orders have proven to be quite troublesome as observed in Figure 6.6, since the NLFRCs can be corroded by noise or harmonic interference. Additionally, using a curve fitting method designed for linear systems on nonlinear systems can contribute to the poor modal validation.

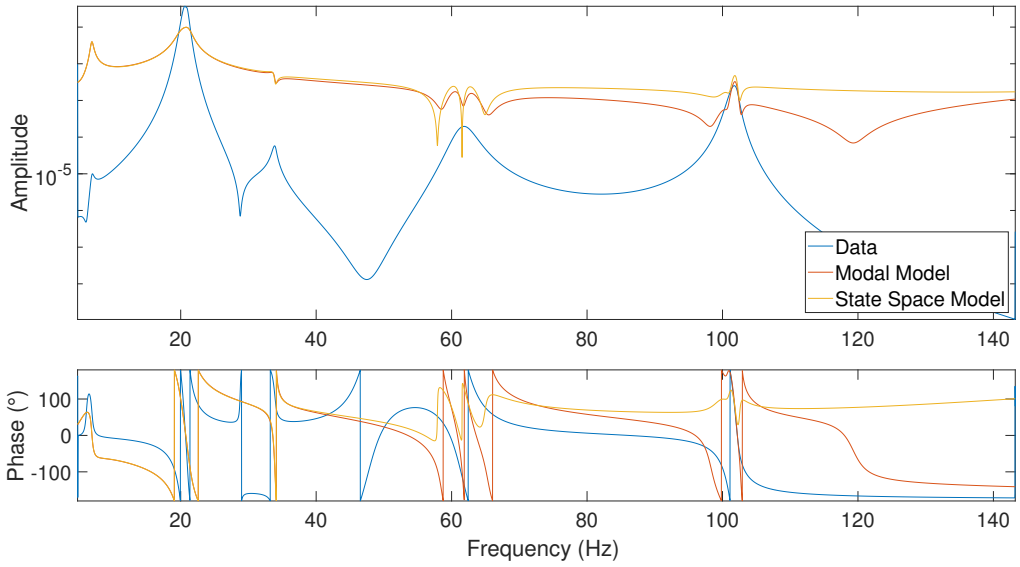

Figure 6.2: Modal synthesis before MLMM.

In this context, the user should guide the fit towards the modes with higher amplitude as these are the main contributors in the grand scheme. In a way, with the employment of MLMM, this is already done, since this algorithm may shift several modes to one resonance, as observed from the modal models differences from Figure 6.2 to Figure 6.3. The superharmonic modes that were selected were not resulting in a proper fit, neither for the superharmonic resonance or the resonance. MLMM shifted these superharmonic resonance modes to the resonance, thus obtaining a proper fit solely at this higher amplitude. This proved to be efficient in this work, however different scenarios may require different solutions.

The consequent conversion of the modal models to SS models is done according to the already described procedure. The multi-harmonic SS model is acquired.

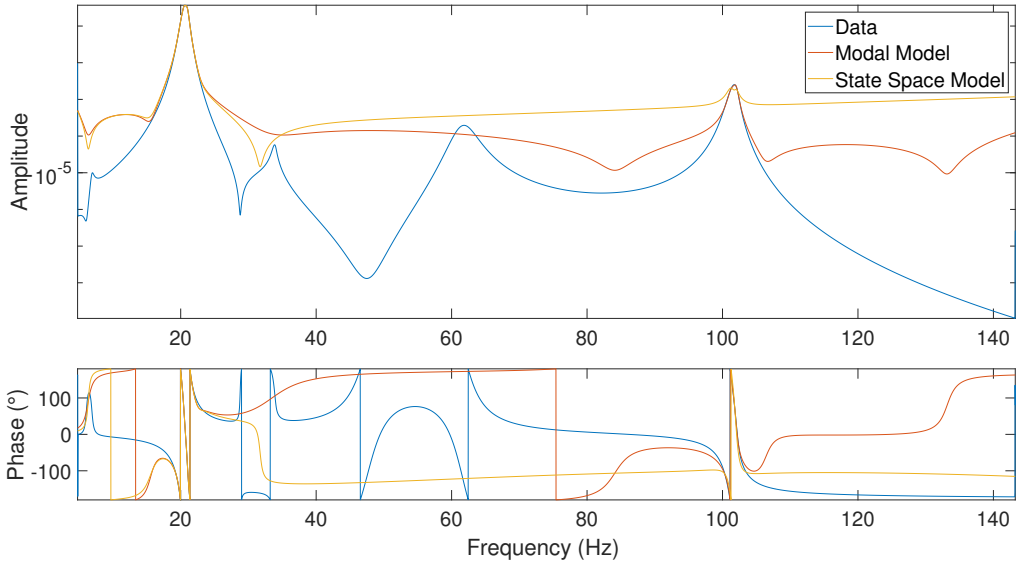

Figure 6.3: Modal synthesis after MLMM. Mode shifting operation is visible.

6.2.3 Multi-Harmonic State-Space Response Simulation

The computation of the simulated SS time responses is done according to the *lsim* MATLAB function. This function requires the respective aforementioned modal SS model and input force time series, the vector u of Equation 6.3. It also requires the time vector that guides the simulation. The latter is trivially equal for all simulations and its the same vector that guides the input force.

The input force time series given to the simulations is the non-orthodox aspect of this methodology. First, it is important to remark that nonlinear system responds at the frequency ω and also at its harmonics for a single-harmonic input at ω. Therefore, this multi-harmonic SS model should react in the same fashion, introducing a single-harmonic input at ω should provide a multi-harmonic time response. As previously stated, each harmonic order is its own SS model from which the time simulated responses of each order are calculated, summing up all these responses to this single-harmonic input must provide the desired outcome. However, the SS simulation is linear, introducing an input signal at frequency ω will always output a response at ω. It is easy to see how this becomes problematic for the higher orders, since the input force at ω will not lead to a response at $h\_order \times \omega$.

Therefore it is required that the input of the higher-orders simulations is manifested in its correct BW. The frequency of the input must be modified. In the case of simple constant spectrum inputs with a known frequency content, this modification is trivial. Otherwise, the input signal modification is done in a very similar fashion to the signal recreation of Equation 3.8a. For the simulation of a specific harmonic-order, the instantaneous Fourier coefficients of harmonic 1, or in-phase and quadrature components, previously retrieved from the initial MHDTF processing, are multiplied with Constant Output Level Amplitude (COLA) reference signals of the respective order, as in Equation 6.5, resulting in a signal with the same amplitude and phase content of the original harmonic 1 recreated signal, but at the desired multiple of

its frequency.

$$input\_force_h(t) = in - phase_1(t) \times \sin(h \times \omega \times t) + quadrature_1(t) \times \sin(h \times \omega \times t + 90°) \quad (6.5)$$

The obtained signal is used as input for the simulation of the h^{th} order SS model. After, the responses from each SS model, i.e. from each order, are summed respecting the initial relation between excitation frequency and response frequencies, leading to the desired multi-harmonic simulated response.

6.3 Application on a Simulated Lumped Parameter Model

The simulation system to be SS modelled refers to a 3 DOFs lumped parameter system, Figure 6.4, very similar to the system introduced in section 4.1. This time, the cubic spring is between the 2^{nd} and 3^{rd} mass. The structural parameters are also different, Table 6.1, and they were designed to have a strong higher-order harmonics response at the first mode.

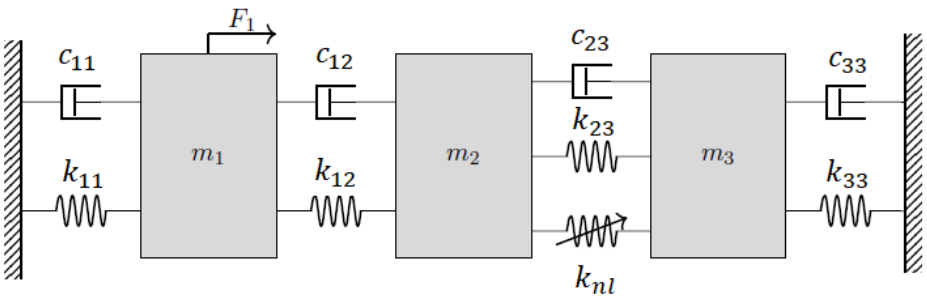

Figure 6.4: 3 DOF system, with cubic spring between mass 2 and 3.

Table 6.1: 3-DOFs system 2 parameters.

Mass(Kg)	Stiffness (N/m)	Nonlinear cubic stiffness (N/m^3)	Damping (Ns/m)
$m_1 = 10$	$k_{11} = 1.62 \times 10^4$	$k_{nl} = 1 \times 10^4$	$c_{11} = 30$
$m_2 = 1$	$k_{12} = 3 \times 10^4$		$c_{12} = 1$
$m_3 = 1$	$k_{23} = 1 \times 10^4$		$c_{23} = 1$
	$k_{33} = 1 \times 10^4$		$c_{33} = 1$

In order to obtain the time series of the response of the system, a 1000N constant amplitude logarithmic swept-sine input force, bandwidth of 10 rad/s to 300 rad/s, was applied at the 1^{st} mass. As done for the previous simulation a Newmark solver derived the acceleration response signals. These signals were processed using the MHDTF. Harmonics 1, 3 and 5 were tracked and the described procedure applied. The applied cut-off ratio was 15%, due to the disturbance free response.

The estimated MHDTF NLFRCs and the synthesised NLFRCs of the modal model and the modal SS model, for harmonics 1, 3 and 5 are plotted in Figure 6.5, 6.6 and 6.7, respectively. The fits are good for harmonic 1, due to its trivial behaviour.

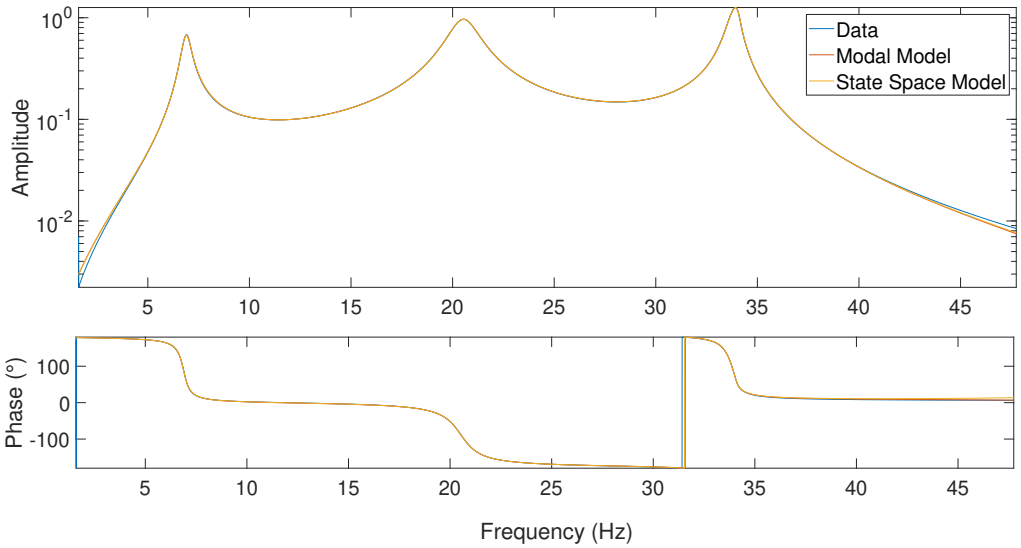

Figure 6.5: Harmonic 1 MHDTF estimation NLFRCs, juxtaposed with modal model and state-space model synthesised NLFRCs, for DOF3.

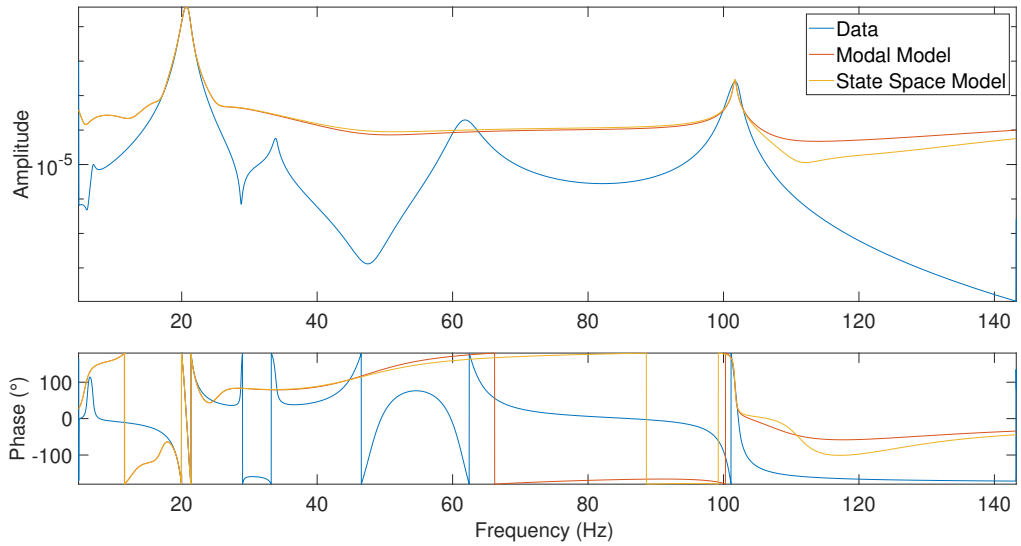

Figure 6.6: Harmonic 3 MHDTF estimation NLFRCs, juxtaposed with modal model and state-space model synthesised NLFRCs, for DOF3.

The fits of harmonics 3 and 5 are suboptimal. In the first and third modes of harmonic 3 the approximation is good. The same occurs for the first mode of harmonic 5. Since the contribution of the higher orders is only significant at these peaks, it is important that the fit at these is good. Additionally, small discrepancies are shown between the modal model and SS model. Moreover on harmonic 5, after the amplitude limit level of the harmonic mitigation, experienced at around -200dB, the turbulent amplitude levels were interfering with PolyMAX, therefore the estimations were leveled to pre-limit estimations.

After, the remaining procedure was applied. In this case of a simulation system, the input force is trivially modified since it is a known entity that was provided to the Newmark solver.

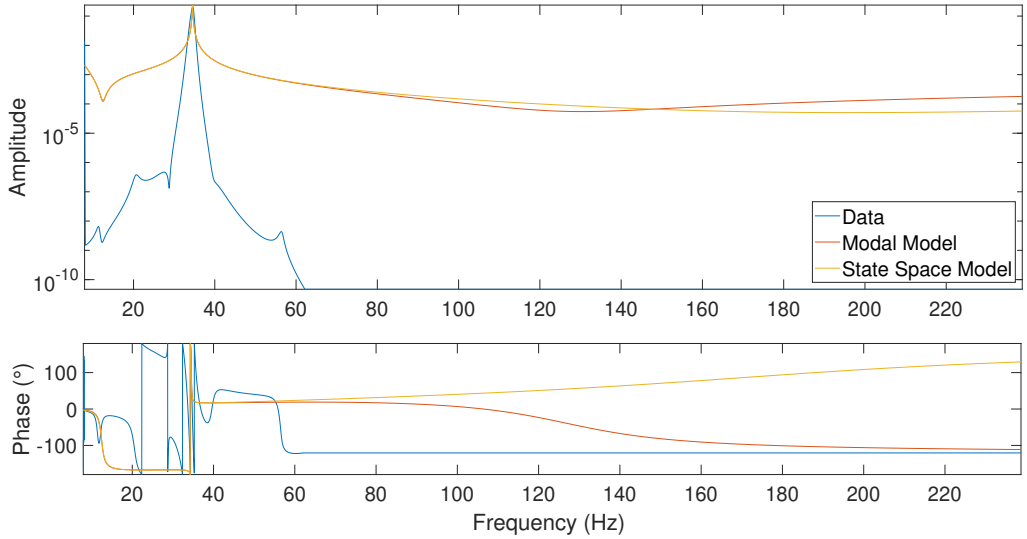

Figure 6.7: Harmonic 5 MHDTF estimation NLFRCs, juxtaposed with modal model and state-space model synthesised NLFRCs, for DOF3.

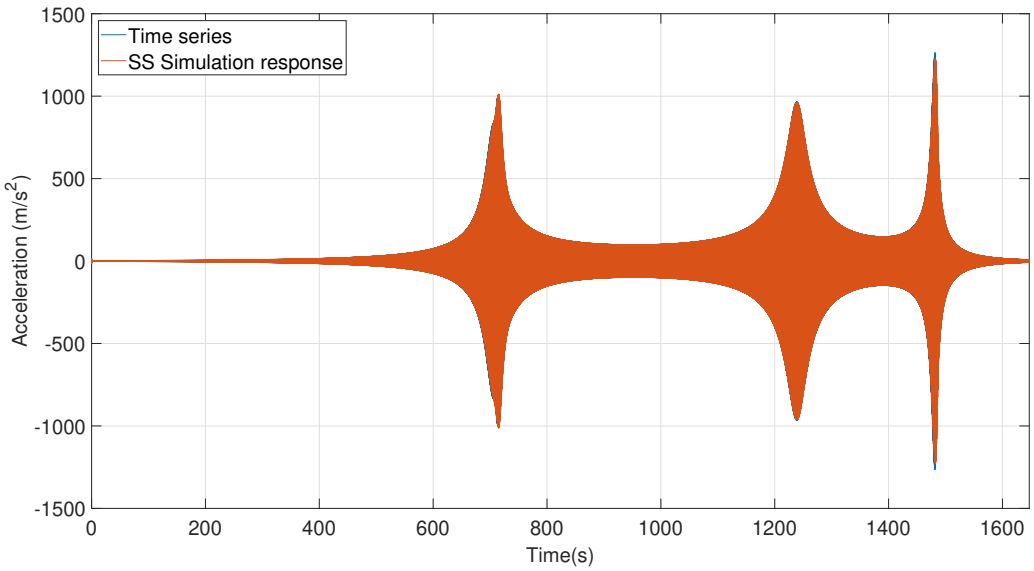

Figure 6.8: DOF3 Newmark response solution simulation contrasted with state-space simulation.

The SS simulated time response is contrasted with the Newmark solution time series, in Figure 6.8. However, since the contrast is not much noticeable, it is more convenient to plot the harmonic sum of the SS simulation response instead, Figure 6.9. As visible, the simulated model presents acceptable results, there is a noticeable correlation between the harmonic sum and the Newmark time series. However, at

modes 1 and 3, there is a slight shift in the response and underestimation. The modelling error in only considering the 1^{st} harmonic is hence very clear, by the comparison of harmonic sum and harmonic 1 amplitudes.

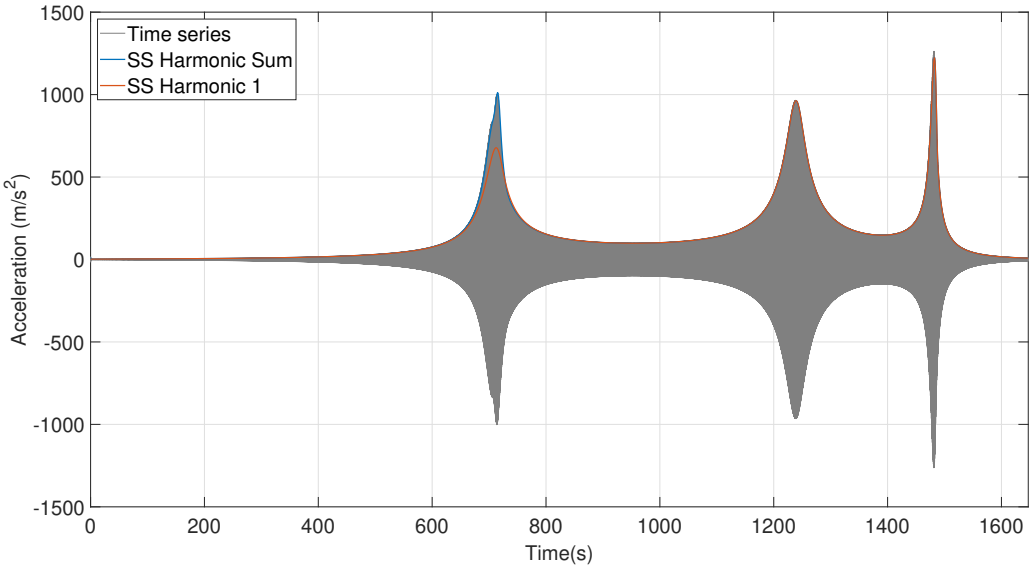

Figure 6.9: DOF3 Newmark response solution simulation contrasted with state-space simulation harmonic sum and harmonic 1.

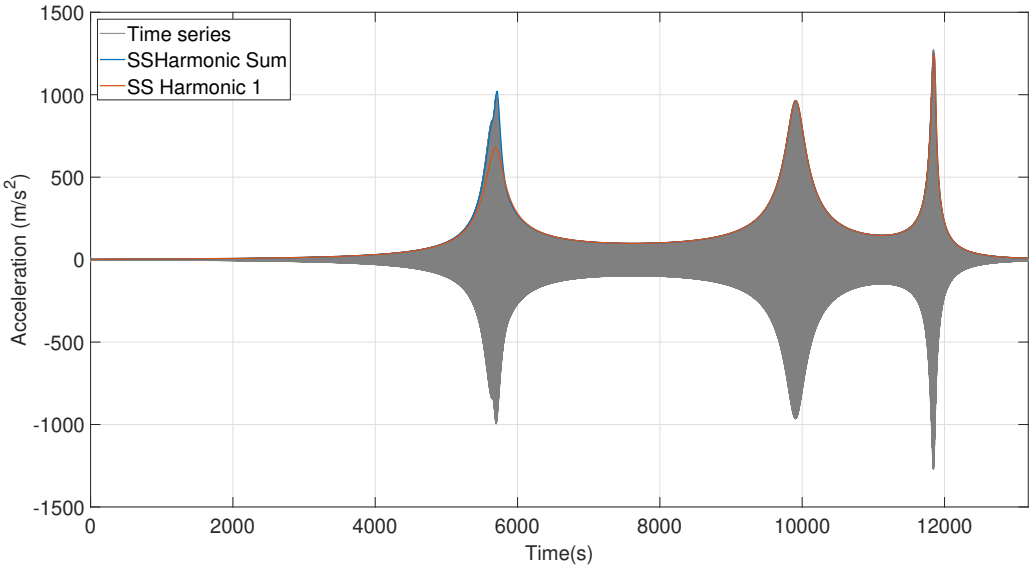

Figure 6.10: DOF3 Newmark response solution simulation contrasted with state-space simulation harmonic sum and harmonic 1, for lower sweep rate.

Additionally, due to the ease of creating simulation data with the Newmark solver, an investigation on the model adaptability to different conditions than the ones who originated it can be made. Consequently, to

the already created multi-harmonic SS model was applied two different forces, one with a lower sweep rate and one with a 10% force increase. The comparison is then made with the Newmark solution for the different conditions. As seen in Figure 6.10, a slower sweep rate of the excitation provided an identical comparison as the original sweep rate. For the 10% force increase, Figure 6.11, the SS could not keep up with the strong nonlinear increase in amplitude of nonlinear systems, the simulated response is underestimated in every mode.

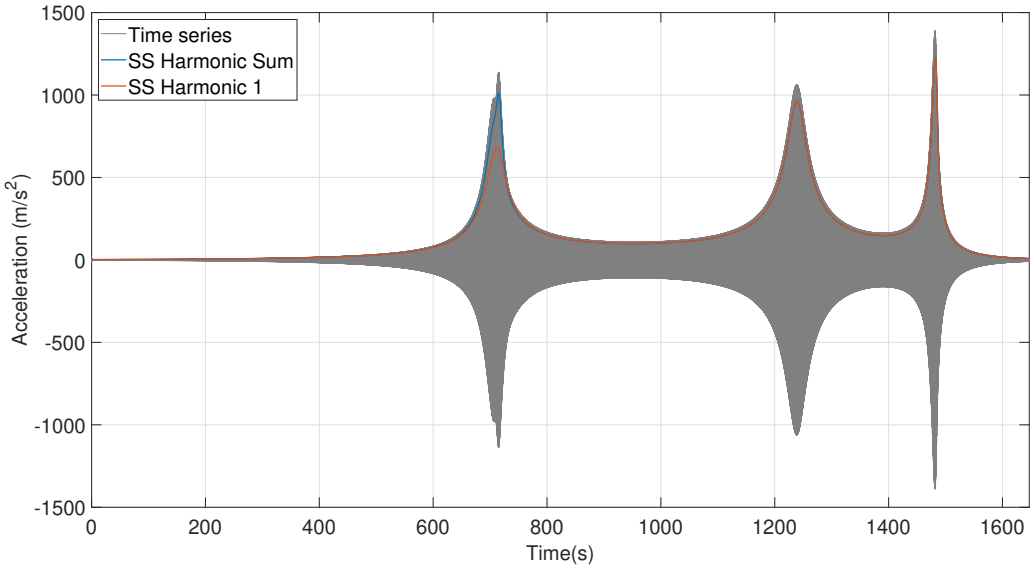

Figure 6.11: DOF3 Newmark response solution simulation contrasted with state-space simulation harmonic sum and harmonic 1, for 10% force increase.

6.4 Application on a Demo Airplane Experimental Setup

The experimental setup to be modelled is the same as discussed in chapter 5, where it was shown to present a strong harmonic 2 and 3 contribution. Again, for ease of processing, only the wing and pylons DOFs were considered.

The procedure starts with the measured signals MHDTF processing. For this application, a 5% cut-off ratio was prioritized to ensure high-quality NLFRCs. From the estimated MHDTF NLFRCs, the synthesised NLFRCs of the modal model and the SS model, for harmonics 1, 2 and 3 were constructed. They are plotted in Figure 6.12, 6.13 and 6.14, particular to the LWing1/LWing Force.

Regarding harmonic 1, the fit is overall adequate. Harmonics 2 and 3 as well, specially when comparing to the fits of the higher-orders of the simulatied system in Figure 6.6 and Figure 6.7. In this comparison, the experimental model has the advantage of having a strong higher-order contribution that facilitates PolyMAX's work. However, the model fit is not good when disturbances are present in the NLFRC: in the 10Hz to 60Hz range of harmonic 2 and 15Hz to 90Hz for harmonic 3. It fails to predict the system

underlined in the noise. Additionally, the wing DOFs fit is better comparing to the pylon DOFs, since the NLFRCs estimations of the first, Figure 5.7 are clearer when comparing to the latter, Figure 5.6.

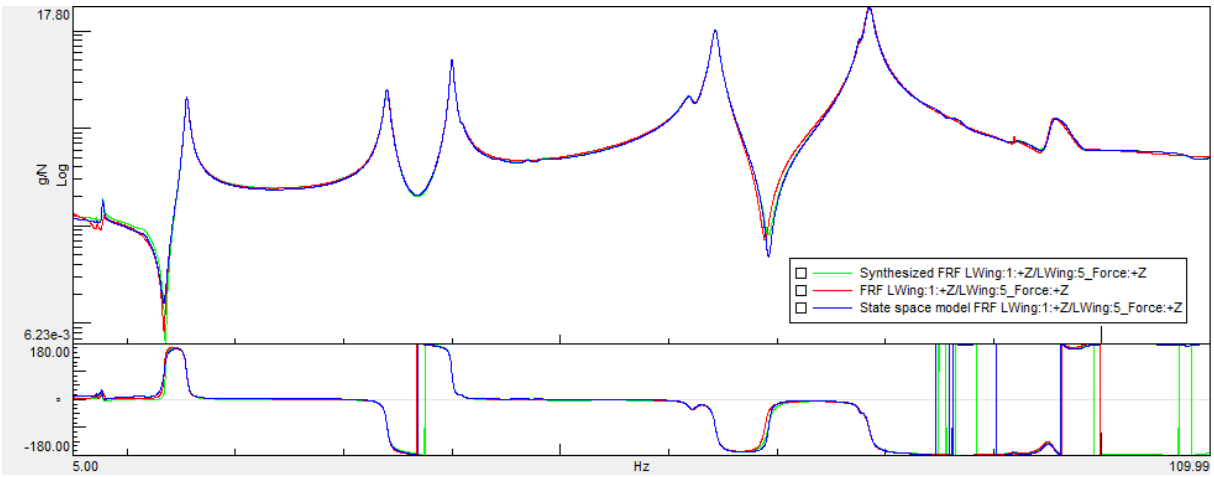

Figure 6.12: Harmonic 1 MHDTF estimation NLFRCs (red), juxtaposed with modal model (green) and state-space model (blue) synthesised NLFRCs, for LWing1/LWing Force.

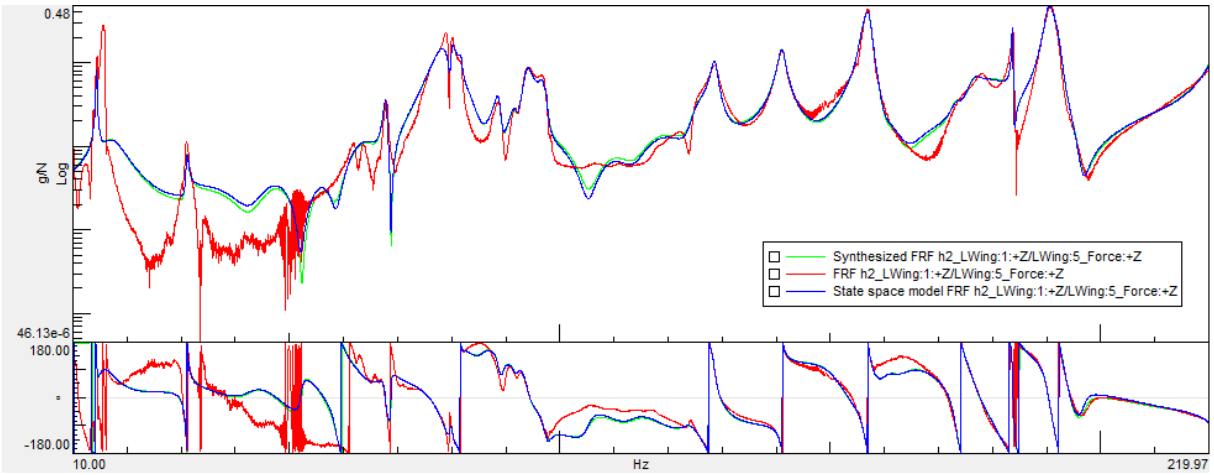

Figure 6.13: Harmonic 2 MHDTF estimation NLFRCs (red), juxtaposed with modal model (green) and state-space model synthesised NLFRCs, for LWing1/LWing Force.

The simulated time series are calculated following the remaining procedure, with the input force modification as detailed for the higher orders.

The harmonic sum and harmonic 1 amplitudes of the SS simulated time response are contrasted with the measured time series in Figure 6.15 and 6.16. It is possible to see, not only the accuracy of the SS model, by comparing the time series with the harmonic sum, but also the improvement of including higher-order harmonics in the model by comparing the harmonic sum and the harmonic 1 amplitudes. In

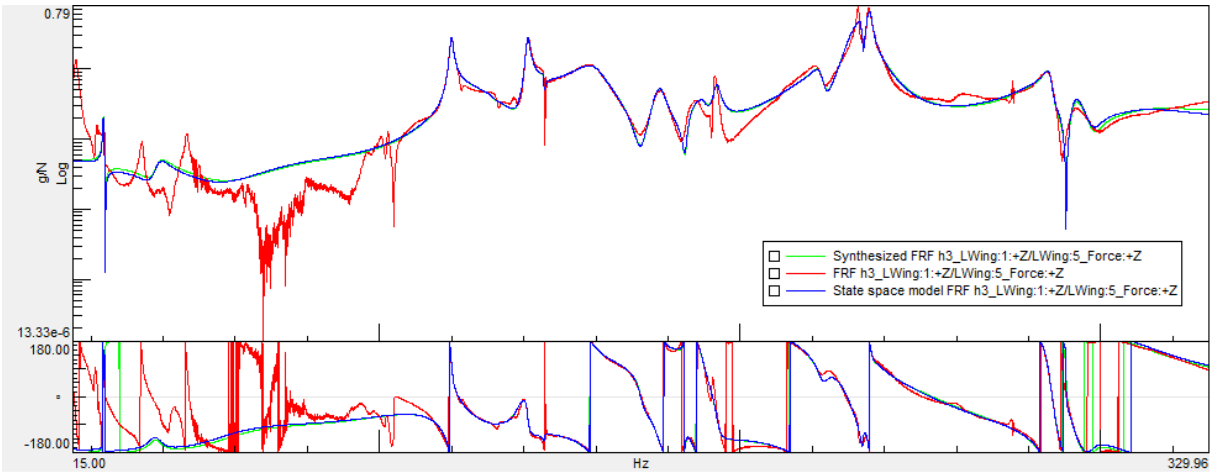

Figure 6.14: Harmonic 3 MHDTF estimation NLFRCs (red), juxtaposed with modal model (green) and state-space model (blue) synthesised NLFRCs, for LWing1/LWing Force.

general, the wing DOFs presented a greater prediction overall when comparing to the pylon DOFs. This is observed at 480s in Figure 6.16, the simulated amplitude underestimates the actual response and if not for the multi-harmonic inclusion it would only be worse. This comes at no surprise since the fits of the pylon DOFs were poor. The reason may be the overall complexity of the behaviour of the pylon, as visualized by comparing Figure 5.7 and Figure 5.6. Nevertheless, even for experimental measurements, that present strong nonlinear effects and disturbances in the signal, this technique achieved a numerical prediction with adequate results that satisfactorily improved with the inclusion of higher-order harmonics in the model.

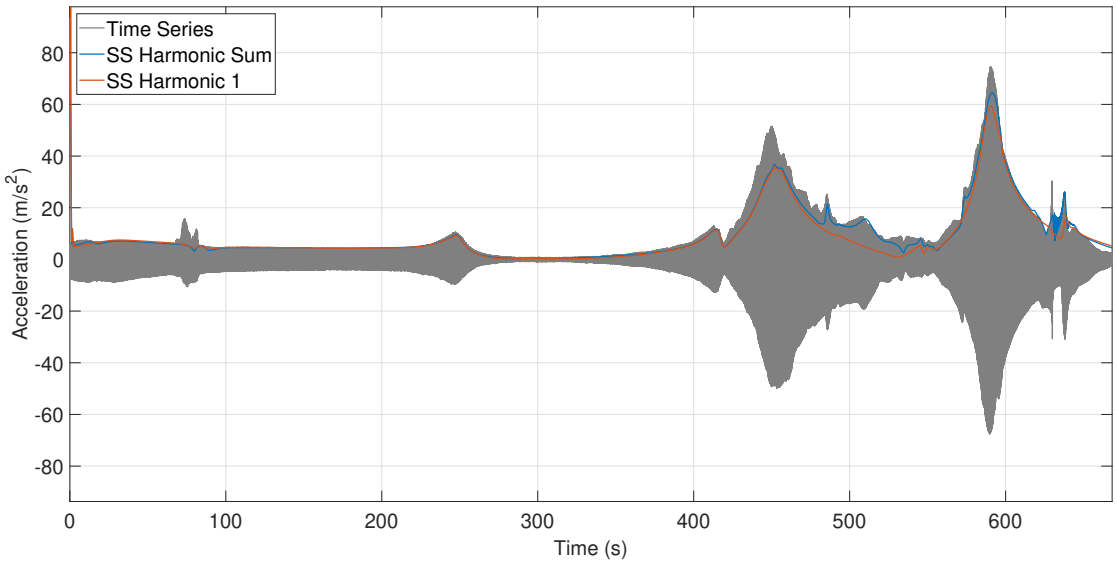

Figure 6.15: LWing6, sweep 1 measured response contrasted with state-space simulation harmonic sum and harmonic 1 amplitudes.

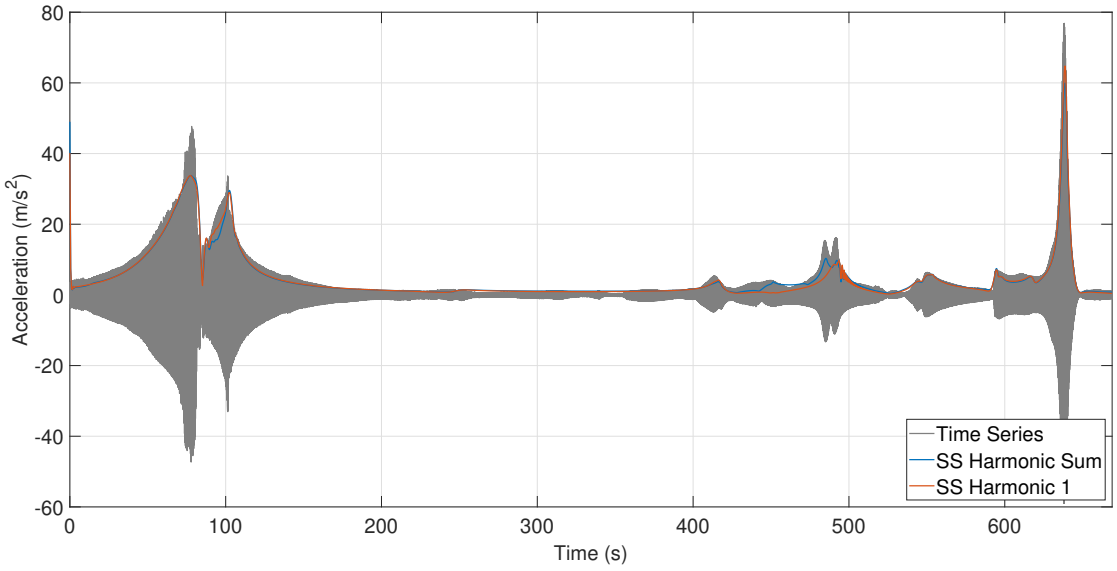

Figure 6.16: LPyl2, sweep 2 measured response contrasted with state-space simulation harmonic sum and harmonic 1 amplitudes.

Chapter 7

Conclusions and Future Work

As indicated in chapter 1, the main objective of this dissertation was to extend the DTF procedure to nonlinear structures, thus estimating the amplitude and phase of a measured response not only for its fundamental harmonic but also for the higher-orders. Additionally, it is also an objective to explore the capabilities of the multi-harmonic contributions, provided by the MHDTF, on the nonlinear system identification field.

7.1 Conclusions and Achievements

The principal objective of developing a procedure able to perform, with particular emphases to offline processing, multi-harmonic identification of nonlinear responses was achieved, and to an extent, successfully so. The main validation comes from the comparison with the numerical computation results of the HB method, Figure 4.15. In this context, several implementations of the procedure contributed to the identifications and validation observed, namely, the acausal filtering, with the use of the *filtfilt* function, to assure zero phase filtering and the correct relation between the estimations and the time/frequency that they occur at, as realized in Figure 3.13. Harmonic interference mitigation also played a big roll on the simulation results, reducing the impact that the harmonics may have with each other when the amplitude difference is significant. The impact of this stage is visualized by comparing Figure 4.7 and Figure 4.8, as without it, validation is only possible up to the vicinity of -100 dB amplitude level. This stage, however, is disused in the presence of signal disturbances, associated with experimental testing.

These are also the main contributors for the better results obtained when comparing to the ones of the adaptive filter for simulation data, Figure 4.13 and Figure 4.14. Moreover on this comparison, processing experimental data corrupted by nonlinearity and noise with both methods, Figure 5.11, confirmed the very good suitability of the MHDTF to reject noise disturbances, as its precursor, the single-harmonic DTF, already suggested.

The MHDFT is also presented as a technique with good flexibility, depending on user preference. The

influence of the cut-off ratio presents a clear compromise: either tracking accuracy or efficient noise rejection, as interpreted in subsection 5.2.1.

The development of a multi-harmonic state-space modelling procedure was also one of the challenges for this dissertation. Possible due to the estimations of the MHDTF, it was shown that there is clear improvement by considering the higher-orders contributions, partially achieving the proposed goal as its accuracy is only at the level of excitation used during the identification, due to the underlying linearisation.

7.2 Future Work

Future developments on the MHDTF should focus on the lowpass filtering stage. In the end, this is where the good disturbance attenuation capabilities of this technique originate from. The employment of a variable BW lowpass filter, instead of the discrete implementation in this work, will lead to decreased CPU times. As a consequence, the interference indicator will need adaptation.

Additionally, the MHDTF identification of sub-harmonics was not explored in this dissertation. The already developed should be able to track these responses, however, it is expected that they may suffer more heavily from harmonic interference.

To improve the multi-harmonic SS model prediction, the use of Polymax and MLMM to obtain a good fit of the higher-order NLFRC should be further investigated. However, the underlying linearisation does not allow to obtain a good model behaviour at arbitrary excitation amplitudes. To overcome this limitation, the model in Equation 6.3 should include additional terms to account for the nonlinearity. This has similarly be done by Paduart et al. [40], where two additional terms represent the relation between state and outputs with the nonlinearity. The cited approach is based on the use of a periodic pseudorandom excitation with the Best Linear Approximation (BLA) framework. The novelty of this approach would then be the use of a swept-sine excitation together with the MHDTF, that maintain a deterministic relation between excitation and response frequencies. The applicability of this approach is however yet to be verified.

Bibliography

[1] U. Musella, E. Faignet, B. Peeters, and P. Guillaume. Digital tracking techniques for mimo swept sine control testing. In *Proceedings of International Conference on Noise and Vibration Engineering (ISMA)*, Leuven, Belgium, 2020.

[2] G. Kerschen, K. Worden, A. F. Vakakis, and J.-C. Golinval. Past, present and future of nonlinear system identification in structural dynamics. *Mechanical Systems and Signal Processing*, 20(3): 505–592, 2006. doi:10.1016/j.ymssp.2005.04.008.

[3] J. Noël and G. Kerschen. Nonlinear system identification in structural dynamics: 10 more years of progress. *Mechanical Systems and Signal Processing*, 83:2–35, 2017. doi:10.1016/j.ymssp.2016.07.020.

[4] R. J. Allemang, D. L. Brown, and R. W. Rost. Experimental modal analysis and dynamic component synthesis. *Measurement Techniques for Experimental Modal Analysis*, 2, Dec. 1987.

[5] M. Simon and G. R. Tomlinson. Use of the Hilbert transform in modal analysis of linear and non-linear structures. *Journal of Sound and Vibration*, 96(4):421–436, Oct. 1984. doi:10.1016/0022-460X(84)90630-8.

[6] T. K. Caughey. Random excitation of a system with bilinear hysteresis. *Journal of Applied Mechanics*, 27:649–652, 1960.

[7] J. Roberts and P. Spanos. *Random Vibrations and Statistical Linearization*. Wiley, 1990.

[8] S. F. Masri and T. K. Caughey. A nonparametric identification technique for nonlinear dynamic problems. *Journal of Applied Mechanics*, 46:433–447, 1979. doi:10.1115/1.3424568.

[9] I. J. Leontaritis and S. A. Billings. Input-output parametric models for non-linear systems, Part I: Deterministic non-linear systems. *International Journal of Control*, 41(2):303–328, 1985. doi:10.1080/0020718508961129.

[10] I. J. Leontaritis and S. A. Billings. Input-output parametric models for non-linear systems Part II: Stochastic non-linear systems. *International Journal of Control*, 41(2):329–344, 1985. doi:10.1080/0020718508961130.

[11] M. Schetzen. *The Volterra and Wiener Theories of Nonlinear Systems*. Krieger, 1980.

[12] H. Rice and J. Fitzpatrick. A generalised technique for spectral analysis of non-linear systems. *Mechanical Systems and Signal Processing*, 2(2):195–207, 1988. doi:10.1016/0888-3270(88)90043-X.

[13] R. Porwal and N. Vyas. Nonlinear damping estimation of self-excited system using wavelet transform. In *Proceedings of the 27th International Modal Analysis Conference (IMAC)*, Orlando, FL, USA, 2009.

[14] M. Feldman. *Hilbert Transform Applications in Mechanical Vibration*. Wiley, 2011. doi:10.1002/9781119991656.

[15] W. Heylen, S. Lammens, and P. Sas. *Modal Analysis Theory and Testing*. Katholieke Universteit Leuven, Departement Werktuigkunde, Leuven, Sept. 2005.

[16] S. Vettori, E. D. Lorenzo, B. Peeters, and A. Carcaterra. Development and validation of data processing techniques for aircraft ground vibration testing. In M. L. Mains and B. J. Dilworth, editors, *Topics in Modal Analysis & Testing, Volume 8*, pages 225–236. Springer International Publishing, 2020.

[17] G. Kerschen, M. Peeters, J. Golinval, and A. Vakakis. Nonlinear normal modes, Part I: A useful framework for the structural dynamicist. *Mechanical Systems and Signal Processing*, 23(1):170–194, 2009. doi:10.1016/j.ymssp.2008.04.002.

[18] R. M. Rosenberg. Normal Modes of Nonlinear Dual-Mode Systems. *Journal of Applied Mechanics*, 27(2):263–268, Jun. 1960. doi:10.1115/1.3643948.

[19] R. M. Rosenberg. The normal modes of nonlinear n-degree-of-freedom systems. *Journal of Applied Mechanics*, 29(1):7–14, 1962. doi:10.1115/1.3636501.

[20] S. Shaw and C. Pierre. Non-linear normal modes and invariant manifolds. *Journal of Sound and Vibration*, 150(1):170–173, 1991. doi:10.1016/0022-460X(91)90412-D.

[21] G. Gloth and M. Sinapius. Analysis of swept-sine runs during modal identification. *Mechanical Systems and Signal Processing*, 18(6):1421–1441, 2004. doi:10.1016/S0888-3270(03)00087-6.

[22] T. Detroux, L. Renson, L. Masset, and G. Kerschen. The harmonic balance method for bifurcation analysis of large-scale nonlinear mechanical systems. *Computer Methods in Applied Mechanics and Engineering*, 296:18–38, Nov. 2015. doi:10.1016/j.cma.2015.07.017.

[23] T. M. Cameron and J. H. Griffin. An Alternating Frequency/Time Domain Method for Calculating the Steady-State Response of Nonlinear Dynamic Systems. *Journal of Applied Mechanics*, 56(1): 149–154, Mar. 1989. doi:10.1115/1.3176036.

[24] G. Xie and J. Y. Lou. Alternating frequency/coefficient (AFC) technique in the trigonometric collocation method. *International Journal of Non-Linear Mechanics*, 31(4):531–545, 1996. doi: doi:10.1016/0020-7462(96)00003-0.

[25] L. Tan and J. Jiang. Chapter 1 - Introduction to Digital Signal Processing. In *Digital Signal Processing*, pages 1–12. Academic Press, 3^{rd} edition, 2019. doi:10.1016/B978-0-12-815071-9.00001-4.

[26] L. Tan and J. Jiang. Chapter 2 - Signal Sampling and Quantization. In *Digital Signal Processing*, pages 13–58. Academic Press, 3^{rd} edition, 2019. doi:10.1016/B978-0-12-815071-9.00002-6.

[27] L. Tan and J. Jiang. Chapter 6 - Digital Signal Processing Systems, Basic Filtering Types, and Digital Filter Realizations. In *Digital Signal Processing*, pages 173–228. Academic Press, e edition, 2019. doi:10.1016/B978-0-12-815071-9.00006-3.

[28] J. O. Smith. *Introduction to Digital Filters with Audio Applications*. W3K Publishing, 2007.

[29] Zurich Instruments. Principles of lock-in detection and the state of the art. White Paper, Nov. 2016.

[30] R. All. *Digital Filters For Everyone*. Creative Arts & Sciences House, 3^{rd} edition, Mar. 2015.

[31] J. Moorer. The Manifold Joys of Conformal Mapping: Applications to Digital Filtering in the Studio. *Journal of the Audio Engineering Society*, 31(11):826–841, Nov. 1983.

[32] P. Nali, , and A. Bettacchioli. Beating phenomena in spacecraft sine testing and an attempt to include the sine sweep rate effect in the test-prediction. *Advances in Aircraft and Spacecraft Science*, pages 197–209, 2016. doi:10.12989/aas.2016.3.2.197.

[33] G. Abeloos, L. Renson, C. Collette, and G. Kerschen. Stepped and swept control-based continuation using adaptive filtering. *Nonlinear Dynamics 104*, 2021. doi: https://doi.org/10.1007/s11071-021-06506-z.

[34] S. Haykin and B. Widrow. *Least-Mean-Square Adaptive Filters*. Wiley, Sept. 2003.

[35] B. Peeters, H. V. der Auweraer, P. Guillaume, and JanLeuridan. The polymax frequency-domain method: A new standard for modal parameter estimation? *Shock and Vibration*, 11:395–409, Jan. 2004. doi:10.1155/2004/523692.

[36] P. Schaldenbrand. *Getting Started with Modal Curvefitting*. Siemens Digital Industries Software, https://community.sw.siemens.com/s/article/getting-started-with-modal-curvefitting, Sept. 2020. (Accessed on 02/10/2022).

[37] M. El-kafafy, G. Accardo, B. Peeters, K. Janssens, T. De Troyer, and P. Guillaume. A Fast Maximum Likelihood-Based Estimation of a Modal Model. In M. Mains, editor, *Topics in Modal Analysis, Volume 10*, pages 133–156, Cham, 2015. Springer International Publishing. doi:10.1007/978-3-319-15251-6_15.

[38] P. Schaldenbrand. *Maximum Likelihood estimation of a Modal Model (MLMM)*. Siemens Digital Industries Software, https://community.sw.siemens.com/s/article/maximum-likelihood-estimation-of-a-modal-model-mlmm, Sept. 2020. (Accessed on 02/10/2022).

[39] M. Elkafafy and B. Peeters. Robust Identification of Stable MIMO Modal State Space Models. In B. J. Dilworth, T. Marinone, and M. Mains, editors, *Topics in Modal Analysis & Parameter Identifica-*

tion, Volume 8, pages 81–95, Cham, 2023. Springer International Publishing. doi:10.1007/978-3-031-05445-7_10.

[40] J. Paduart, L. Lauwers, J. Swevers, K. Smolders, J. Schoukens, and R. Pintelon. Identification of nonlinear systems using Polynomial Nonlinear State Space models. *Automatica*, 46(4):647–656, 2010. doi:10.1016/j.automatica.2010.01.001.

Appendix A

MATLAB code

A.1 Multi-Harmonic Digital Tracking Filter

A.1.1 Without Harmonic Interference Mitigation

```
% MULTI-HARMONIC DIGITAL TRACKING FILTER - EDUARDO SOUSA 2022
%
% MHDTF script, without interference mitigation
% considering the signal to be tracked as x

%% SIGNAL VARIABLES

sweepmode = 'logarithmic';
f_start = 1;   % signal start frequency,  in Hz
f_end = 10;    % signal end frequency, in Hz
T = 10;        % signal period
fs = 1000;     % sample frequency

time_vec = linspace(0, T, T*fs); % time vector

%% USER DEFINED DTF SETTINGS

h_sel = [1 2 3];          % selection of the harmonics to track
N = 10;                   % number of sub-intervals, N = 1 for constant cut-off frequency
cut_off_ratio = 0.15;     % cut-off frequency ratio
interval_splitting = 1;   % 0 - sample/time based , 1 - frequency based
filter_order = 4;         % butterworth filter order, advised to remain always 4

%% COMPUTATION VARIABLES

nh = length(h_sel);             % number of harmonics
n_samples = length(time_vec);       % number of samples
```

```
28
29  aux1 = zeros(1,N); % sample location of sub-interval start
30  aux2 = zeros(1,N); % sample location of sub-interval end
31  switch sweepmode
32      case char('linear')
33          f_vec = linspace(f_start,f_end,n_samples);
34          S = (2*pi)*(f_end - f_start)/T;   % linear sweep rate
35          aux1(1,:) = 1+round((0:N-1)*n_samples/N);
36      case char('logarithmic')
37          f_vec = logspace(log10(f_start),log10(f_end),n_samples);
38          S = (60/T)*log2(f_end/f_start);   % logarithmic sweep rate, in octaves per minute
39          switch interval_splitting
40              case 0
41                  aux1(1,:) = 1+round((0:N-1)*n_samples/N);
42              case 1
43                  aux1 = 1 + round(log2((0:N-1)/(N)*(f_end/f_start - 1) + ...
                        1)/log2(f_end/f_start)*(n_samples));
44          end
45  end
46  aux2 = aux1(1,2:end) - 1; aux2(N) = n_samples;
47
48  % COLA reference signals
49  sin_cola = zeros(nh,n_samples); cos_cola = zeros(nh,n_samples);
50  for h_id = 1:nh
51      sin_cola(h_id,:) = chirp(time_vec,h_sel(h_id)*f_start,T,h_sel(h_id)*f_end,sweepmode,-90);
52      cos_cola(h_id,:) = chirp(time_vec,h_sel(h_id)*f_start,T,h_sel(h_id)*f_end,sweepmode);
53  end
54
55  %% VECTOR/MATRIX PREALLOCATION
56
57  in_phase = zeros(nh, n_samples);  % in-phase component
58  quad = zeros(nh, n_samples);      % quadrature component
59
60  rec = zeros(1,n_samples);       % recreated signal
61
62  %% MULTI DUAL PHASE HOMODYNING (MIXING)
63
64  mix_sin = x.*sin_cola;
65  mix_cos = x.*cos_cola;
66
67  %% FILTERING LOOP
68
69  for h_id = 1:nh       % h_id - harmonic identifier of the interference row
70      for n = 1:N
71          [b,a] = butter(filter_order,h_sel(h_id)*cut_off_ratio*f_vec(aux1(n))/(fs/2));
72          aux_early = aux1(n) - 250000;
73          aux_late = aux2(n) + 250000;
74
75          if aux_early < 1 || n == 1; aux_early = 1; end
```

```
76          if aux_late > n_samples || n == N; aux_late = n_samples; end
77
78          filter_aux1 = filtfilt(b,a,squeeze(mix_sin(h_id, aux_early:aux_late)));
79          filter_aux2 = filtfilt(b,a,squeeze(mix_cos(h_id, aux_early:aux_late)));
80
81          in_phase(h_id,aux1(n):aux2(n)) = ...
                2*filter_aux1((aux1(n)-aux_early+1):(aux2(n)-aux_early+1));
82          quad(h_id,aux1(n):aux2(n)) = ...
                2*filter_aux2((aux1(n)-aux_early+1):(aux2(n)-aux_early+1));
83      end
84  end
85
86  %% AMPLITUDE AND PHASE ESTIMATION
87  x_amp = sqrt(quad.^2 + in_phase.^2);
88  x_phase = atan2(quad, in_phase);
89
90  %% SIGNAL RECREATION
91  for h_id = 1:nh
92      rec = rec + in_phase(h_id,:).*sin_cola(h_id,:) + quad(h_id,:).*cos_cola(h_id,:);
93  end
```

A.1.2 With Harmonic Interference Mitigation

```
1  % MULTI-HARMONIC DIGITAL TRACKING FILTER - EDUARDO SOUSA 2022
2  %
3  % MHDTF script, with or without interference mitigation
4  % considering the signal to be tracked as x
5
6  %% SIGNAL VARIABLES
7
8  sweepmode = 'logarithmic';
9  f_start = 1;    % signal start frequency,  in Hz
10 f_end = 10;     % signal end frequency, in Hz
11 T = 10;         % signal period
12 fs = 1000;      % sample frequency
13
14 time_vec = linspace(0, T, T*fs); % time vector
15
16 %% USER DEFINED MHDTF SETTINGS
17
18 h_sel = [1 2 3];         % selection of the harmonics to track
19 N = 4;                   % number of intervals, N = 1 for constant cut-off frequency
20 mitigation = 1;          % 1 = with interference mitigation, 2 = no mitigation
21 cut_off_ratio = 0.15;    % cut-off frequency ratio
22 leap_detection = 5;      % jump detection sensivity, in dB
23 leap_percentage = 0.3;   % percentage of jumps per interval number "allowed" before ...
       disregarding
24 interval_splitting = 1; % 0 - sample/time based , 1 - frequency based
```

```
filter_order = 4;       % butterworth filter order, advised to remain always 4

%% COMPUTATION VARIABLES

nh = length(h_sel);      % number of harmonics
n_samples = length(x);   % number of samples

aux1 = zeros(1,N); % sample location of sub-interval start
aux2 = zeros(1,N); % sample location of sub-interval end
switch sweepmode
    case char('linear')
        f_vec = linspace(f_start,f_end,n_samples);
        S = (2*pi)*(f_end - f_start)/T;   % linear sweep rate
        aux1(1,:) = 1+round((0:N-1)*n_samples/N);
    case char('logarithmic')
        f_vec = logspace(log10(f_start),log10(f_end),n_samples);
        S = (60/T)*log2(f_end/f_start);   % logarithmic sweep rate, in octaves per minute
        switch interval_splitting
            case 0
                aux1(1,:) = 1+round((0:N-1)*n_samples/N);
            case 1
                aux1 = 1 + round(log2((0:N-1)/(N)*(f_end/f_start - 1) + ...
                    1)/log2(f_end/f_start)*(n_samples));
        end
end
aux2 = aux1(1,2:end) - 1; aux2(N) = n_samples;

if mitigation == 2; int_m = 1:nh;  % interference matrix
else
    int_m = ones(factorial(nh-1), nh); int_m(:,2:end) = perms(setdiff(1:nh,1));
end

% COLA reference signals
sin_cola = zeros(nh,n_samples); cos_cola = zeros(nh,n_samples);
for h_id = 1:nh
    sin_cola(h_id,:) = chirp(time_vec,h_sel(h_id)*f_start,T,h_sel(h_id)*f_end,sweepmode,-90);
    cos_cola(h_id,:) = chirp(time_vec,h_sel(h_id)*f_start,T,h_sel(h_id)*f_end,sweepmode);
end

%% VECTOR/MATRIX PREALLOCATION

int_vec_valid = ones(1,size(int_m,1)); % interference vector validation
% 0 - presence of jumps in the vector / 1 - everything fine

h_valid = mitigation.*ones(1,nh);      % harmonic validation
% 0 - presence of jumps / 1 - normal state / 2 - interference caused by this harmonic is ...
    already mitigated

in_phase = zeros(nh, n_samples);       % in-phase component
```

```
72  quad = zeros(nh, n_samples);           % quadrature component
73
74  rec = zeros(1,n_samples);              % recreated signal
75
76  %% MULTI DUAL-PHASE HOMODYNING (MIXING)
77
78  mix_sin = x.*sin_cola;
79  mix_cos = x.*cos_cola;
80
81  %% LOWPASS FILTERING AND HARMONIC INTERFERENCE MITIGATION LOOP
82
83  for int_m_id = 1:size(int_m,1)  % int_m_id = interference row from interference matrix
84      for vec_id = 1:nh           % vec_id = vector identifier of the interference row
85
86          curr_h = int_m(int_m_id, vec_id);
87          if  int_vec_valid(int_m_id) == 0
88              continue
89          end
90          for n = 1:N
91              [b,a] = butter(filter_order,h_sel(curr_h)*cut_off_ratio*f_vec(aux1(n))/(fs/2));
92              aux_early = aux1(n) - 250000;
93              aux_late = aux2(n) + 250000;
94
95              if aux_early < 1 || n == 1; aux_early = 1; end
96              if aux_late > n_samples || n == N; aux_late = n_samples; end
97
98              filter_aux1 = filtfilt(b,a,squeeze(mix_sin(curr_h, aux_early:aux_late)));
99              filter_aux2 = filtfilt(b,a,squeeze(mix_cos(curr_h, aux_early:aux_late)));
100
101             in_phase(curr_h,aux1(n):aux2(n)) = ...
                    2*filter_aux1((aux1(n)-aux_early+1):(aux2(n)-aux_early+1));
102             quad(curr_h,aux1(n):aux2(n)) = ...
                    2*filter_aux2((aux1(n)-aux_early+1):(aux2(n)-aux_early+1));
103         end
104
105         if vec_id == nh || h_valid(curr_h) == 2
106             continue
107         end
108
109         % interference indicator
110         h_valid(curr_h) = interference_indicator(leap_detection, leap_percentage, ...
111             (in_phase(curr_h,aux1(2:end))), (in_phase(curr_h,aux1(2:end) - 1)),  ...
112             (quad(curr_h,aux1(2:end))), (quad(curr_h,aux1(2:end) - 1))) ;
113
114         if h_valid(curr_h) == 0
115             int_vec_valid(int_m_id) = 0;
116             continue
117         end
118
```

```
        % recreated single harmonic signal
        rec_harm = in_phase(curr_h,:).*sin_cola(curr_h,:) + ...
            quad(curr_h,:).*cos_cola(curr_h,:);

        %interference mitigation
        for vec_id_int = (vec_id+1):nh
            mix_sin(int_m(int_m_id, vec_id_int),:) = squeeze(mix_sin(int_m(int_m_id, ...
                vec_id_int),:)) - rec_harm.*sin_cola(int_m(int_m_id, vec_id_int),:);
            mix_cos(int_m(int_m_id, vec_id_int),:) = squeeze(mix_cos(int_m(int_m_id, ...
                vec_id_int),:)) - rec_harm.*cos_cola(int_m(int_m_id, vec_id_int),:);
        end
        h_valid(curr_h) = 2;
    end
end

%% AMPLITUDE AND PHASE EXTRACTION

x_amp = sqrt(quad.^2 + in_phase.^2);
x_phase = atan2(quad, in_phase);

%% SIGNAL RECREATION
for h_id = 1:nh
    rec = rec + in_phase(h_id,:).*sin_cola(h_id,:) + quad(h_id,:).*cos_cola(h_id,:);
end
```

A.2 Harmonic Interference Indicator

```
% INTERFERENCE INDICATOR - EDUARDO SOUSA 2022
%
% function that checks if the corresponding harmonic is composed of
% interference (valid = 0) or not (valid = 1)
%
% inputs:
%   leap_detection - leap height, expressed in dB
%   leap_percentage - percentage of jumps, per number of N-1, required for invalidation
%   in_phase1, in_phase2 - in_phase component before and at each interval start
%   quad1, quad2 - quadrature component before and at each interval start

function valid = interference_indicator(jump_detection, jump_percentage, in_phase1, ...
    in_phase2, quad1, quad2)
     n_jumps = 0;
     amp1 = sqrt(in_phase1.^2 + quad1.^2); amp2 = sqrt(in_phase2.^2 + quad2.^2);
     for jump_id = 1:length(amp1)
        if abs(db(amp1(jump_id)) - db(amp2(jump_id))) > jump_detection
               n_jumps = n_jumps + 1;
        end
     end
```

```
20      if n_jumps >= ceil(jump_percentage*(length(amp1)))
21          valid = 0;  % composed of interference
22      else
23          valid = 1;  % not composed of interference
24      end
25  end
```

A.3 Harmonic Sum

```
1  % HARMONIC SUM - EDUARDO SOUSA 2022
2  %
3  % outputs the harmonic sum
4  % inputs:
5  %   amp, phase - 2D matrix containing the amplitude and phase tracking, for
6  %   each harmonic-order
7  %   h_sel - contains the selected harmonics
8
9  function out = harmonic_sum(amp, phase, h_sel)
10 nh = length(h_sel);
11 n_samples = length(amp);
12 if nh == 1; amp = amp'; phase = phase'; end
13 period_samples = 0:0.1:2*pi;
14 for sample_id = 1:n_samples
15     k = 0;
16     for h_id = 1:nh
17         k = k + amp(h_id,sample_id).*sin(h_sel(h_id)*period_samples + phase(h_id,sample_id));
18     end
19     out(sample_id) = max(k);
20 end
21 end
```

A.4 H_1 Estimator

```
1  % H1 ESTIMATOR algorithm - EDUARDO SOUSA 2022
2  %
3  % function outputs the H1 estimator complex valued FRF
4  %
5  % the inputs are as follows:
6  %   amp - 3D matrix containing the response amplitude tracking for each
7  % DOF and each sweep
8  %   phase - 3D matrix containing the response phase tracking for each DOF
9  % and each sweep
10 %   f_phase - 3D matrix containing the amplitude tracking for each input
11 %   force and each sweep
12 % sweep and each input force
```

```
%   f_phase - 3D matrix containing the phase tracking for each input force
%   and each sweep

function h1 = h1_algorithm(amp, phase, f_amp, f_phase)
% vector preallocation
h1 = zeros(size(amp,1), size(f_amp, 1), length(amp));

% translation to complex coordinates
X = amp.*exp(1i*phase);
F = f_amp.*exp(1i*f_phase);

% H1 estimator computation loop
for sample_id = 1:length(amp)
    xx = squeeze(X(:,:,sample_id));
    ff = squeeze(F(:,:,sample_id));

    g_ff(:,:) = ff*ff';  % input autopower matrix
    g_xf(:,:) = xx*ff';  % output-input crosspower matrix
    h1(:,:,sample_id) = g_xf(:,:)/g_ff(:,:);
end
end
```

Appendix B

SIMULINK Block Diagram

In the present appendix, the block diagrams of the online Multi-Harmonic Digital Tracking Filter (MHDTF) are displayed. In Figure B.1, the MHDTF block diagram for a single harmonic-order is visible. This block takes as inputs the response signal to track, identified as y, the time value of the excitation frequency, $freq$, in rad/s and the harmonic order of the block, h_order. Figure B.2 exemplifies the combination of three blocks referent to harmonic 1,2 and 3 to create the MHDTF.

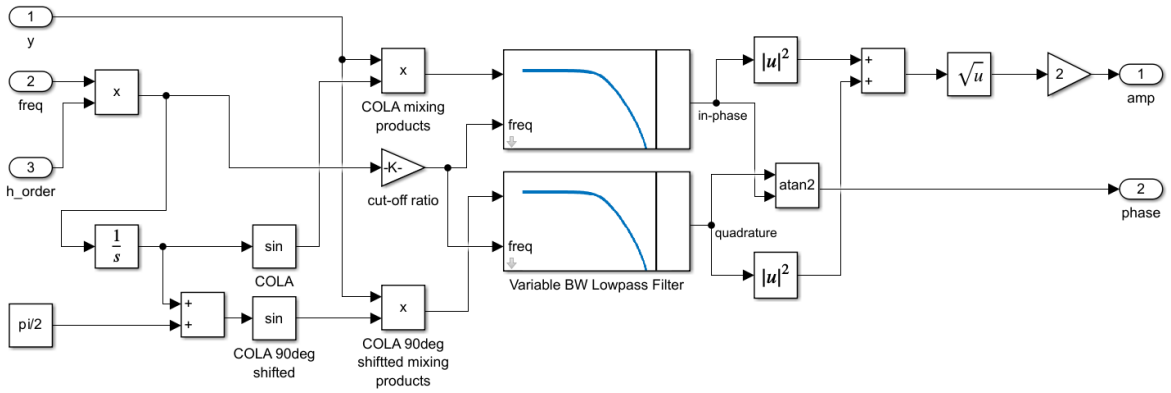

Figure B.1: Single harmonic-order SIMULINK block diagram.

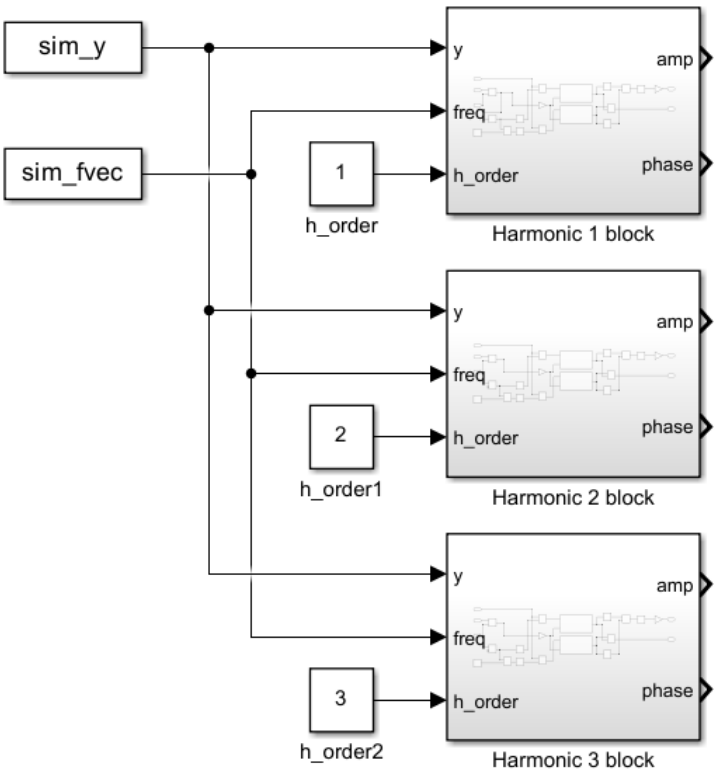

Figure B.2: MHDTF procedure SIMULINK block diagram.